CHALMERS

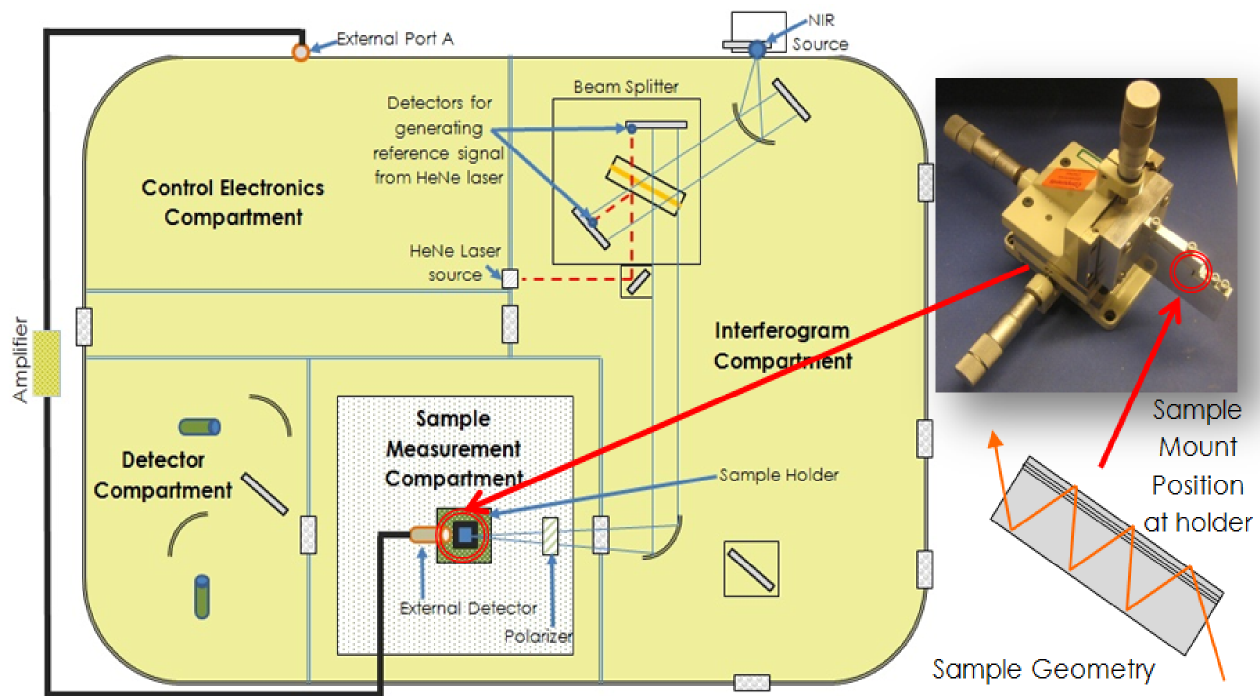

Characterization of GaN/AlN MQW based Heterostructures using Fourier Transform Infrared (FTIR) Spectroscopy

Master of Science Thesis in Communication Engineering

D. M. S. SULTAN

Photonics Laboratory
Department of Microtechnology and Nanoscience, MC2
Chalmers University of Technology
SE-41296 Gothenburg, Sweden, June 2010

THESIS FOR THE DEGREE OF MASTERS OF SCIENCE IN COMMUNICATION ENGINEERING

Characterization of GaN/AlN MQW based Heterostructures using Fourier Transform Infrared (FTIR) Spectroscopy

D. M. S. SULTAN

Examiner: PROF. SHUMIN WANG

Photonics Laboratory
Department of Microtechnology and Nanoscience, MC2
Chalmers University of Technology
SE-41296 Gothenburg, Sweden 2010

The Author grants to Chalmers University of Technology and University of Gothenburg the non-exclusive right to publish the Work electronically and in a non-commercial purpose make it accessible on the Internet.

The Author warrants that he is the author to the Work, and warrants that the Work does not contain text, pictures or other material that violates copyright law.

The Author shall, when transferring the rights of the Work to a third party (for example a publisher or a company), acknowledge the third party about this agreement. If the Author has signed a copyright agreement with a third party regarding the Work, the Author warrants hereby that he has obtained any necessary permission from this third party to let Chalmers University of Technology and University of Gothenburg store the Work electronically and make it accessible on the Internet.

Characterization of GaN/AlN MQW based Heterostructures using Fourier Transform Infrared (FTIR) Spectroscopy

D. M. S. SULTAN

© D. M. S. Sultan, June 2010.

Chalmers University of Technology
Department of Microtechnology and Nanoscience, MC2
Photonics Laboratory
SE-412 96, Göteborg, Sweden
Telephone + 46 (0)31-772 1000

Printed by Chalmers reproservice, Chalmers University of Technology
Göteborg, Sweden, June, 2010

Abstract

Quantum Cascade Lasers (QCLs) devices based on GaN/AlN multiple quantum wells (MQWs) on GaN substrates are capable of providing much higher power throughput compared with conventional laser diodes and stable in incessant operation at higher temperatures. Because of a large conduction band offset (~2eV), it has potentials to operate at 1.3-1.55 μm wavelength regime in fiber-optic telecommunications. To fabricate such materials with desired precision is still challenging and that's the key motivation of this thesis to work out by performing optical characterization of such materials using Fourier Transform Infrared (FTIR) spectroscopy. A significant modification and enhancement is done in instrumental setup after thorough theoretical investigations on working mechanisms of BRUKER IFS 55 FTIR spectroscopy to make it suitable for analyzing such specific device structures. Intersubband absorption is measured on several GaN/AlN MQW based samples with varied doping concentrations, well and barrier widths. The acceptable endmost outcomes were combined with the theoretical model to probe scientific resonance. Hereby, the findings from the thesis lead the designer to the right direction for choosing the appropriate parameters to obtain the prime product in future samples. At the end, temperature insensitivity on intersubband absorption peak energy has also been reconnoitered by the fact that the peak intersubband transition energy decreases by ~6meV at 400^0C compared to room temperature.

Keywords: FTIR, interferometer, GaN/AlN multiple quantum wells, heterostructures, IS absorbance, FWHM, spontaneous and piezoelectric polarization, band offset.

Acknowledgement

It’s my immense pleasure to announce my first thanks to my supervisor Prof. Shumin Wang for his never-ending, passionate and insightful guidance throughout the thesis work. I would like to show my greatest gratitude to Prof. Ander Larsson to let me introduce to walk on such wonderful research work.

My special gratitude goes to Martin Stattin, whose passionate walk along me made all complexities result oriented. I love to thank Yuxin Song whom I find a good friend. His fruitful discussion and cooperation was really helpful. A big thank goes to Kristian Berland, for his nice and fit assistance to made me trodden with adequate theories for designing temperature dependent experimental study on GaN/AlN MQWs. I would also like to mention the name of Rashid Farivar giving thanks for providing necessary information regarding growth process and GaN/AlN based heterostructures whenever be needed. I like to thank all other members of photonics lab as well whom I find friend, philosopher and guide.

Lastly, I would like to thank all of my friends and family members whose well wish and moral support helped to lead the way smoothly. Above all, I would like to give my deepest gratitude to God.

D. M. S. Sultan
June, 2010

Publication

The thesis is end up with the following publication:

[1] Kristian Berland, Martin Stattin, Rashid Farivar, D. M. S. Sultan, Per Hyldgaard, Anders Larsson, Shu Min Wang, and Thorvald Andersson,
"Temperature stability of intersubband transition in GaN/AlN Quantum wells",
Applied Physics Letter, (accepted).

List of Acronyms

2D	Two dimensional
AlN	Aluminum Nitride
ADC	Analog to Digital Converter
DLATGS	Deuterated L-Alanine doped Triglycine Sulfate
FTIR	Fourier Transform Infrared Spectroscopy
FWHM	Full Width Half Maximum
GaN	Gallium Nitride
IS	Intersubband
QTH	Quartz–Tungsten–Halogen
LED	Light Emitting Diode
LASER	Light Amplification by Stimulated Emission of Radiation
MQW	Multi Quantum Well
NIR	Near Infrared

Table of Contents

1 Introduction 6
2 Physical Description of AlN/GaN heterostructures 8
2.1 Band Structure 8
2.2 Polarity and polarization 9
2.3 Critical layer thickness and stain relaxation 11
2.4 Dopants 11
3 Intersubband absorption in GaN/AlN MQWs 12
3.1 Intersubband Transition 12
3.2 Quantum Cascade Laser (QCL) 13
3.3 Theoretical Model 14
4 Fourier Transform Infrared Spectroscopy 16
4.1 Michelson Interferometer 17
4.2 Fourier-Transformation 17
4.3 Bruker IFS 55 FTIR Spectroscopy 18
4.3.1 Power Supply Compartment 19
4.3.2 Interferometer Compartment 21
4.3.3 Detector Compartment 24
4.4 Spectrum manipulation using OPUS/IR software 25
4.4.1 Baseline correction 26
4.4.2 Smoothing 26
4.4.3 Curve-fitting 26
4.5 External Detectors 26
4.6 Absorption study setup 27
4.7 Temperature dependent study setup 28
5 Observation of intersubband absorbance in GaN/AlN MQWs 30
5.1 Structures of measured samples 30
5.2 Optical characterization 31
6 Temperature stability of intersubband transition in GaN/AlN Quantum wells 36
7 Summary and future direction 41
7.1 Summary 41
7.2 Future direction 41
Appendix A 43
Appendix B 44
Appendix C 45
References 46
PAPER 48

Chapter 1

1 Introduction

Semiconductor heterostructures are ultimate evolution in device structures that have brought us an enormous easy life being equipped with today's most advanced data communication and telecommunication applications. Beyond that an outstanding addition to such heterostructures is the device of intersubband (IS) transition which is enhanced with today's hot research branch of quantum architectures (i.e. quantum well (QW), quantum dot (QD), quantum well infrared photodetectors (QWIPs) etc). Intersubband transitions in nitride-based semiconductor heterostructures have potentials in the arena of optoelectronic devices especially in concern of temperature stability. One key feature of AlN/GaN heterostructures is the high band-offset (~2 eV) between gallium nitride (GaN) and aluminum nitride (AlN) that enables intersubband transitions in the near-infrared regime, $\lambda = 1\sim4\ \mu$m. Thus, intersubband devices such as modulators, detectors, and quantum cascade lasers (QCLs) have huge potentials to operate at wavelengths useful for fiber optic communication.

Due to the fact of wide band gap property, AlN/GaN heterostructures could offer high power, high speed and high frequency applications. Intersubband transitional utility makes such structures to build ultrafast 1.55 μm all optical switches that may operable at Tbit/s at room temperature because of the three orders of magnitude shorter in the relaxation time than the carrier life time [1]. Several groups have already reported intersubband absorption at 1.3~1.5 μm in GaN/AlN based multiple quantum wells (MQWs) [2, 3, 4]. One challenge to fabricate such heterostructures is growth technology due to a large lattice mismatch and a thermal expansion coefficient difference between GaN and AlN that are ~2.5% and 30% along the a-axis, respectively, at room temperature [5]. Besides, massive piezoelectric and spontaneous polarization effects due to the presence of high ionic bonding inside the GaN and AlN MQW structures influence the intersubband transition and play an important role in perfect designing of QCL devices' growth parameter to achieve as high as possible IS absorption.

In order to investigate the absorption property of such heterstructures, Fourier Transform Infrared Spectroscopy (FTIR) has been used. FTIR is one of the most important analytical techniques available to today's scientists. In FTIR spectroscopy, an infrared spectrum is obtained by passing infrared radiation through a sample and determining what fraction of the incident radiation is absorbed at a particular energy. The energy at which a maximum peak occurs in absorption characteristics corresponds to the frequency of a vibration mode of a sample molecule.

This thesis has been written with a background interest on optical characterization of GaN/AlN based QCL heterostructures. Some imperative growth related properties on AlN/GaN based heterostructures have been included in Chapter 2 to improve the understanding for the reader regarding thesis focus. In chapter 3, intersubband transition property of GaN/AlN MQWs is described along with the parameters used in the theoretical model so that readers may have an understanding of the discussion part regarding measured results of optical characterization using FTIR. Chapter 4 has been written to illustrate the instrumentation and experimental setup regarding optical characterization with FTIR. The basic ideas and definitions associated with FTIR spectroscopy along with a proper operation procedure have been described here. Apart from that, this Chapter covers the two important setups of intersubband study on GaN/AlN MQW heterostructures and temperature stability study. Later on, Chapter 5 and Chapter 6 have included extensive discussions on the experimental outcomes based on optical characterization of IS absorbance and temperature stability property of GaN/AlN MQW

heterostructures. An overview of the whole thesis in a summary along with some future directions regarding thesis work will take place in Chapter 7 at the end.

Chapter 2

2 Physical Description of AlN/GaN heterostructures

AlN/GaN heterostructures are combination of multiple AlN and GaN based alloy layers. These two alloys follow Wurtzite structures and consequently inherit the nature of thermodynamic stable phase. Besides this leads to unique material properties such as built in electric field due to spontaneous and piezoelectric polarization. Sapphire (Al_2O_3) is widely used as a substrate for GaN growth that exhibits different lattices like $a = 0.319$ nm for GaN and $a = 0.312$ nm for AlN. The lattice mismatched epitaxial growth causes a large number of dislocations in nitride devices; with a dislocation density that is more than five orders of magnitude higher compared with other compound semiconductor heterostructures [6]. However, there are remarkable small impacts on the performance of GaN based light emitters due to the presence of such defects which still have not been fully understood. So, the research interest on such materials is growing significantly today. Another property of GaN/AlN heterostructures is that it may activate a high doping energy like 170 meV for the acceptor doping. It requires a high acceptor density near 10^{20} cm^{-3} to achieve a free hole concentration of about 10^{18} cm^{-3}. Due to the high doping, the hole mobility becomes significantly lower i.e. 10 cm^{2}s^{-1}V^{-1} but the electron mobility becomes quite high like 2000 cm^{2}s^{-1}V^{-1} whereas the critical breakdown voltage is more than 3 MVcm^{-1}.

Even though the recent commercial deployment of GaN based devices, it is not fully understood yet the net internal physical mechanism that resides on such GaN/AlN based heterostructures. Advanced numerical simulations and modeling of such structures along with characterizing the samples can further improve performance. The theoretical modeling of such heterostructures has already included the material composition, carrier density, internal temperature, built in electric field and relevant physical conditions and the simulation has been performed by open source scientific tools like Python [7].

2.1 Band Structure

Energy bandgap (E_g) of Wurtzite semiconductor materials span the wide range from infrared to ultraviolet (0.7 to 6.2 eV) and has been shown in Figure 2.1 below.

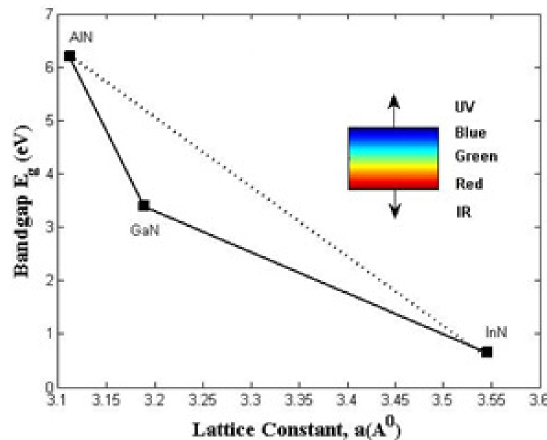

Figure 2.1: Bandgap energy of Wurtzite nitrides (AlN, GaN, InN respectively) has been plotted here against the lattice constant without an account of the bowing parameter.

Once the lattice constant of buffer layer is known, the mole fraction, x, can be determined by using Vegard's law that is an approximate empirical rule which holds a linear relation at a constant temperature between the crystal lattice parameters of an alloy and the concentrations of the constituent elements,

$$E_g(Ga_{1-x}N_x) = (1-x)E_g(Ga) + xE_g(N) - bx(1-x) \tag{2.1}$$

where, b is called the bowing parameter for the alloy.

The energy bandgap, E_g of GaN is most accurately determined by photoluminescence measurement of the excitonic effect. The actual bandgap is recovered by adding the estimated binding energy to the observed excitonic binding energy. The GaN energy gap is dependent upon the layer thickness due to the strain [8]. In the Wurtzite phase, most of the conventional nitrides exhibit a direct bandgap of $\sim$2 eV or higher in the Γ valley [12]. Even though the energy bandgap, E_g at 300 K is $\approx$ 3.38 eV may exist at GaN because of very thick layer (a few hundreds μm), the suggested value to use in a numerical model for GaN structures should be less than 2.8 eV [31]. The Varshini coefficients (α, β) for Wurtzite GaN have also been studied extensively [9, 10, 11]. Owing to a small relative change in the bandgap energy by 72 meV (between 0 and 300K), GaN device characteristic tends to be relatively insensitive to the precise values of the Varshini parameters. The more extensive experimental studies on such temperature dependence have been presented in Chapter 6 later on.

2.2 Polarity and polarization

Due to the partly ionic nature of III-Ns and the lacking at inversion symmetry, the heterostructures exhibit a higher order magnitude of spontaneous polarization. These nitride heterostructures also introduce piezoelectric effect along the <0001> direction of crystal. This piezoelectric effect occurs due to strain components like lattice mismatch strain or thermal strain where both of them are induced in lieu of thermal expansion of the substrate and the epitaxial layer.

Among the III-N structures, GaN/AlN MQWs are a very special class of materials. These types of materials are also very much popular because of their favorable mechanical properties and the wide span of the direct band gap. They show only the spontaneous polarization (P_{sp}) that is a built in electric potential and is absent in other III-V semiconductors. Therefore, this property is one of the triggering factors to spoil the quantum efficiency of MQW nanostructures. P_{sp} is present in only two kinds of materials: ferroelectric and pyroelectric materials. P_{sp} can be controlled and mitigated by applying a strong electric field on ferroelectric materials while the presence of P_{sp} in pyroelectric materials is quite tough to control (as P_{sp} occurs along the symmetrical axis of the crystal) and this type of polarization dominates in GaN/AlN MQWs because of their high ionic bonding. Modern Polarization Method (MTP) helps to calculate the exact polarization effect in pyroelectric materials. Since GaN does follow the Wurtzite crystal structure, the P_{sp} occurs along the [0001] direction and is equally oriented. The pyroelectric permanent polarization is an intrinsic property related to the bonding nature of materials, whose origin is somewhat subtle. It can be ultimately attributed to the fact that the geometrical center of the negative charges (electron) in the solid does not coincide with the center of positive charges (nuclei). The less rigorous but more intuitive way of expressing the reason behind P_{sp} in GaN/AlN MQWs structures is that the bond (connecting the atoms with first neighbors) has more ionic nature when compared to other structures.

The non-ideal crystal structure in Wurtzite GaN can be motivated by the origin of the polarity that is the uneven charge distribution between the neighboring atoms in a lattice. The bonds in GaN along the polar axis are faced by the nitrogen in one direction and Ga in the other direction. The Wurtzite

structure of GaN for <0001> epitaxial growth exhibits two polarities in accordance to the orientation of Ga-N bonds [13].

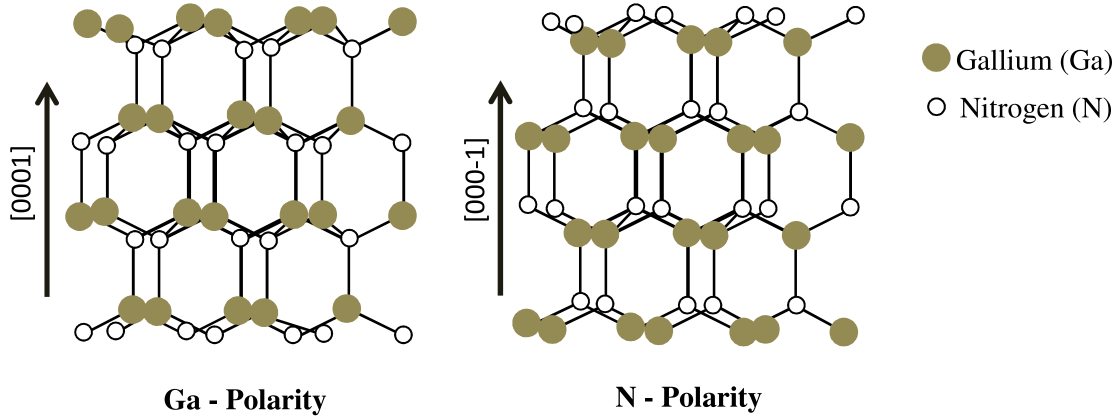

Figure 2.2: Atomic models of Ga and N –polarity on a GaN Crystal.

The Wurtzite GaN lattice polarity is a bulk property as determined by the bond sequence in the crystal and is different from surface termination. Mostly, it is determined by atoms terminating at the surface. The Ga polar GaN is terminated with cation atoms with each cation atom at the surface having a single dangling bond stretching normal to the surface (crystalline direction is defined as [0001]), while the N polar GaN is characterized by anion termination with a single dangling bond normal to the surface (crystalline direction is [000-1]) [20].

The spontaneous polarization $\overrightarrow{P_{sp}}$ is an inherent property and is related to the non-ideality of the crystal structure with respect to the $\frac{c_0}{a_0}$ ratio. In crystallographic direction [000-1], the spontaneous polarization, $\overrightarrow{P_{sp}}$ is different. The reference values of general properties of GaN/AlN MQW structures that are usually recommended in the numerical modeling of GaN/AlN MQWs IS absorbance have been given below.

Table 2.1: General properties of GaN/AlN heterostructures [21, 22].

Constant	AlN	GaN
Bandgap energy, E_g(eV)	6.2	3.39
Lattice constant, a ($\dot{A}$)	3.1079	3.1968
Lattice constant, c ($\dot{A}$)	4.982	5.185
Spontaneous polarization, $\overrightarrow{P_{sp}}(cm^{-2})$	-0.0898	-0.0339
Piezoelectric coefficients, $e_{33}(cm^{-2})$	1.505	0.667
Piezoelectric coefficients, $e_{31}(cm^{-2})$	-0.533	-0.338
Piezoelectric coefficients, $e_{15}(cm^{-2})$	-0.351	-0.167

The direction of piezoelectric polarization $\overrightarrow{P_{pz}}$ depends on the film polarity and the stress state (tensile or compressive). This $\overrightarrow{P_{pz}}$ can be calculated using the following equation:

$$\overrightarrow{P_{pz}} = e_{lm}\varepsilon_{jk} \tag{2.2}$$

where, e_{lm} is the piezoelectric coefficient tensor and $\varepsilon_{jk}$is the strain tensor. In piezoelectric constant, e_{lm}, the independent coefficients are reduced to only three: $e_{31} = e_{32}, e_{33}$ and $e_{15} = e_{24}$. Therefore, the piezoelectric equation becomes:

$$\overrightarrow{P_{pz,x}} = e_{15}\varepsilon_{13} \tag{2.3}$$

$$\overrightarrow{P_{pz,y}} = e_{15}\varepsilon_{23} \tag{2.4}$$

and, $$\overrightarrow{P_{pz,z}} = e_{31}\varepsilon_{11} + e_{31}\varepsilon_{22} + e_{33}\varepsilon_{33} \tag{2.5}$$

The layer that is bi-axially strained in the XY plane (since heterostructures grown perpendicular to <0001> axis generally), the equation of piezoelectric polarization will be of *z*-direction component only:

$$\overrightarrow{P_{pz,z}} = 2\frac{a(T)-a_0(T)}{a_0(T)}(e_{31} - e_{33}\frac{C_{31}}{C_{33}})\varepsilon_{\perp} \tag{2.6}$$

where, $\varepsilon_{\perp} = \varepsilon_{11}+\varepsilon_{22}$ is the plain strain, $a(T)$ is the layer lattice constant at temperature *T*, $a_0(T)$ is the lattice constant of the bulk material at temperature *T* and C_{31}, C_{33} are elastic constants. Hence, the total polarization in absence of an external electric field becomes:

$$\overrightarrow{P_{tot}} = \overrightarrow{P_{sp}} + \overrightarrow{P_{pz,z}} \tag{2.7}$$

2.3 Critical layer thickness and stain relaxation

Because of the lattice mismatch between an epitaxial layer and a substrate, a thin layer may be strained and its thickness depends upon the magnitude of lattice mismatch. If the growth thickness reaches the critical layer thickness (CLT), misfit dislocations, staking faults and 3D islands are introduced in the structures.

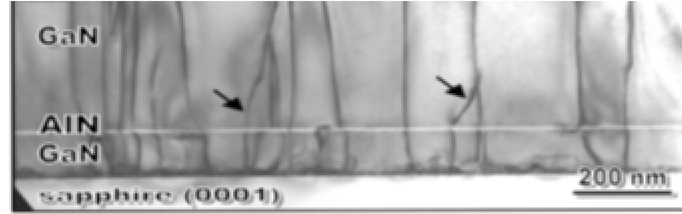

Figure 2.3: Low magnification XTEM image of misfit and threading dislocations in GaN/AlN heterostructures [14] where arrows indicate induced dislocations.

2.4 Dopants

Both the unintentional and the intentional impurities (dopants) play the vital role in device property and growth technique in formation of sample device architecture. Typically, undoped GaN has a high n-type background carrier concentration, ~10^{16}cm^{-3}. So, it would be difficult to do p-doping. Silicon is the most common n-type dopant for III-Ns. In GaN, silicon can easily be doped at Ga sites and has an activation energy ~27 meV [15, 16]. One interesting fact is that the high Si doping introduces stress in the material when the GaN film is thicker than 2 μm. It leads to crack when the Si concentration exceeded 10^{19}cm^{-3} [17, 18]. By controlling the Si source temperature, the doping concentration has been controlled during sample growth. Si-delta doping (δ −doping) has been employed which means that the dopants are spatially localized in a single atomic plane. This introduces the doping spike along the growth direction, which can be defined by a δ function. δ −doping is employed by the time factor of shutter opening (i.e. from a few seconds up to several minutes) depending on the desired doping concentration.

Chapter 3

3 Intersubband absorption in GaN/AlN MQWs

3.1 Intersubband Transition

Optical transition basically occurs between the conduction and the valance band (interband transition). It may also be done within the conduction or the valance band that is known as intersubband transition. Interband transition consists of opposite E(k) dispersion relations. Therefore, the optical transition spectrum is broad and strongly dependent upon temperature. In the contrary, Intersubband transition occurs with the same type of electronic energy dispersion. Due to this fact, intersubband transition induces a narrower peak.

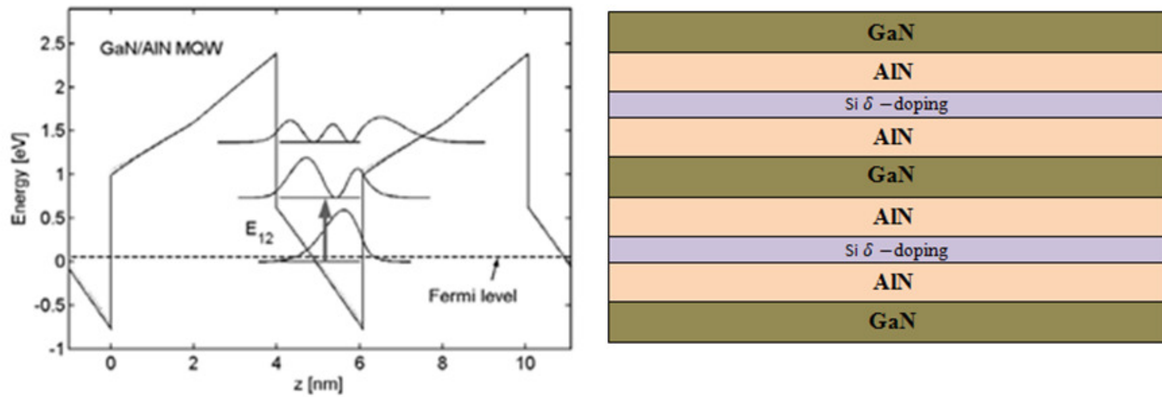

Figure 3.1: Schematic drawing of an AlN/GaN/AlN quantum well potential profile with Si δ-doping (at right). At left, the solid line represents the total potential of conduction band, E_c, including exchange correlation potential (arrow indicates the intersubband transition) while the dotted line represents the Fermi level at room temperature [28].

The important property in the intersubband transition is the very short relaxation time. Basically, intersubband transition occurs due to stronger interaction of LO-phonons with electrons. This electron relaxation by emitting or absorbing LO phonons is very fast, i.e. in the femtosecond scale. Since the space charge affects the subband energy and potential and vice versa, the Schrödinger and Poisson equation have to be solved self-consistently. In the numerical model, Schrödinger equation is solved for an unperturbed potential and thereby the electron population of each state is calculated generating a new potential profile by the use of Poisson equation. This new potential is then used for the next iteration. This iterative process is held until the energy state converges to a steady value. Beside this fact, the E(k) starts to deviate from the parabolic dispersion for the k-value away from the Γ point (k=0) showing the nonparabolicity. This effect is significant for the case of intersubband transition in narrower wells where the transition energy becomes comparable with the band-edge offset. The energy dependent electron effective mass, m_e^*, is used to take account of the nonparabolicity in the numerical model using the following equation:

$$m_e(E) = m_e(1 + \frac{E - E_c}{E_g}) \tag{3.1}$$

where, E_c is the conduction band energy. Besides, many body effect has also been included in the numerical calculation to consider shift of intersubband transition energy due to a high electron density. This many body effect includes the exchange correlation energy, the depolarization shift and the

excitonic shift. The exchange correlation energy can be taken into account as a correction to the total energy potential by adding the following equation [28]:

$$V_{xc}(Z) = -\frac{2}{\pi r_s}\left(\frac{9\pi}{4}\right)^{\frac{1}{3}}\left[1 + 0.7734\frac{r_s}{21}ln\left(1 + \frac{21}{r_s}\right)\right]\frac{e^2}{8\pi\varepsilon_r\varepsilon_0 a_0} \tag{3.2}$$

where, $r_s(z) = 1/\left[\left(\frac{4\pi}{3}\right)a_0{}^3(z)n(z)\right]^{\frac{1}{3}}$ is the ratio of the mean electron distance to the effective Bohr radius, $a_0(z) = \left(\frac{\varepsilon_r(z)}{m_e(z)a_B}\right)$, and Bohr radius, $a_B = \frac{4\pi\varepsilon_0\hbar^2}{m_0 e^2}$.

3.2 Quantum Cascade Laser (QCL)

The noble appliance of such intersubband transition is Quantum Cascade Laser (QCL) that was first demonstrated by F. Capasso *et al.* in 1994 [19]. In a QCL, the principle of electron transfer remains as electron waterfalls. When a proper bias voltage is applied, electrons cascade down via an energy staircase where they emit photons for every fall step. A typical structure is made of a periodic repetition of two sections: one does act as an injection region another one as an active region (shown in Figure 3.2). From the injection region, electrons occupy the same level as their energy level (3) of the active section where the laser transition takes place. Afterwards, optical phonon assisted non-radiative recombination occurs from the level (2) to level (1) and electrons enter into the next stage by tunneling.

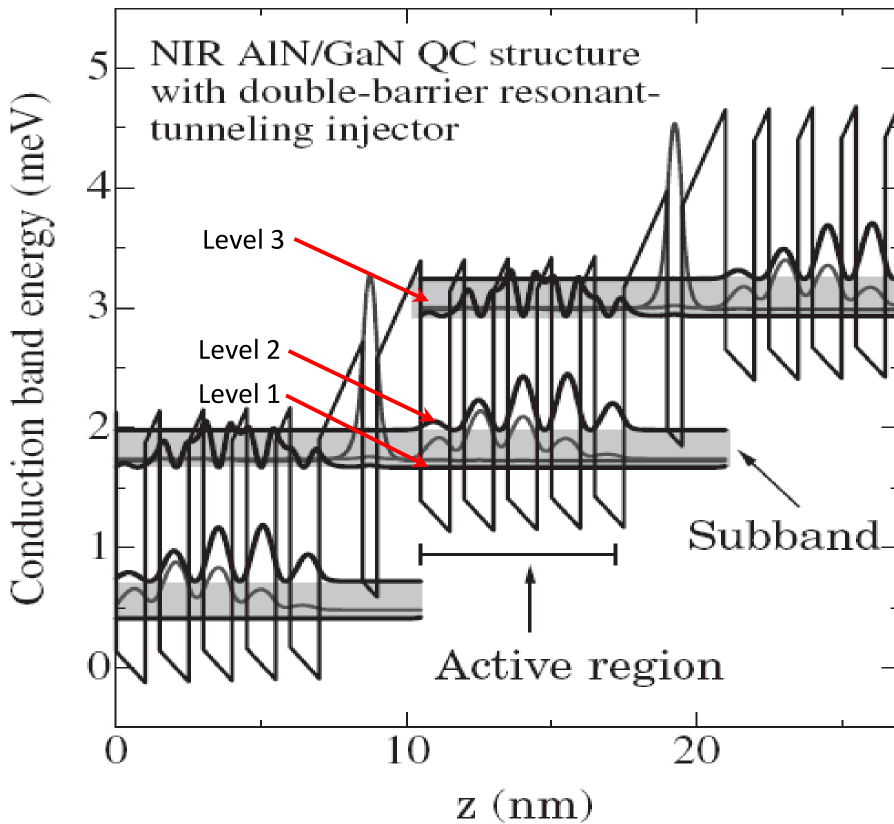

Figure 3.2: A schematic diagram of a GaN/AlN Quantum Cascade Laser (QCL).

The output power of a QCL is normally higher in comparison to a conventional diode laser being operated at the same wavelength due to the cascading effect. It comprises of a periodic series of thin layers of varying material composition forming a superlattice. The superlattice introduces a varying electric potential across the length of the device as there is a varying probability of electrons to occupy

different positions over the device length. By engineering the device layer thicknesses, it is possible to achieve the optimum population inversion between the two subbands to obtain laser emission. Since the position of the energy levels in this kind of laser device is primarily determined by the layer thicknesses but less by the material properties, it is possible to tune the laser emission wavelength over a wide range using the same material.

3.3 Theoretical Model

Intersubband transition in an AlN/GaN structure is induced due to its large conduction band offset typically ~ 2 eV [23]. Therefore III-N QWs can be used to extend the operation wavelength of intersubband devices into the technologically important fiber optical communication range. The peak absorption energy depends on the design of material, such as well and barrier widths, barrier composition and doping. For investigating the theoretical absorption nature on AlN/GaN materials, Schrödinger and Poisson equation have been solved self-consistently to determine the confined energy levels and the envelop function. The numerical model has carried out using finite difference method and it secures a high degree of efficiency and flexibility.

A distinctive feature of GaN / AlN MQWs is the presence of strong spontaneous and piezoelectric polarization, leading to a large interface charge density. The resulting electric field strongly affects the intersubband absorption properties. At the interface between two semiconductor layers with different compositions, a sheet charge induces the change in total polarization in layers. According to the electrostatic boundary condition, in MQWs and superlattices grown along the c-axis, the interface sheet charge can be calculated as:

$$\rho_{pol} = P^i - P^j = \left[{P_{sp}}^i + {P_{pz}}^i\right] - \left[{P_{sp}}^j + {P_{pz}}^j\right] \tag{3.3}$$

where, i donates the layer above the layer j. This 2D sheet charge density is included in the Poisson equation as a source term.

Two important modeling aspects have to be considered. Firstly, a mathematical model is needed for describing physics of semiconductor materials and devices and secondly, it is necessary to use a suitable numerical technique to solve the coupled equations that describe the system. The numerical model employed in this modeling is done on the basis of self-consistent solution of the Schrödinger and Poisson equations, within the finite difference approach. In the effective-mass approximation [24, 25], the electron energies and wavefunctions are obtained by solving the Schrödinger equation,

$$\left[-\frac{\hbar^2}{2}\frac{\partial}{\partial z}\frac{1}{m^*(z,E)}\frac{\partial}{\partial z} + V(z)\right]\psi_i(z) = E_i\psi_i(z) \tag{3.4}$$

where, $m^*(z,E)$ is the energy and position dependent electron effective mass and z is the distance along the growth axis. The total potential energy $V(z) = \Delta E(z) - q\phi(z) + V_{xc}$ includes the exchange correlation energy, V_{xc}, the conduction band discontinuity, $\Delta E(z)$, and the electrostatic potential, $\phi(z)$, resulting from all charges in the system. Once solved, the subband energies, E_i, and wavefunctions, ψ_i are available to compute the total potential. The electrostatic potential, $\phi(z)$ is obtained by the Poisson equation:

$$\frac{d}{dz}\epsilon(z)\frac{d}{dz}\phi(z) = q\left[n(z) - p(z) - {N^+}_D(z) + {N^-}_A(z) - \rho_{pol}\right] \tag{3.5}$$

where, q is the electron charge and ϵ is the dielectric constant, ${N^+}_D(z)$ and ${N^-}_A(z)$ are the local concentration of ionized donor and acceptor, respectively, and ρ_{pol} is the bound polarization charge density at each well/barrier interface. The numerical model interface includes the partial ionization acceptor and donors. This is particularly important for well-doped structure where a limited fraction of

donors and acceptors can be ionized. The electron concentration is given by Fermi-Dirac distribution (a similar equation holds for holes)

$$n(z) = N \sum_i |\psi_i|^2 \ln[1 + \exp((E_f - E_i)/k_B T)] \quad (3.6)$$

where, E_f is the Fermi energy for the system, E_i is the subband energy, $N = \frac{m^* k_B T}{\pi \hbar^2}$, where $m^*$is the effective mass in the well. At equilibrium, the Fermi level E_f is chosen to be constant and zero throughout the structure. The intersubband absorbance coefficient is calculated by using the self-calculated solution [24]:

$$\alpha(\hbar\omega) = \left(\frac{e^2 \omega}{n_r c \epsilon_0}\right) \frac{|\mu_{ij}|^2 (\Gamma/2)}{(E_j - E_i - \hbar\omega)^2 + (\Gamma/2)^2} (N_i - N_j) \quad (3.7)$$

where, $\mu_{ij} = \langle \psi_i | z | \psi_j \rangle = \int \psi_j^* z \psi_i dz$, $\hbar\omega$ is the photon energy, n_r is the refractive index, c is the speed of light, μ_{ij} is intersubband dipole moment, $\psi_i$and $\psi_j$are the subband wavefunctions, Γ is the optical field linewidth and $N_{i(j)}$is the numbers of electrons per unit volume in the i(j)th subband.

The linewidth, Γ palys an important role in the model since a narrower $\Gamma -$ value gives rise to stronger peak absorption in intersubband absorption or to a larger gain for QCLs. The linewidth depends upon the elastic (impurity scattering, scattering by interface roughness) and inelastic (acoustic and optical phonon scattering, spontaneous photon emissions) collisions and is given by:

$$\Gamma = 2\hbar(\frac{1}{2\tau_1} + \frac{1}{\tau_2}) \quad (3.8)$$

where, $\tau_1$and $\tau_2$are the lifetime corresponding to inelastic collisions (spontaneous photon emission) and elastic collision, respectively. In the numerical model, the inhomogeneous contribution to Γ that leads to the change in the maximum intersubband energy due to the barrier and well thickness fluctuation of one monolayer has been computed. The effect can be included using the following formula to evaluate Γ:

$$\Gamma = max\left(\Delta E_{12}\left(L_b \pm \frac{ML}{2}, L_w \pm \frac{ML}{2}\right)\right) - min\left(\Delta E_{12}\left(L_b \pm \frac{ML}{2}, L_w \pm \frac{ML}{2}\right)\right) \quad (3.9)$$

where, L_b is the barrier width, L_w is the well width and ML is one monolayer thickness.

After external excitation, electrons at the ground state are excited to the regions with strong nonparabolic effects. The presence of nonparabolic energy dispersion leads to the shift of eigenvalues of the confined states. The higher subbands are shifted downwards and the ground states shift upwards. In III-V materials, this nonparabolicity effect is multiplied by the polarization effect that further increases the well depth. The nonparabolicity effect has been included by taking into account the energy dependent effective mass $m^*(z, E)$ in Schrödinger equation. Many body effects like depolarization effect and excitonic shift have also been added to correct the total potential that resides in the structure. The correction at IS absorbance peak energy, $\widetilde{E_{12}}$ can then be addressed by the following equation,

$$\widetilde{E_{12}} = E_{12}\sqrt{(1 + \gamma - \delta)} \quad (3.10)$$

where, E_{12} is the IS transition energy (shown at Figure 3.1), γ is the depolarization shift and δ is the excitonic shift. Collective effect of both of them generally leads to a blue shift. The depolarization effect occurs due to the resonant screening between electron plasma in the QWs and the applied electromagnetic field. The excitonic effect is due to the Coulombic interaction between the excitonic electrons and the quasi holes left behind in the ground state which reduces the absorption frequency [28].

Chapter 4

4 Fourier Transform Infrared Spectroscopy

Fourier Transform Infrared Spectroscopy (FTIR) is the outstanding characterizing tool used for analyzing QCL structures developed so far, especially for analyzing the intersubband transition property by measuring the absorption. One of the great advantages of infrared spectroscopy is that any sample in any virtual state may be studied. Liquids, solutions, pastes, powders, films, fibers, gases and surfaces can all be examined with a judicious choice of a sampling technique. As a consequence of the improved instrumentation, a variety of new sensitive techniques have now been developed in order to examine formerly intractable samples.

Infrared spectrometers have been commercially available since the 1940s. At that time, the instruments relied on prisms to act as dispersive elements, but by the mid-1950s, diffraction gratings had been introduced into dispersive machines. The most significant advances in infrared spectroscopy, however, have come about as a result of the introduction of Fourier-transform spectrometers. This type of instrument employs an interferometer and exploits the well-established mathematical process of Fourier-transformation. Fourier-transform infrared (FTIR) spectroscopy has dramatically improved the quality of infrared spectra and minimized the time required to obtain data. In addition, with constant improvements to computers, infrared spectroscopy has made further great strides.

Fourier-transform infrared spectroscopy is based on the idea of the interference of radiation between two beams to yield an interferogram. The latter is a signal produced as a function of the change of path length between the two beams reflected from two mirrors (resides in interferometer block). The two domains of distance and frequency are interconvertable by the mathematical method of Fourier transformation.

The basic components of an FTIR spectrometer are shown schematically below.

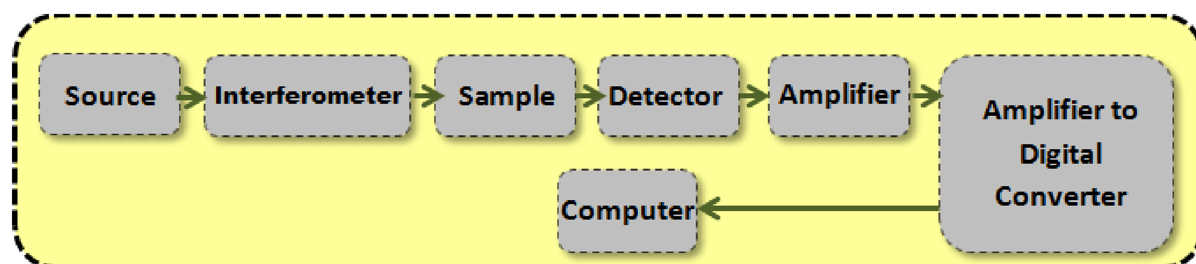

Figure 4.1: Basic components of an FTIR Spectrometer.

Upon amplification of the signal, in which high-frequency contributions have been eliminated by a low pass filter, the data are converted to digital form by an analog-to-digital converter in the ADC block and finally transferred to the computer for Fourier-transformation computation. FTIR instruments have several significant advantages over older dispersive instruments. Two of these are the Fellgett (or multiplex) advantage and the Jacquinot (or throughput) advantage. The '*Fellgett advantage*' is due to an improvement in the signal-to-noise (SNR) per unit time, proportional to the square root of the large number of resolution elements being monitored simultaneously. In addition, because FTIR spectrometry does not require the use of a slit or other restricting device, the total source output can be passed through the sample continuously. This results in a substantial gain in energy at the detector, hence translating to higher signals and improved SNRs. This is known as '*Jacquinot's*

advantage'. Another strength of the FTIR spectrometry is its speed advantage. The mirror has the ability to move short distances quite rapidly, and this, together with the SNR improvements due to the Fellgett and the Jacquinot advantages, make it possible to obtain spectra on a millisecond timescale. In interferometry, the factor which determines the precision of the position of an infrared band is the precision with which the scanning mirror position is known. By using a Helium–Neon (HeNe) laser as a reference, the mirror position is known with a high precision. This is also known as '*Conne's Advantage*'.

4.1 Michelson Interferometer

The most common interferometer used in FTIR spectrometry is a Michelson interferometer, which consists of two perpendicularly plane mirrors, one of which can travel in a direction perpendicular to the plane of the stationary one (shown in Figure 4.2). A semi-reflecting film, the *beamsplitter*, bisects the planes of these two mirrors. The beamsplitter material has to be chosen according to the wavelength region to be examined. Materials such as germanium or iron oxide are coated onto an 'infrared-transparent' substrate (i.e. potassium bromide or cesium iodide) to produce beamsplitter for the mid- or near-infrared regions. Thin organic films, such as poly ethylene terephthalate, are used in the far-infrared region.

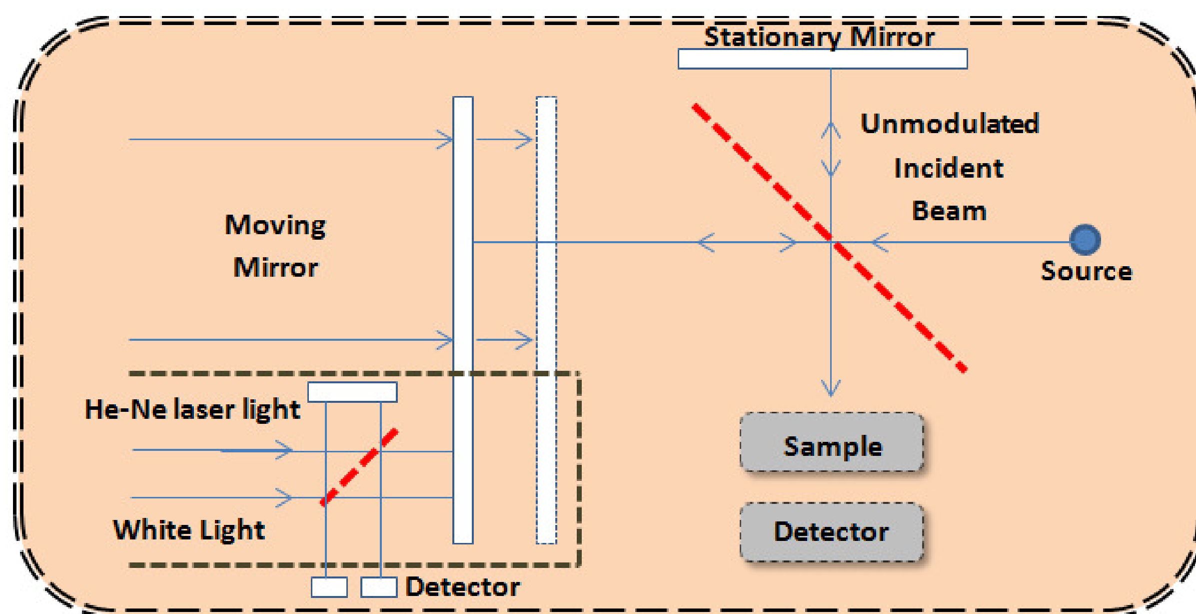

Figure 4.2: Schematic diagram of a Michelson interferometer.

If a collimated beam of monochromatic radiation of wavelength (λ) is passed into an ideal beamsplitter, 50% of the incident radiation will be reflected to one of the mirrors while 50% will be transmitted to the other mirror. The two beams are reflected from these mirrors, returning to the beamsplitter where they recombine and interfere. Afterwards, 50% percent of the beam reflected from the fixed mirror is transmitted through the beamsplitter while another 50% is reflected back in the direction of the source. The beam which emerges from the interferometer at 90^0 to the input beam is called the transmitted beam and this is the beam detected in the FTIR spectrometry.

4.2 Fourier-Transformation

The essential equations for Fourier-transformation relating the intensity falling on a detector as a function of retardation, $S(\delta)$ (in Volt), to the source intensity at a particular wavenumber, $\tilde{\nu}$, given by $B(\tilde{\nu})$, can be written by the following equation if the source assumed is continuum:

$$S(\delta) = \int_{-\infty}^{+\infty} B(\tilde{v}) cos(2\pi\tilde{v}\delta) d\tilde{v} \quad (4.1)$$

which is one half of a cosine Fourier-transform pair. Another can be defined by following:

$$B(\delta) = \int_{-\infty}^{+\infty} S(\tilde{v}) cos(2\pi\tilde{v}\delta) d\tilde{\delta} \quad (4.2)$$

These two equations are interconvertable and are known as a Fourier-transform pair. Each can be converted into the other by the mathematical method of Fourier-transformation. Since, retardation referring to mirror movement and thereby, Eq. 4.1 and Eq. 4.2 will be of finite integral and limited by the user defined resolution at OPUS/IR software. These two equations are solved using fast Fourier-transformation (FFT) algorithm which is quite fast. Due to a rapid scanning, FTIR has the ability to increase the SNR by signal-averaging, leading to an increase of SNR proportional to the square root of the scanning time as follows [33]:

$$SNR = \sqrt{n} \quad (4.3)$$

where, n denotes the number of scanning before averaging.

There are diminishing returns for signal-averaging. It takes an increasingly longer time to achieve better improvements. The accumulation of a large number of repeated scans makes greater demands on the instrument. It is normal to incorporate a laser monochromatic source in the beam of the continuous source. The laser beam produces standard fringes which can 'line-up' successive scans accurately and can determine and control the displacement of the moving mirror at all times.

4.3 Bruker IFS 55 FTIR Spectroscopy

IFS 55 is a instrument made by Bruker Optics that incorporates both Fourier transform and interferometry together to form Fourier Transform Infrared Spectroscopy. It has a dimension of 61 cm × 70 cm × 27 cm.

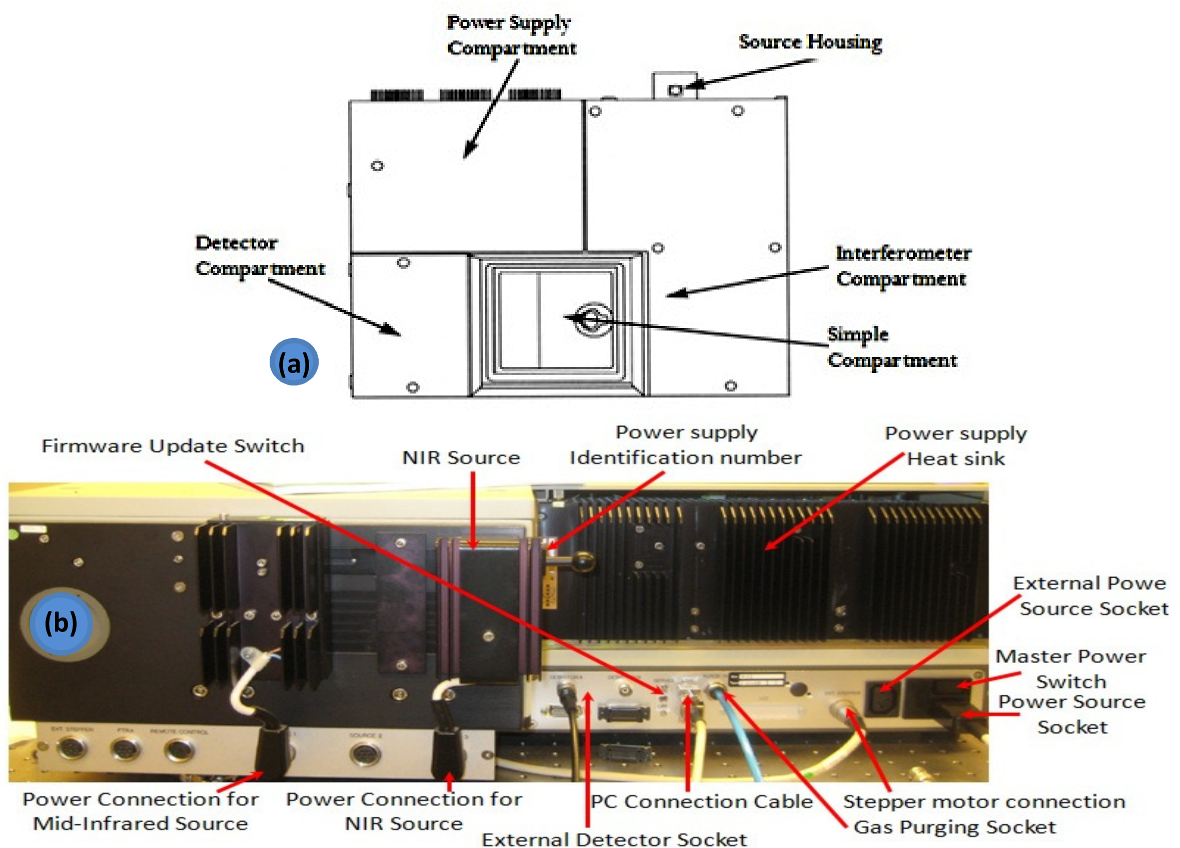

Figure 4.3: (a) Top view and (b) rear view of IFS 55 FTIR spectroscopy.

To perform the measurement optimally and for its long term reliability, the operation should be held 18 - 30^{0}C and within less than 70% humidity. If the temperature variance fluctuates more than 2^{0}C, then measurement optimality may vary during observation. This machine is designed to characterize the spectra in the frequency region of 7500-370 cm^{-1} (1333 nm ~ 27027nm). However, the characterization limit on wavelength regime is also dependent upon the splitting limit by the beamsplitter (mounted in the interferometer compartment), detection limit of photodetector as well as by the sampling frequency (i.e. frequency of HeNe laser in the case of IFS 55). The scanning resolution of this machine can be optimized to a limit of 0.2 cm^{-1}.

4.3.1 Power Supply Compartment

The spectrometer electronics can be found in the power supply compartment that is treated as the processing brain in IFS 55. The main tasks of this compartment are controlling the interferometer moving mirrors, automatic acquisition and processing of measured signals and storing and executing the spectrometer control program customized for a specific spectrometer configuration.

The IFS 55 power supply basically consists of a power supply section for the FTIR spectroscopy, TC20 IFM board (interface control board), TC20 processor board (interface board between the PC and the FTIR itself), and analog board that converts the analog detector signal to the digital one for further numerical processing and last the HeNe laser components (shown at Figure 4.4 (a)).

This HeNe laser is used as an internal reference source into the interferometer to solve the drive performance problem. The HeNe laser emits light with a known and stable wavelength under any circumstance. The laser beam parallels the signal path through the interferometer and produces its own interferogram at a separate detector. This reference interferogram is used as an extremely accurate measure of the interferometer displacement (Optical Path Difference (OPD)).

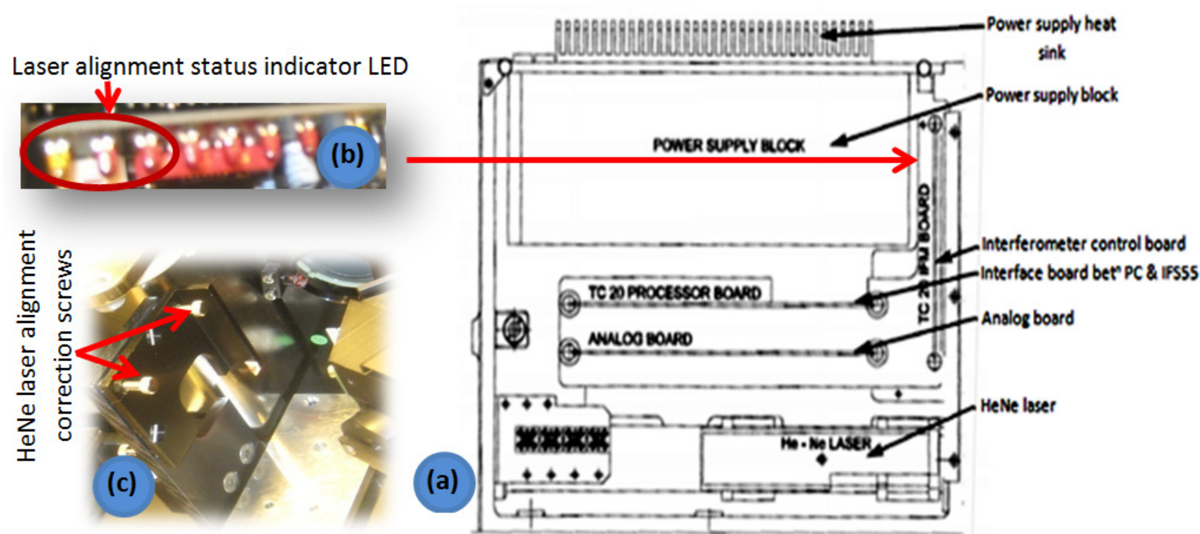

Figure 4.4: (a) Schematic figure of the power supply compartment and (b) laser alignment status indicator LED embedded at TC 29 IFM BOARD (interface control board) (c) laser alignment correction screws.

We can, therefore, write the following equation for a HeNe based FTIR:

$$\lambda_i = \lambda_r * (f_r / f_i) \quad (4.4)$$

where, subscript '*r*' denotes the HeNe reference and '*i*' indicates the measured signal at the detector.

We can now calculate the spectrum without extremely tight tolerances on the velocity. This was just a theoretical example. Now let us see how the reference interferogram is actually used in IFS 55.

The signal from the interfering beams of the He-Ne laser is monitored by a detector. What is observed is a sinusoidal signal. The average value remains always same as the beam is neither divided nor interference produced (the HeNe laser lases at 633 nm and the CaF_2 beamsplitter mounted in IFS can split the signal in the wavelength range from 1000 nm to 8333 nm) while passing through the beamsplitter. The sinusoid goes positive and negative about this value. The average signal level is called '*zero level*'. After acquisition of the signal (at resolution by user setting at OPUS/IR software) along with the He-Ne laser reference, sampling process is held in the TC20 processing board to digitize the analog signal and then send it to the PC for achieving the spectrum by applying Fourier transformation. A high precision electronic circuit is integrated at the TC20 processor board that produces a voltage pulse when the He-Ne reference sinusoid crosses the zero level. By use of only positive zero crossings, the circuitry can develop one pulse per cycle of the reference interferogram (valid in the case of IFS 55 for the mounted He-Ne spectrum), or by use of all zero crossings for two pulses per cycle of this interferogram. The latter case is often called oversampling. These pulses trigger the A/D converter which immediately samples the main interferogram shown in the Figure 4.5.

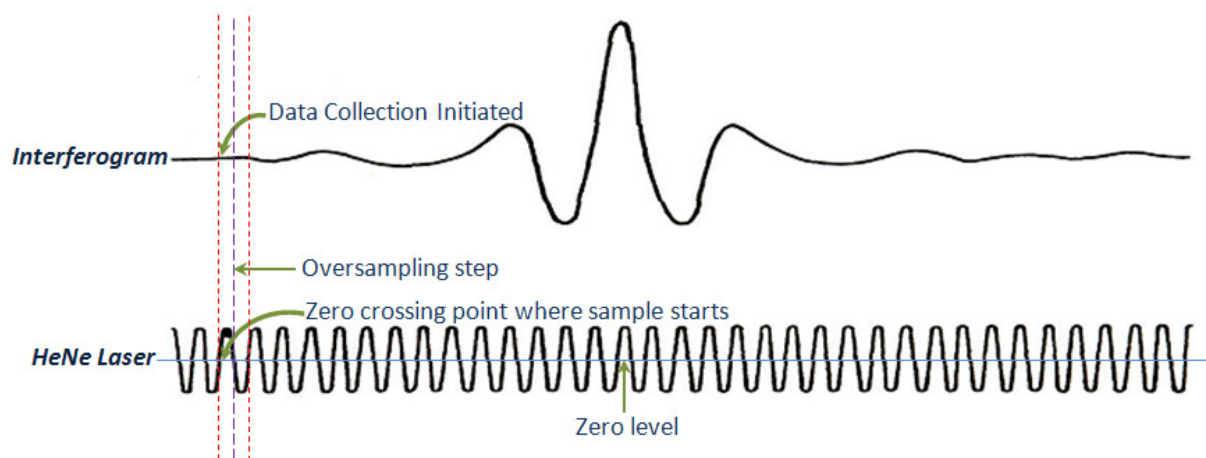

Figure 4.5: Sampling process to digitize data.

There is a fundamental rule called the Nyquist theorem which can be paraphrased to state that a sinusoid can be restored exactly from its discrete representation if it has been sampled at a frequency at least twice as high as its own frequency. If we apply this rule to the above formula we find immediately that since the minimum value of (f_r/f_i) is 2, so the minimum value of λ_i is twice the wavelength of the reference laser using the equation (4.4):

$$\lambda_{min} = 633 \text{ nm}*2 = 1.266 \ \mu\text{m}.$$

With oversampling, the reference laser wavelength is effectively halved. So in this case:

$$\lambda_{min} = (633 \text{ nm}/2)*2 = 633 \text{ nm}.$$

The oversampling can be incorporated in the IFS 55 upgrading firmware.

The alignment of the He-Ne laser beam inside the interferometer block is a vital issue since any small misalignment to the detectors (resides in the interferometer block) may ruin to create interferogram as the synchronization process of the moving mirror with the help of the He-Ne laser retardation stops. As shown in Figure 4.4(b), the circled three LEDs situated at the TC20 IFM board indicate the alignment of the He-Ne laser. If the He-Ne beam somehow becomes misaligned from its actual path

(parallel to the internal detectors mounted inside the interferometer block to precisely move the moving mirror) towards the interferometer block, the status of two red LEDs become ON. In this instance, changing the screws to the clockwise or anticlockwise direction shown at Figure 4.3.1 (c), misalignment problem can be solved. The status of red LEDs becomes OFF whenever misalignment problem mitigates.

4.3.2 Interferometer Compartment

Interferometer compartment of IFS 55 consists of source housing, source collection and a focusing mirror, an interferometer block along with a beamsplitter.

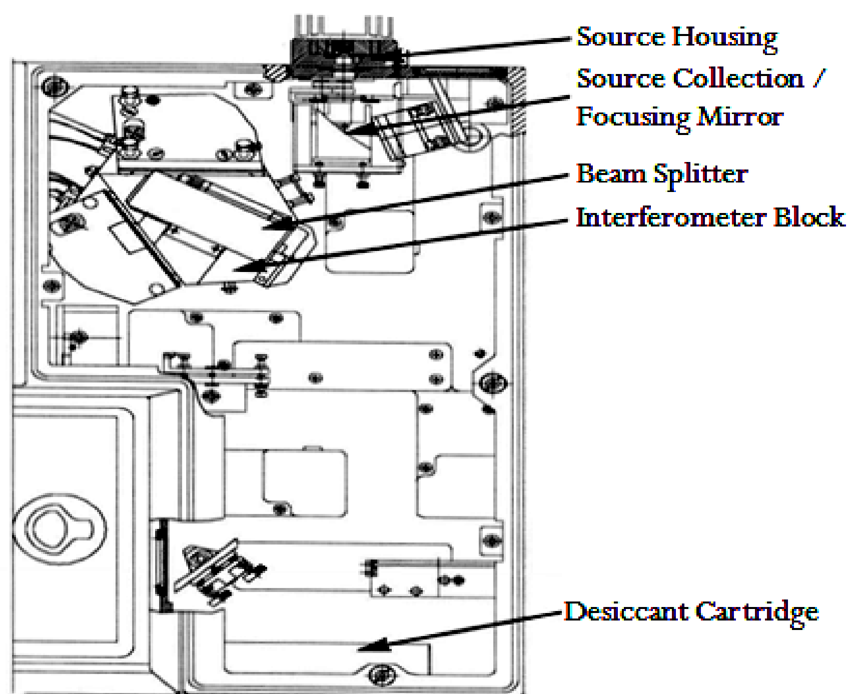

Figure 4.6: Schematic figure of the interferogram compartment.

IFS 55 FTIR spectroscopy is equipped with a single source attached to the back of the interferometer compartment. A manual aperture slide is installed within the compartment to regulate the source intensity. A heat sink is also attached to the back of the source housing. It uses the high efficiency NIR source with powerful collecting mirrors. The integrated aperture slide can be manually operated by using OPUS software from PC to obtain either the maximum resolution or the maximum count rate. A Quartz–Tungsten–Halogen (QTH) lamp is used as NIR source since it may run at significantly higher temperatures than mid-infrared sources and meet the photon flux required for the interferogram to fill the ADC at the centerburst and this is transparent across the entire NIR region. This NIR source is operated at a voltage less than their specified operating voltage indicating its long term operation stability. QTH lamps are more intense than tungsten light bulbs, but this intensity may sometimes lead to problems of digitization noise and response nonlinearity at detector.

The beamsplitter is made of a special material (Si on CaF_2 of which usual operation in between 1000 nm to 8333 nm). It transmits half of the radiation striking on it and reflects the other half. Radiation from the source strikes the beamsplitter and separates into two beams. One beam is transmitted through the beamsplitter to the moving mirror and the second is reflected off the beamsplitter to the fixed mirror (shown in Figure 4.7). The fixed and the moving mirrors reflect the radiation back to the beamsplitter. Again, half of this reflected radiation is transmitted and half is reflected at the beamsplitter, resulting in one beam passing to the detector and the second back to the source.

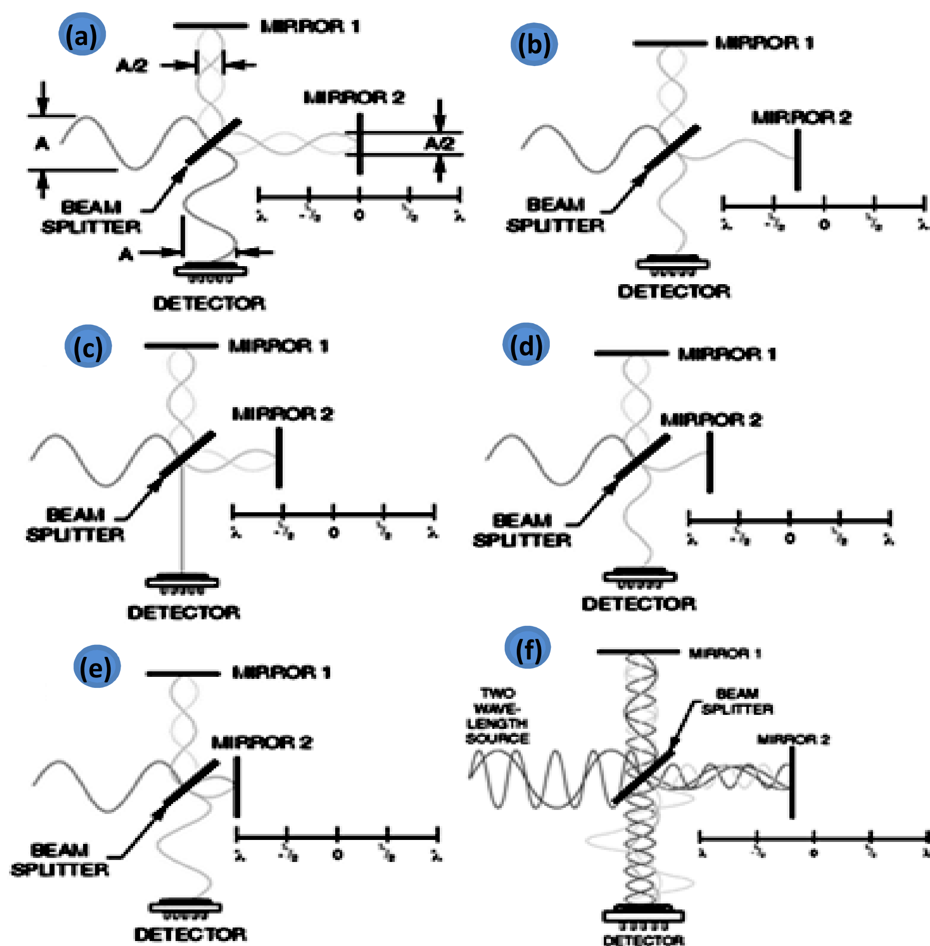

Figure 4.7: Schematic representation of waves and their phases, input, output, and the two arms of the interferometer as the scan goes from zero path difference condition to OPD=λ . (a) OPD=0 case. (b) λ/4 OPD case. (c) λ/2 OPD case. (d) 3λ/4 OPD case. (e) 1λ OPD case and (f) λ/4 OPD at two wavelength case.

Optical Path Difference (OPD) between the beams travelling through the two arms of an interferometer is equal to the product of the physical distance travelled by the moving mirror (multiplied by 2, 4, or other multiplier which is a function of the number of reflecting elements used) and n, the refractive index of the medium filling the interferometer block (air, nitrogen for purged systems, etc.). The raw FTIR data (Measured and ready for sending to PC) consists of a number of pairs of values (interferogram intensities, Optical Path differences).

FTIR has a natural reference point when the moving and the fixed mirrors are the same distance from the beamsplitter. This condition is called '*Zero Path Difference*' (ZPD). The moving mirror displacement, Δ, is measured from the ZPD. In Figure 4.7, the beam reflected from the moving mirror travels 2Δ further than the beam reflected from the fixed mirror. The relationship between the OPD and the mirror displacement, Δ, is:

$$OPD = 2\Delta n \tag{4.5}$$

Interferogram is the name of the signal format acquired by an FTIR spectrometer. It is usually significantly more complex looking than a sinusoid signal, which would be expected if only a single wavelength of light was present. Figure 4.8 is the interferogram of a broadband light source. The centerburst, the big spike in the center of Figure 4.8 is a telltale signature of a broadband source. Its origin lies in the fact that all wavelengths are in-phase at the ZPD. Therefore, their contributions are all at maximum and a very strong signal is produced by the system's detector.

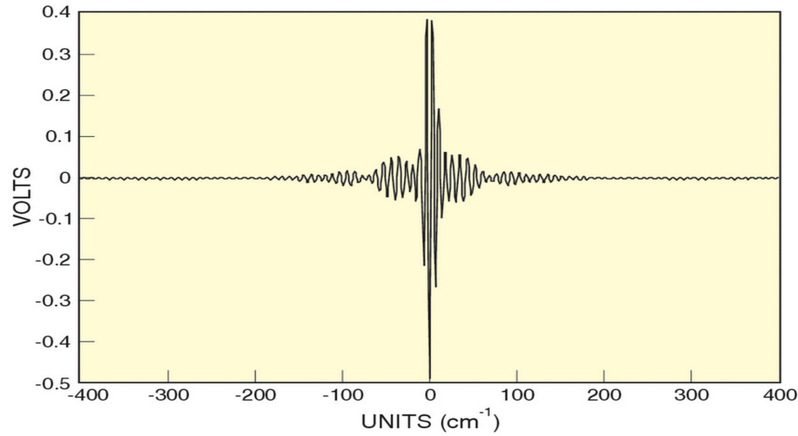

Figure 4.8: Broadband source interferogram.

As the OPD grows, different wavelengths produce peak readings at different positions and for a broadband signal; they never reach their peaks at the same time. Thus, as the moving mirror moves away from the centerburst, the interferogram becomes a complex looking oscillatory signal with decreasing amplitude.

The X-axis of the interferogram represents the optical path difference. Each individual spectral component contributes to this signal a single sinusoid with a frequency inversely proportional to its wavelength. This leads us to the definition of the unit of a spectral measurement. The wavenumber (cm^{-1}) represents the number of full waves of a particular wavelength per cm of length. The transformation of the wavenumber (cm^{-1}) to the wavelength (nm) can be done using the formula below:

$$\lambda(nm) = \frac{10^7}{cm^{-1}} \tag{4.6}$$

Once an interferogram is collected, it needs to be translated into a spectrum (emission, absorption, transmission, etc.). The conversion process is through the Fast Fourier Transform algorithm. The discovery of this method by J.W. Cooley and J.W. Turkey in 1965 [33], followed by an exponential growth of computational power at affordable prices, has been the driving force behind the market penetration of FTIR instruments.

A number of steps are involved in calculating the spectrum. Instrumental imperfections and basic scan limitations need to be accommodated by performing phase correction and apodization steps. These electronic and optical imperfections can cause erroneous readings due to different time or phase delays of various spectral components. Apodization is used to correct for spectral leakage, artificial creation of spectral features due to the truncation of the scan at its limits (a Fourier transform of sudden transition will have a very broad spectral content).

In processing of interferogram when the light intensity goes from one maximum of the interferogram to the next maximum, the optical path difference between the two legs of the interferometer changes by exactly one wavelength of the incoming radiation. To determine the wavelength of the incoming radiation, we can measure the frequency f_i or period $t_i = 1/f_i$ of the interferogram and consequently the wavelength is calculated using the following:

$$\lambda_i = V_o * t_i = V_o / f_i \tag{4.7}$$

where, V_o = the speed of the OPD change. The optical velocity is directly related to the speed of the scanning mirror. In IFS 55, the default optical velocities predefined by Bruker are 20 KHz, 10 KHz, 5 KHz and 2.2 KHz. For Bruker IFS 55, V_o is '*4*' integer multiple of the scanning mirror: $V_o = 4nV_m$,

where *n* donates the integer). However, the velocity V_m is needed to be maintained constant at all times with a high degree of accuracy. An error in the velocity value will shift the wavelength scale according to equation (4.7). Fluctuations in V_m may manifest themselves as deviations of the interferogram from a pure sine wave that in turn will be considered as a mix of sinusoids. In other words, there will be more than one wavelength in the incoming radiation. This behavior produces what are called “spectral artifacts”. And this complexity has been mitigated by inducing a reference signal using a He-Ne Laser that has already been discussed in section 4.3.1.

4.3.3 Detector Compartment

The IFS 55 detector compartment contains a DLATGS-detector and a Si/Ge detector (both of them integrated with a preamplifier) that have been installed in the detector compartment using a dovetail mount. This dovetail mount makes the detector easily replaceable. An automatic detector change option permits the selection of the detector position using OPUS/IR software.

The detector compartment contains a user replaceable molecular sieve cartridge that absorbs much of the water vapour present in the detector compartment. If the detector module 2 is selected using OPUS/IR software, beam entering through the window is reflected off by motor controlled flat mirror shown in the Figure 4.9 and then reaches the detector module 2 via the ellipsoidal mirror.

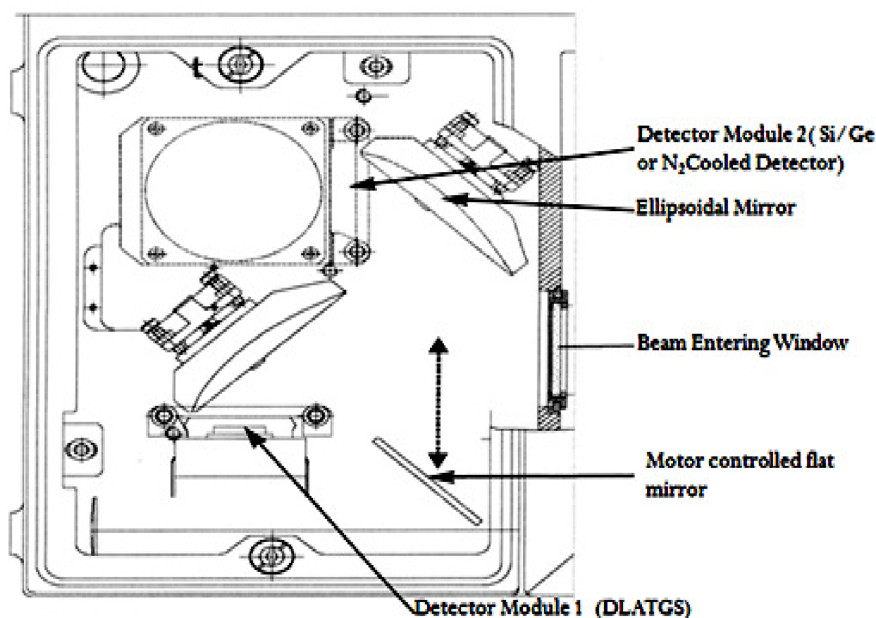

Figure 4.9: Schematic representation of detector compartment.

Detectors used in IFS 55 are basically two types: thermal detector (DLATGS) and quantum detector (Si/Ge detector or N_2 cooled PbSe detector). Thermal detectors operate by sensing the change in temperature of an absorbing material. Their output may be in the form of change in the resistance of semiconductor. The DLATGS detector incorporates a ferroelectric material that exhibits a large spontaneous electrical polarization at temperatures below its Curie point. If the temperature of the ferroelectric material is changed, the degree of polarization also changes. If electrodes are placed on opposite faces of a thin slice of material to form a capacitor, this change in polarization may be observed as an electrical signal. When the polarization changes, the charges induced on the electrodes can either flow as a current through a circuit of relatively low impedance or produce a voltage across the slice if the external impedance is comparatively high. DLATGS produces a signal only when the temperature of the element changes and is not very useful for measuring temperatures that do not

change. This type of detector is basically used for signal of mid-infrared region with low scanning velocity (~above KHz) due to a slow detecting response.

Quantum detectors (i.e. Si/Ge detector or N_2 cooled PbSe detector) are based on the interaction of radiation with the electrons in a solid, causing the electrons to be excited to a higher energy state (e.g., from a valence band to a conduction band of a semiconductor). The sensitivity of quantum detectors usually increases with wavelength (up to the cutoff), as the number of photons for a given amount of energy increases. Since the output is controlled by the number of electrons excited, the output voltage also rises with wavelength. When the wavelength approaches λ_{max}, the response drops off precipitously. This behavior is in contrast to that of thermal detectors, where the response per watt is constant. To use quantum effects for the detection of radiation, it is necessary to be able to excite electrons from one state to another state that has different electrical properties. Because high energies are required to release electrons from a photoemissive surface, this effect can only be used in the ultraviolet, visible, and near-infrared regions. This type of detector is suitable to detect signal evaluated from a higher scanning velocity (~above MHz).

4.4 Spectrum manipulation using OPUS/IR software

There are a number of techniques available to users of IFS 55 that help with both the qualitative and quantitative interpretation of spectra by the use of OPUS/IR software interface. During the measurement of FTIR spectra using the OPUS interface, it is really essential to configure parameters correctly in Advance Setup menu (shown in Figure 4.10).

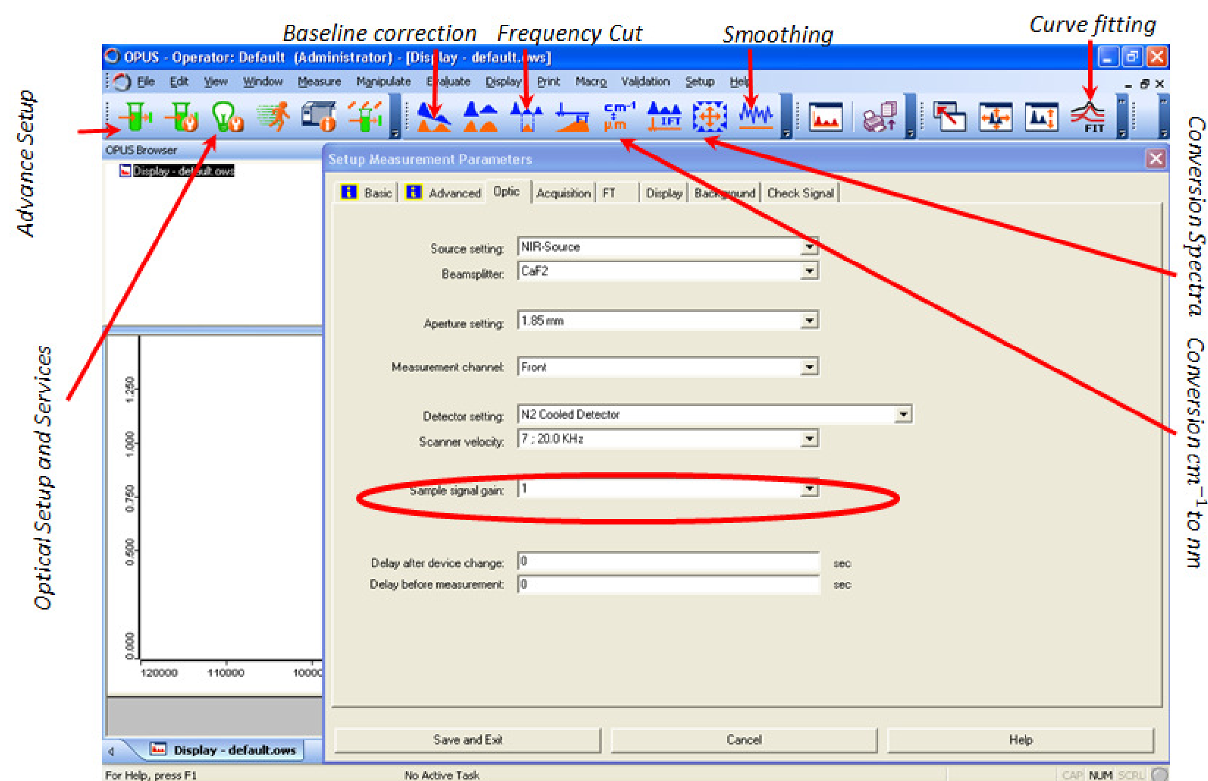

Figure 4.10: Opus/IR software interface.

As shown, in Figure 4.10, *'Optical Setup and Services'* menu is used to configure the hardware oriented configuration. Besides, *'Advance measurement'* menu is used to setup the parameters on measurement calibration. One important thing is that *'Sample signal gain'* (red circled) residing in *'Optic'* tab on *'Advance Setup'* has to be changed to *'1'* from *'Automatic'* as in the experimental setup discussed on Section 4.6 and Section 4.7, the mounted external detectors were incorporated with

external amplifier. If it is not being changed, a user may mislead from optical characterization since OPUS/IR can't recognize the gain factor induced by the external amplifier. A quick reference manual for IS absorbance study has also enclosed at Appendix C.

4.4.1 Baseline correction

It is a data manipulation technique usually used in quantitative infrared spectroscopy. In such manipulation, baseline is joined with the points of the lowest absorbance of spectra (preferably, in reproducibly flat parts of the absorption line). The absorbance difference between the baseline and the top of the band is then used.

4.4.2 Smoothing

'Noise' in a spectrum can be diminished by a smoothing data manipulating process. After a spectrum is smoothened, it becomes similar to the result of an experiment at a lower resolution. The features are blended into each other and the noise level decreases. A smoothing function is basically a convolution between the spectrum and a vector whose points are determined by the degree of smoothing applied. Generally, a degradation factor is required, which is positive integer. A low value, say one, produces only subtle changes, while a high value has a more pronounced effect on the spectrum.

4.4.3 Curve-fitting

Quantitative values for band areas of heavily overlapped bands can be achieved by using curve-fitting data manipulating procedure. One of these is based on a least-min-square algorithm. Least-square curve-fitting covers a general class of the techniques whereby one attempts to minimize the sum of the squares of the difference between an experimental spectrum and a computed spectrum generated by summing the component curves. Generally, the procedure involves entering the values of the wavenumbers of the component bands (determined by using derivative and/or deconvolution) and then the program determines the best estimate of the parameters of the component curves. Apart from the obvious variables of peak height and width, the type of band-shape needs to be considered. The class of band-shape of an infrared spectrum depends on the type of sample. A choice of Gaussian, Lorentzian or a combination of both is usually applied. However, MATLAB v.9 has been used extensively to manipulate the measured signals along this Opus/IR software.

4.5 External Detectors

During the experiment, instead of using the internal detectors (i.e. DLATGS and Si/Ge detector), we had to use several external detectors since the signal strength became so weak after the interferogram passing through the sample. During our experimental evaluation of GaN/AlN based IS absorbance and temperature dependent IS transition study, three different types of detector have been used. Initially for intersubband absorbance, JUDSON J16 series' Ge has been used that can detect photon from wavelength range 800 nm to 1800 nm. The maximum responsivity limit of this detector is less than 1 A/W. Another external detector was PGA20 Thorlab Inc. InGaAs photodetector and it has a detectivity range from 1200 nm to 2600 nm wavelength regime. Besides, it has a much higher responsivity like 1.12 A/W (max.) compared to the JUDSON J16 series' Ge. Besides, in temperature dependent study setup, another built in amplified PDT10DT Thorlab Inc. InGaAs photodetector was used which has photo sensitivity from 1200 nm to 2750 nm wavelength regime. This detector is enhanced with adjustable gain and adjustable bandwidth. User may vary the gain from 0 dB to 70 dB with the 10 dB step. However, the more information on such detectors has been included in Appendix B.

4.6 Absorption study setup

Even though BRUKAR FTIR spectroscopy IFS 55 has been used to measure the absorption study, the sample compartment had to be customized to assess the signal which is evaluated after the IR interferogram block. Since, the signal strength of sample (or, dummy) detected at internal detectors resided in IFS 55 detector compartment (i.e. DTGS, Si/Ge) became too low, an external detector had to be mounted just after the customized sample holder (shown in Figure 4.11 (a)). The placement of such sample holder in FTIR spectroscopy has been aligned in a way that the beveled 45^0 face of sample (or, dummy) become parallel to incident beam coming from interferometer block.

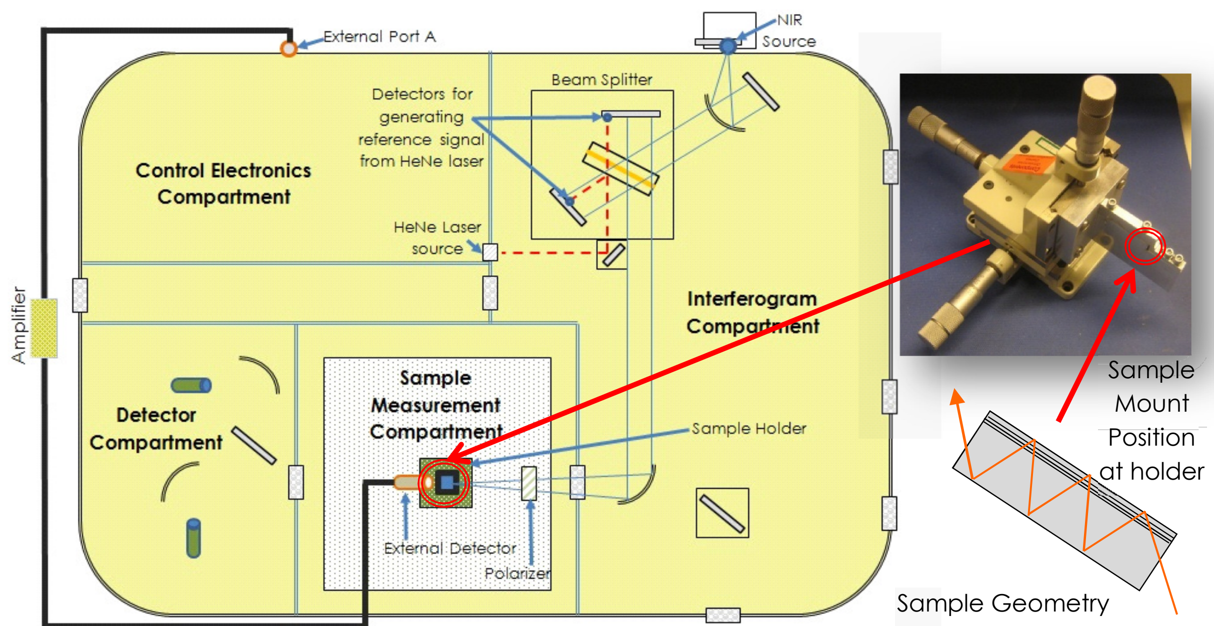

Figure 4.11 (a): Schematic figure of absorption study experimental setup.

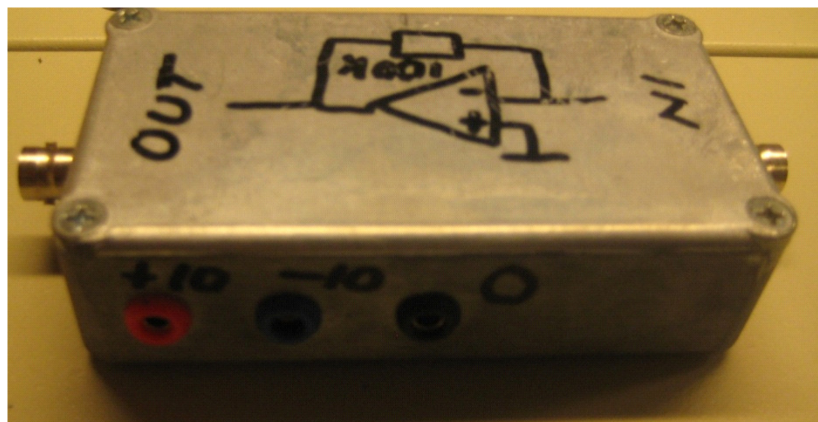

Figure 4.11 (b): The external amplifier.

The sample holder is made of three screw-gazes that help define the actual placement of the sample by varying X, Y and Z coordinates (so that IR interferogram produced from interferometer compartment enters the sample in a perfect manner). A Thorlab Inc. linear polarizer (LPNIR100 [Appendix B3]) has also been mounted in the sample compartment before the sample holder for polarizing the light generated from the NIR source. The intersubband absorption can be identified by the difference in absorbance for transverse magnetic (TM) and transverse-electric (TE) polarized light. The intersubband absorption

occurs only for TM light (i.e. light with the electric field in the growth direction). As an external detector, JUDSON J16 Ge detector [Appendix B1.1] (later on, Thorlab Inc. PGA20 InGaAs detector [Appendix B1.3]) has been used in such experimental setup. This external detector has been connected to the IFS 55 external input signal port, 'External A'. To amplify the collected signal by the external detector, an amplifier has also been plugged in between the detector and the IFS 55 external input signal port. The signal amplifier has been designed using MC1741 OPAMP shown in Figure 4.11 (b).

The observable samples have been produced from sample's growth wafers following several steps. At beginning, the sample's growth wafers have been cut into a dimension of 5×8 mm^2 pieces. To form the multi-pass waveguide geometry, each of them has been polished at bottom as well as two beveled opposite edges. This geometry allows the light to be incident to one of the beveled edges and to pass through it by the application of total internal reflection several times. Finally, the light that leaves the sample at the other beveled edge is collected by the mounted external detector. The processing of a sample structure is to increase the interaction with the active layer and induces higher absorption (~about 10 internal reflections at the upper wafer surface of the sample). One drawback of such a structure is that it induces extra reflection due to difference in refractive index between the epitaxial layer and the substrate and consequently, creates the interference pattern. As reference, 5×8 mm^2 dimensional dummy sapphire (Al_2O_3) (without any epitaxial growth) samples have also been prepared following the same procedures. This dummy sample has been used to obtain the background signal (reference) for evaluating the absorbance spectra.

4.7 Temperature dependent study setup

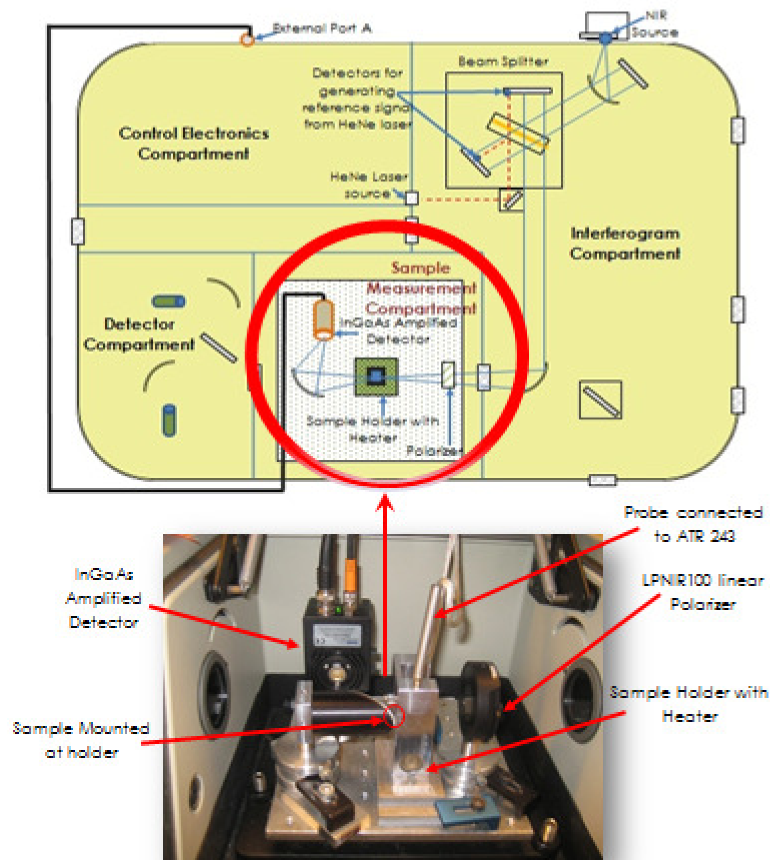

Figure 4.12: Schematic figure of temperature dependent absorption study experimental setup.

For the temperature dependent absorption study using a multi-pass waveguide geometry, a very similar experimental setup has been done except the employment of newly designed sample holder and built-in amplified external detector (PDT10DT external InGaAs amplified detector [Appendix B1.2]). This sample holder is quite different from the previous one since a thermostat has been embedded to vary the temperature. Due to the experiment requirement, the sample temperature has been varied from 25^0C to 400^0C within step increment of 50^0C. To do so, the PIXSYS ATR 243 [Appendix B2] was connected with a probe to the sample holder to regulate the temperature.

During this study, the Thorlab Inc. built in amplified InGaAs external detector has been employed to get signals coming from the sample. Since the detector diameter was of only 2 mm, it is necessary to use a confocal mirror to collect most light coming from the sample to the detector. This detector is then connected to the IFS 55 through the external input channel (external A) port. As InGaAs built in amplified detector operates at -10^0C [Appendix B1.2], therefore there is a huge impact of temperature at surrounding to do incessant accurate detection even though an advanced cooler is attached to it. To reduce the influence of the surrounding temperature, a thick paper board with a hole at the center is used just before the detector.

Background light (i.e. fluorescent light in the lab) always contribute to induce noise even at lower orders of magnitude. Therefore, all the absorption data has been collected in dark.

Chapter 5

5 Observation of intersubband absorbance in GaN/AlN MQWs

5.1 Structures of measured samples

GaN/AlN MQW structures were grown on GaN templates. The chosen templates were of 2.5 μm thick in which Si is doped at around $n = 3 \times 10^{18} \text{cm}^{-3}$ to form a contact layer. The schematic structures of optically characterized samples are shown in Figure 5.1.

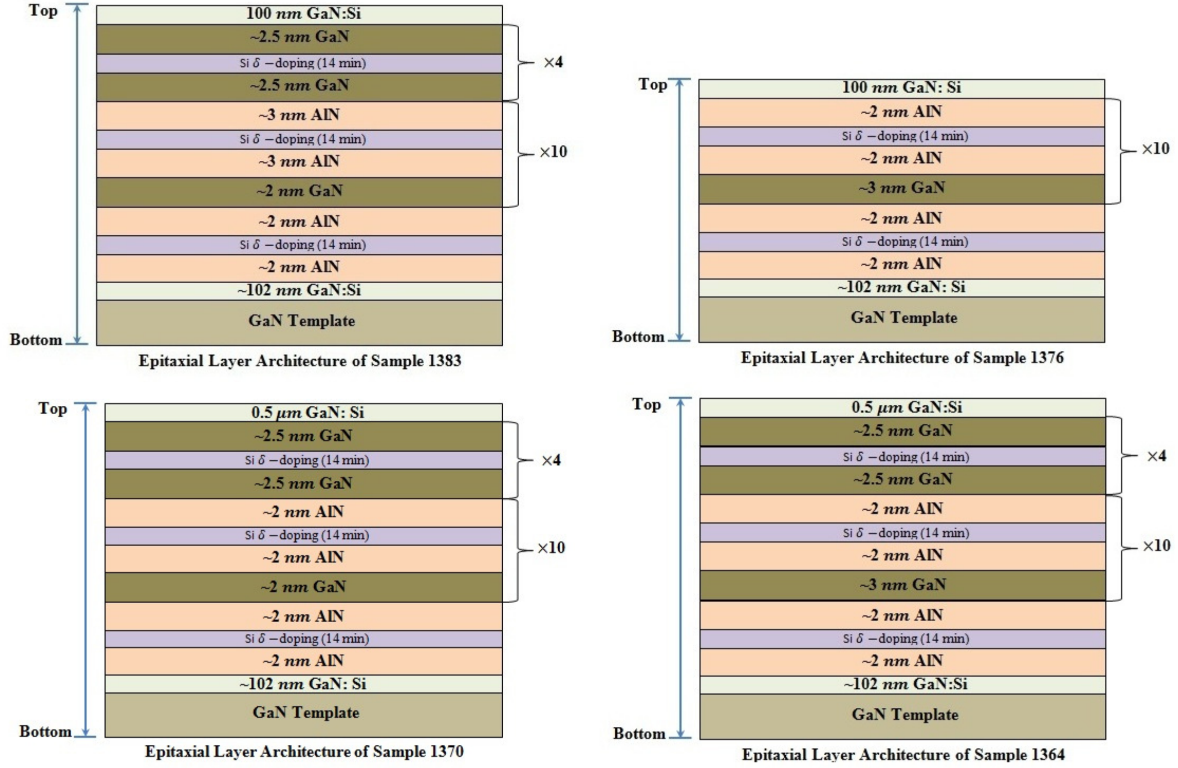

Figure 5.1: Structures of GaN/AlN MQWs.

The multiple quantum well was grown on top of ~102 nm thick GaN buffer layer where Si doping was $2 \times 10^{18} \text{cm}^{-3}$ and followed by several hundred nm thick $2 \times 10^{18} \text{cm}^{-3}$ Si doped GaN cap layer. In the MQW structure, GaN layers remain undoped. Si δ doping with a concentration of $3 \times 10^{18} \text{cm}^{-3}$ (in the AlN barrier layers) along with MQWs provides necessary electrons in QWs. The GaN and AlN widths determined by XRD are given at Table 5.1 below.

Table 5.1: GaN and AlN layer thicknesses measured by XRD.

Sample Number	Sample Name	GaN Well Width (nm)	AlN Barrier Width (nm)
1	S1364	3.4	4.1
2	S1370	2.5	4.1
3	S1376	3.1	2.8
4	S1383	2.7	2.8

5.2 Optical characterization

To obtain intersubband transitions in GaN/AlN MQW structures, optical measurements are executed by IFS 55 FTIR Spectroscopy. The experimental setup of this optical characterization has already been discussed in Section 4.6. We already know that absorption can only be achieved for the TM polarized light whereas there are no absorption spectra related to the TE polarized light. The study has been verified by measuring the absorption characteristics for both polarization modes for the GaN/AlN MQW sample S1370.

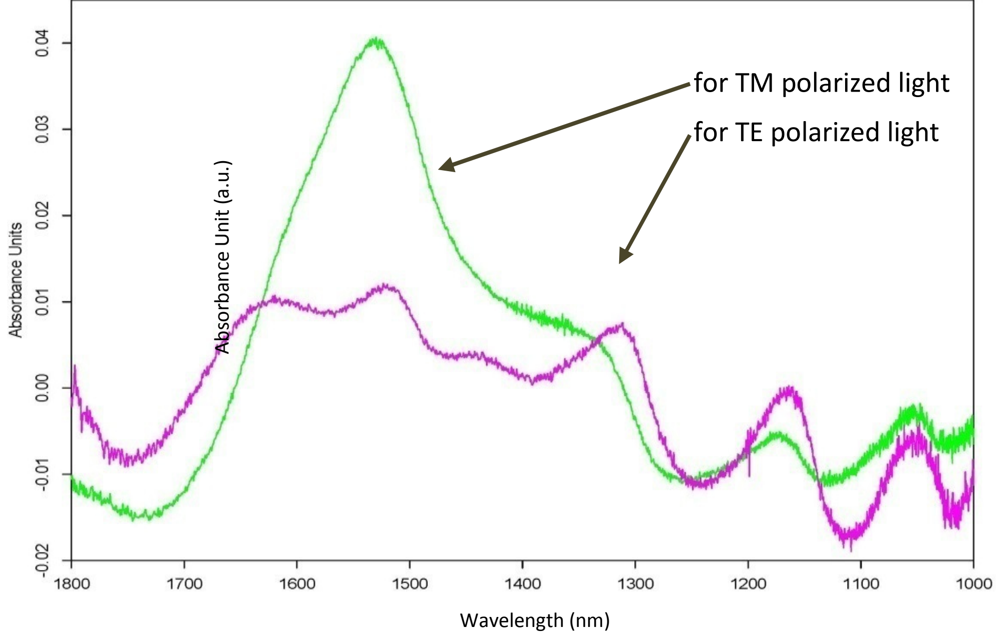

Figure 5.2: Measured FTIR Spectrum for sample S1370 using TE and TM polarized light.

By careful observations from Figure 5.2, it is noticed that there is a maximum absorption peak at 1534 nm wavelength (that corresponds to a strong absorption peak at 808 meV) for the TM polarized light and no significant absorption is shown for the TE polarized light. Therefore, this observation approves that the obtained peak is due to intersubband absorption. The presence of small peaks around the tail could be due to monolayer fluctuations or resonant standing waves occurred by the total internal reflections while broadband spectra pass through this multi-pass waveguide.

This absorption measurement obtained by FTIR is mostly known as absorbance and it can be defined by deriving the Beer–Lambert law [Appendix A1],

$$A = -log_{10} \frac{T_{sample}}{T_{reference}} \tag{6.2.1}$$

where, T_{sample} and $T_{reference}$ are the measured transmission spectra by IFS 55 FTIR spectroscopy of the sample (of GaN/AlN MQWs) and reference (Al_2O_3) respectively.

Initially, the absorbance spectra for samples (tabulated in Table 5.1) are measured by IFS 55 FTIR spectroscopy with an external detector (JUDSON J16 series' Ge detector) and has shown in Figure 5.3. From the Figure 5.3, it is quite clear that the IS absorbance for sample S1370 and sample S1383 is at 1534 nm and 1661 nm, respectively, but the IS absorbance for sample S1364 and sample S1376 are little ambiguous (in accordance to the observation of flatness nature in the IS absorbance spectra for both samples respectively). This limitation can be motivated by the responsivity limit of JUDSON J16 series' Ge detector in the wavelength range from 800 nm to 1800 nm (shown in Appendix B1.1).

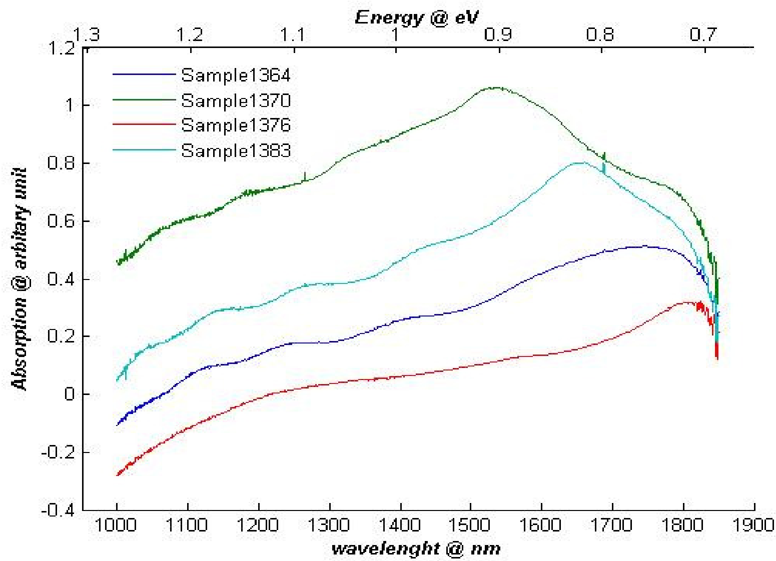

Figure 5.3: Measured absorbance Spectrum for samples using the JUDSON J16 series' Ge Detector.

To overcome this problem, an external InGaAs amplifier has been installed in place of the Ge detector since its responsivity covers the wavelength region from 1200 nm to 2750 nm. The measured IS absorbance spectra by the InGaAs detector are shown in the Figure 5.4:

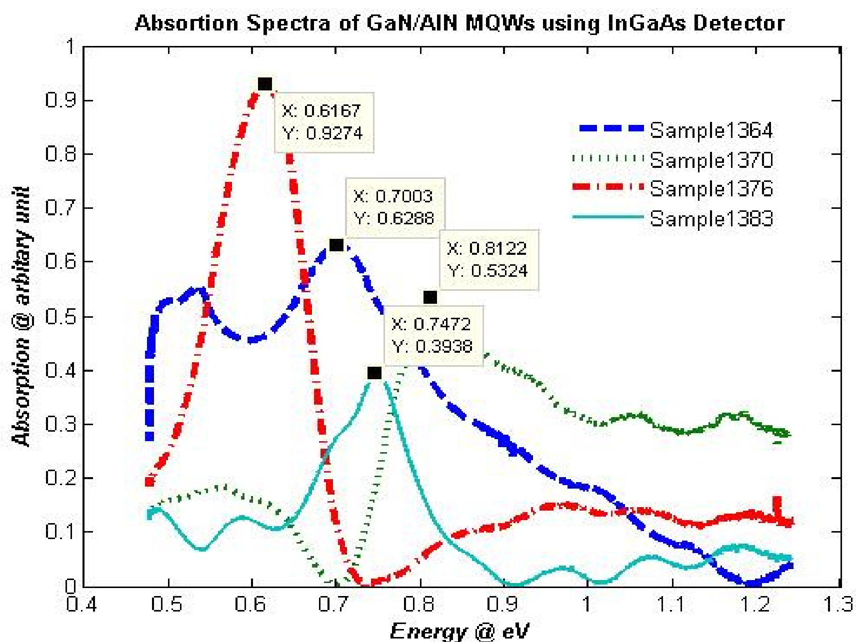

Figure 5.4: Measured absorbance spectrum for samples using the InGaAs detector.

When using an InGaAs detector (shown at Figure 5.4) instead of a Ge detector, the maximum peak absorbance for the sample S1370 and the sample S1383 becomes clearer compared with those in the Figure 5.3. Besides, it also could be highlighted that the maximum absorbance for the sample S1383 and the sample S1370 (at the wavelength 1.53 μm and 1.66 μm, respectively) corresponds very close to the QCL expected design of the operation wavelength (1.55 μm). Besides from these observations, it can be concluded that IS absorbance peak is strongly dependent upon layer thickness. Therefore, optimizing the layer thickness, the noble target can be achievable. To concrete the statement said just earlier, another investigation has been done by observing the FWHM of each sample.

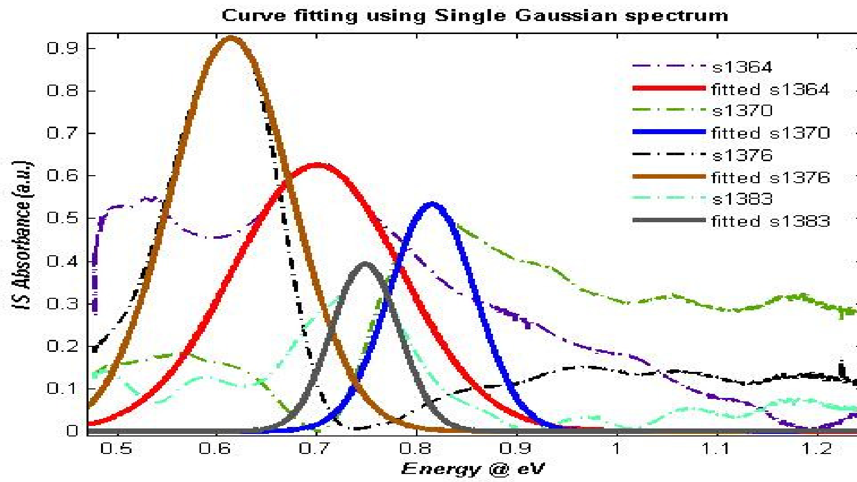

Figure 5.5: Fitted Gaussian spectra along with the IS absorbance of the samples.

To analyze FWHM, a single Gaussian curve has been chosen to fit (in Figure 5.5) the originally measured data from IFS 55 FTIR Spectroscopy using an InGaAs detector. The fitted intersubband transition energies correspond to the integer number of monolayers. The measured results together with the numerically evaluated results by the theoretical model (discussed in Section 3.3) are shown below.

Table 5.2: Summary of the IS absorbance results. Here, TBD means 'to be determined'.

Sample Number	Sample Name	IS Absorbance measured (eV)	IS Absorbance calculated (eV)	FWHM measured(eV)
1	S1364	0.7003	0.6900	0.2799
2	S1370	0.8122	0.7697	0.1435
3	S1376A	0.6167	0.6120	0.2026
4	S1376B	0.6243	TBD	0.2061
5	S1383	0.7472	0.7120	0.1126

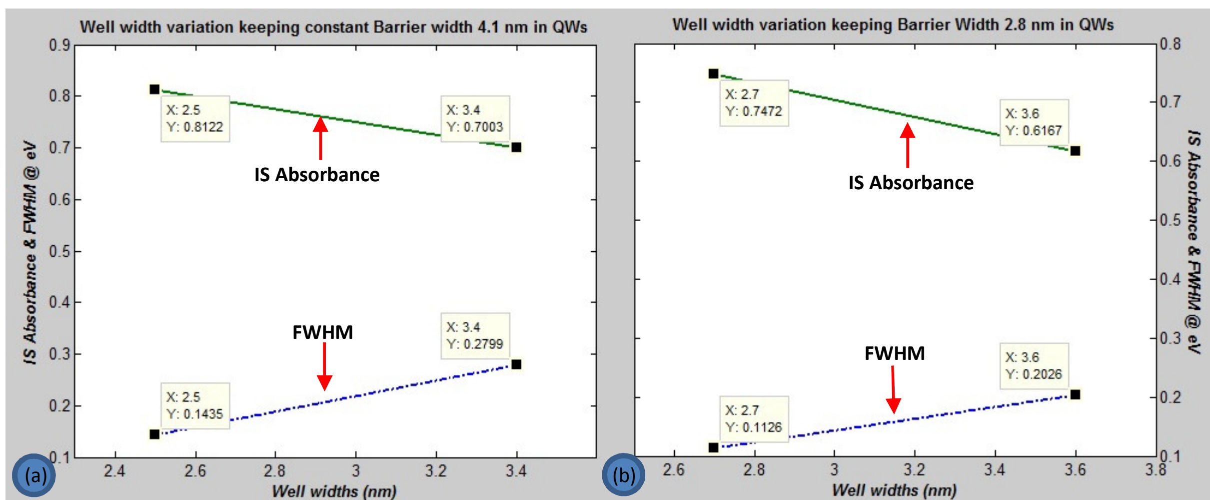

Figure 5.6: Measured IS absorbance peak and FWHM as a function of the well width keeping the barrier width constant (a) 4.1 nm [sample S1364 & sample S1370] and (b) 2.8 nm [sample S1376 & sample S1383] using the InGaAs detector.

Hereby, a new observation is committed by observing both the intersubband absorption (eV) and the FWHM (eV) utilizing the data from both Table 5.1 and Table 5.2. During the investigation, well widths have been varied keeping a constant barrier width (both for the case of 4.1 nm and 2.8 nm) as shown in Figure 5.6.

The well and barrier layers of the MQW structures will be initially biased because of the presence of polarization induced electric field which persuades triangular confinement potential profiles. The spontaneous and piezoelectric polarization effects become more dominant (consequently, induce larger electric fields and break the symmetry of the potentials) with increment of the well width in the MQW structures and so decrease intersubband absorbance energy (shown in the Figure 5.6 above). Besides, the thicker AlN barrier also increases the electric field in each well and it results in red shift of the ground state subband level due to the quantum confined stark effect.

In the same Figure 5.6, there is a clear trend of increment of FWHM with the increment of the well width (showing a good agreement to the relation of FWHM and IS absorbance coefficient at Eq. 3.7). However, a higher FWHM means a lower dephasing time of electrons in the excited subband (in agreement with Eq. 3.8) and consequently, makes the MQW structure more competent as a candidate for ultrafast intersubband device (i.e. THz optical switch). Hence, there will always be a tradeoff of achieving both of the maximum IS absorbance and the maximum FWHM from the same structure. However, an interesting and reverse observation is presented in a paper where the FWHM of GaN/AlN based device structures grown on GaN templates (quite similar structures as our observing samples) decreases with the increment of well widths [26]. The author proposed that this phenomenon is occurred due to the wide homogeneous broadening induced by enhanced electron-electron scattering process (due to the presence of layer roughness and atom diffusion at the GaN/AlN interface) and strong monolayer fluctuations when the well width is smaller. This disagreement to our experimental observations could be explained from the non-uniformity in epitaxial growth. 100% uniformity cannot be maintained all through the way from center to the edge (due to the non-uniform flux distribution and substrate temperature during growth process mainly) and so, IS absorbance peak positions as well as the values of FWHM may vary for different samples of the same structure but chosen from different locations of the grown wafer.

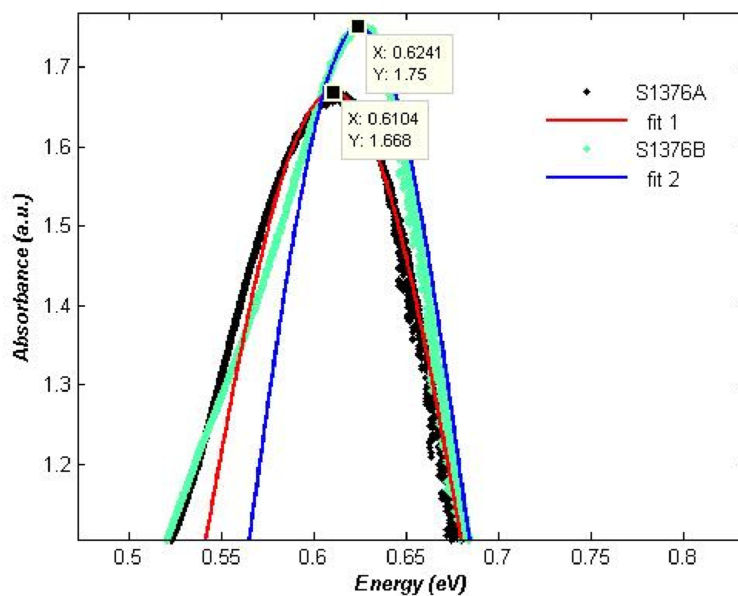

Figure 5.7: Intersubband absorbance of Sample S1376A and S1376B. S1376A and S1376B follows the same structure but chosen from different locations of the growth wafer.

To validate the prediction, two other samples (S1376A and S1376B) have been chosen to perform IS absorbance study where both of them have taken from the same wafer but from different locations. By observing Figure 5.7, it can be clearly stated that the IS absorbance as well as the linewidth vary even for the same structures but taken from two different locations. Similarly, another study of the same author [26] on a GaN/AlN MQW structure grown on a sapphire substrate has shown that there was a variation by 0.27 meV/mm, 0.52 meV/mm and 0.003 mm^{-1} along the 20 mm line across the wafer for IS peak energy, FWHM and absorbance, respectively [27].

Chapter 6

6 Temperature stability of intersubband transition in GaN/AlN Quantum wells

III-N heterostructures have already put a pioneer foot step in developing blue and ultraviolet light emitting diode, laser diodes as well as high temperature/power electronics. In this respect, GaN/AlN based MQW heterostructures are nothing but outstand research competent because of one of their most renowned features, intersubband transition. As this type of heterostructures consists of very large conduction band offset (~2eV), they show significant impending at wide fiber-optic telecommunications by utilizing the intersubband absorption property in the near infrared region. One interesting phenomenon, enhanced electron-LO phonon interaction (occurred in intersubband transition in highly ionic heterostructures) plays the major role to design ultrafast all optical Tbit/s switch (as the recovery time after IS transition is 140-370 fs, and it is order of magnitude shorter than other conventional semiconductor laser structures) [29]. In other word, this enhanced electron-LO phonon interaction can be a threat for any type of structure operated at higher temperature since it helps to assure significant heat radiation. At higher temperature operation, electron-LO phonon interaction rate increases due to the decrease in energy bandgap in device structure [31]. To investigate such an effect on GaN/AlN based MQW heterostructures, temperature dependent IS absorption study is committed experimentally.

As in Section 4.7 where the experimental setup has been stated already, experiments have been performed by polarizing the light in the TM mode using Thorlab Inc. linear polarizer. The measurement is done at room temperature (25^0C) as well as at elevated temperatures in an interval of 50^0C from 50^0C to 400^0C. During the measurement, hysteresis study has also been conducted for each sample. For performing the optical characteristics on such samples, sapphire (Al_2O_3) has been used as dummy samples as background reference. The peak absorbance is hauled out from the measured spectra using curve fitting tools in MATLAB interface.

From Figure 6.1 (a) and (b), it is clearly visualized that a very small red shift occurs (~2.2 meV) in IS absorbance peak for temperature variance from 25^0C to 400^0C. This shift remains the same for hysteresis observations as well. During observation, the sample holder temperatures have been calibrated within approximately $\pm 5^0$C. The small redshift occurred in Figure 6.1 can be described from the thermal effect in band offset as well as a huge internal electric field induced by high ionic property of GaN/AlN QW heterostructures. This internal electric field creates an exceptionally large spontaneous and piezoelectric field. And this enhancement of piezoelectric effect occurs due to the enhanced strain component like lattice mismatch strain or thermal strain where both of them are induced because of thermal expansion of the substrate and epitaxial layer at higher temperatures.

To signify the obtained outcome from the experiment, it is always wise to correlate them with theoretical expectations. And so, self-consistent solution is designed by the use of Schrödinger-Poisson equation for conduction band electrons. Temperature effects of such heterostructures have been modeled by the count of AlN and GaN band gaps, thermal expansion influencing piezoelectric fields and two dimensional Fermi distributions of electrons. Among these parameters, the band gap parameter affects a lot to the shift of the peak position while the strain induced piezoelectric effect is significant. In the design of theoretical modeling, redistribution of electrons has been ignored since a large intersubband transition occurs on such heterostructures.

Varshni relation has been added to see the change in band gap to fix the conduction band offset at all temperatures:

$$E_g(T) = E_g(T = 0) - \frac{\alpha T^2}{\beta + T} \quad (6.1)$$

where the Varshni parameters α and $\beta$for AlN and GaN are quite different from each other. For GaN, $\alpha_{GaN} = 0{,}914\ \text{meK}^{-1}, \beta_{GaN} = 825$ K whereas for AlN, $\alpha_{GaN} = 2.63\ \text{meK}^{-1}, \beta_{GaN} = 2082$ K.

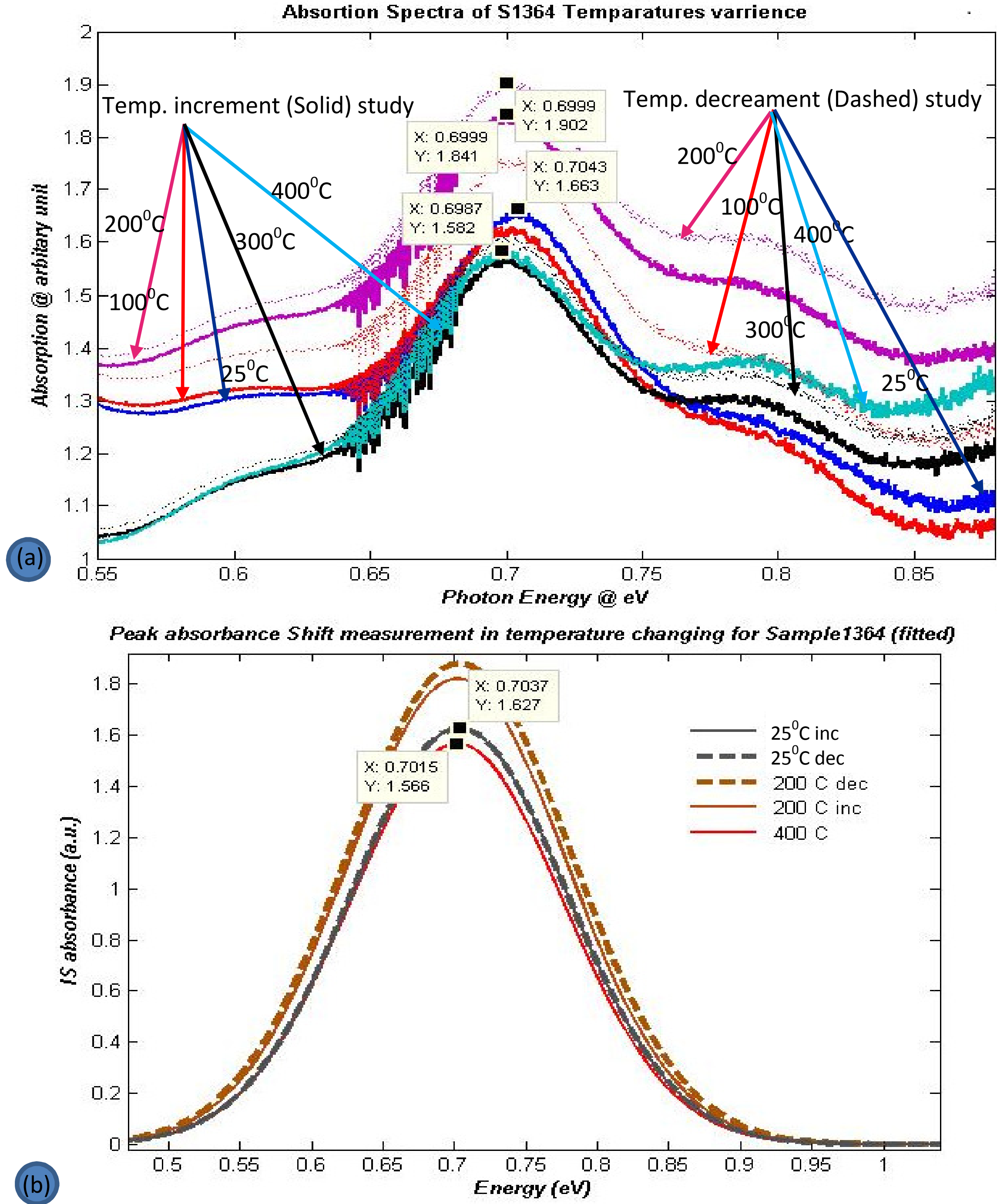

Figure 6.1: Temperature dependent hysteresis study on sample S1364 (a) before fitting and (b) after fitting.

Along with the solution of Schrödinger equation, depolarization and excitonic effects have also been included by considering the full structure at equilibrium (with the presence of a common Fermi level, i.e. shown in Figure 6.2.b). Hereby, to investigate the intersubband absorbance, an adequate unit cell size is chosen to achieve the bulk like behavior for the full structure even far from the central cell. However, it is necessary to consider the full structure since there may have been the probability of

distorting or depleting the active part of the QW structure due to the presence of a huge electric field. The reason behind such an approximation could be demonstrated from the following Figure 6.2.

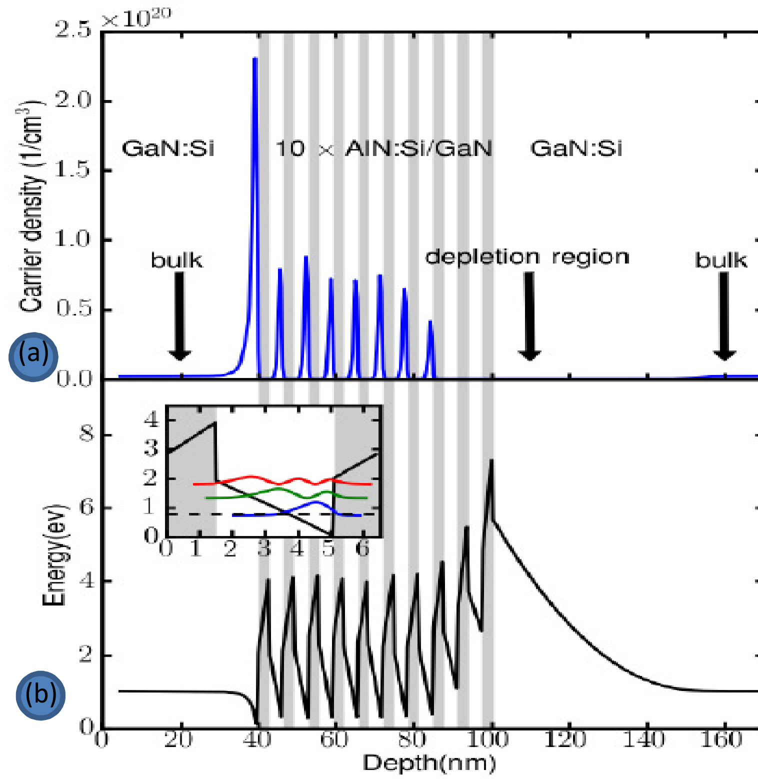

Figure 6.2: Schrödinger and Poisson equations solved (a) carrier density profile and (b) energy density profile of GaN/AlN based ten periods of MQW structures (Sample S1376A) with a doped AlN barrier (gray background) and a GaN cap layer [29].

In Figure 6.2, the carrier density and the energy profile have been illustrated through the solution of Schrödinger–Poisson equation for Sample S1376A. In Figure 6.2 (a), the light gray background indicates the position of the AlN barrier and the two dimensional electron gases are formed. Hereby in Figure 6.2 (b), a long electrostatic tail depletes electrons in the conduction band at the right side of the AlN/GaN interface. In a more insightful observation in Figure 6.2 (a), though it could be seen that the two rightmost wells are completely depleted and the third rightmost is partially depleted, the rest of them repeat themselves steadily having approximately the same IS absorbance spectra (Figure 6.2 (a)). Therefore, the solution based on the single unit well assumption was fairly enough. In Figure 6.2 (b), along the whole potential profile of the AlN/GaN MQW structure, confined energy states are demonstrated in the inset where three lowest energy states are drawn along with the Fermi level at room temperature (dashed line).

Table 6.1: Measured and calculated IS absorbance. Here. TBD means ‘to be determined’.

Sample Name	IS Absorbance measured (eV)	IS Absorbance calculated (eV)
S1364	0.704	0.690
S1376A	0.626	0.612
S1376B	0.6243	TBD
S1383	0.739	0.712

The observed and calculated peak positions at room temperature are shown in Table 6.1. It is worth to mention that solving Schrödinger equation involves the finite difference method that includes the non-parabolicity correction [29]. The strong non-parabolicity coupled band filling is the main reason for the redshift of IS absorbance. Strong non-parabolicity leads to a significant decrease in transition energy with the increment of the wave vector. Hence, this combination causes the reduction at IS peak absorbance with increment of temperature [30]. The absorbance peak shift is summerized in Figure 6.3.

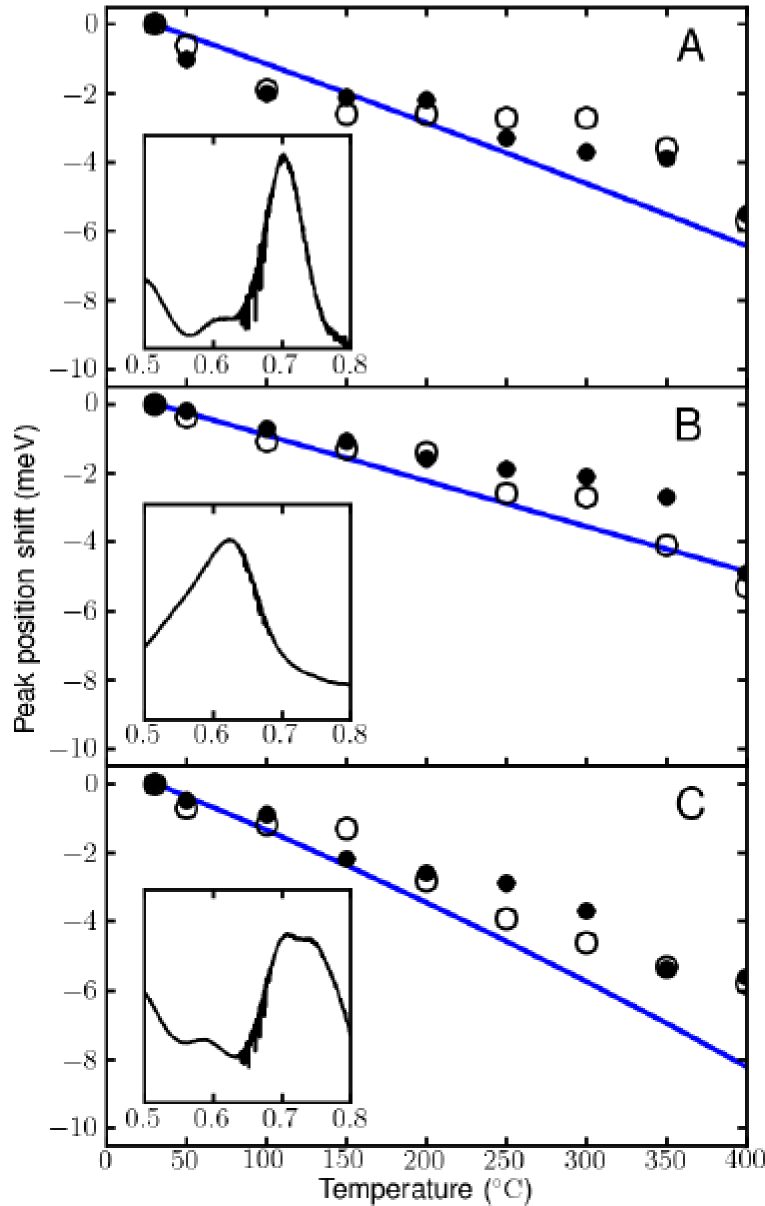

Figure 6.3: Temperature dependent IS absorbance peak shift for sample S1364, sample S1376A and sample S1383 (top, middle and bottom, respectively). The experimentally obtained peak energy shift relative to that at room temperature are presented by filled circles and the open circles represent the results for the decrement in sample temperature. The solid line represents the theoretical IS absorbance at various temperatures. The insets represent the measured room-temperature absorption spectra for the samples [29].

In the above figure, it is understood that good coincidence resides between the experimentally and the theoretically evaluated data. The experimental peak positions shift by ~ 6 meV as temperature is increased from room temperature to 400^0 C. Hereby, there is a comparatively poorer correspondence for sample S1383 and this could be due to the presence of a double peak. Based on our calculations,

we attribute multiple peaks to mono-layer fluctuations. An one mono-layer thinner (wider) shifts the calculated (using our theoretical model) peak position by 40 (30) meV. This shift explains the shape of the spectrum in the inset of Figure 6.3. The temperature-dependent shift in transition energy is mostly affected by the shift in band offset, but the strain-induced piezoelectric effect is also essential. By only including the temperature dependent band offset in theoretical model, it is obtained that 60, 67, and 80 % of the full energy shift for sample S1364, S1376A and S1383 is due to the temperature dependent band offset. The higher percentage for sample S1383 can be described from a larger penetration into the left AlN barrier, and so, an increased sensitivity to the band offset. The remaining 20% of the shift come from the piezoelectric effect.

Summary

7 Summary and future direction

7.1 Summary

Throughout this thesis, a long and effective experiment procedure has been followed to observe heterostructures' (mainly GaN/AlN MQW based QCL device structures) optical properties. An effective investigation on design and optimization parameters has been done by characterizing the intersubband transition using Bruker IFS 55 Fourier transform infrared spectroscopy. Due to the absence of proper hardware manual on such an instrument, it has been challenging for doing additional modifications to get IS absorbance spectra from GaN/AlN MQW QCL device structures. A depiction of instrumentation with the experimental setup on IS absorbance observation has been included here and also a clear operation procedure of IFS 55 spectroscopy has been described. During the observations, it has been found that the device structures' IS absorbance property vastly depends on layer thickness. The combination of a small GaN well width and a wide AlN barrier width leads to the red shift on IS peak absorbance for such GaN/AlN MQW based device structures. Specially, some fabricated samples (i.e. sample S1370A and sample S1383) have already shown promising results of having IS absorbance at the expected wavelength for optical fiber communication appliances ~1.55 μm. But it is worth to remember that the small well width means the more influence from monolayer fluctuations that may induce interface dislocations in device structures. Enhancement of the electron-LO phonon interactions that occurs in the IS transition at higher temperatures (in highly ionic heterostructures) could be a threat as it induces heat significantly as consequences. Hereby, the temperature dependent experimental study on GaN/AlN MQW based device structures have been committed and it has been found that only ~6meV red shift occurs at a much higher temperature (400^0C) for the sample A compared to the peak at room temperature. Later on, these results were also verified with the calculations using the theoretical model. Hence, this temperature insensitivity for the intersubband transition energies in GaN/AlN MQWs signifies them very promising materials for QCL devices.

7.2 Future direction

It's really nice to write something about the future direction of the thesis work but honestly, it's also quite tough to concise all possibilities in my case as FTIR spectroscopy as it can be utilized several ways to obtain various information of this device structure. The photoemission study is the current requirement of newly developed samples of QCL device structures. To obtain photoluminescence measurement, IFS 55 FTIR spectroscopy will definitely be a good option since it is really quick and easy to measure the optical characteristics. As it is known, photoluminescence measurements require optical excitation on the device structure and so an external high power laser (i.e. Ar^+ laser) will be needed in the experimental setup. A tentative experimental setup is proposed in the Figure 7.2. There are some challenges that have to be overcome regarding this setup to be fully functional. One of them may be the strong laser beams' (i.e. HeNe laser and Ar^+ laser) inclination to N_2 cooled InSb detector along photoemission spectra from sample that may saturate the detector. Hence, a suitable attenuator can be used to scale down the signal strength of a strong incident flux (specially suppressing the Ar^+ laser before entering the interferometer block). Besides, the photo emitted spectra from sample have to be aligned intuitively to form a (as accurate as possible) parallel beam entering FTIR using several lenses and mirrors. Hereby, each of the optical components (i.e. lances and mirrors) will contribute in loss of photon even if in small scale. Therefore, there may have a good probability of reaching very

low signal (after suppressing HeNe laser and Ar^+ laser contribution at interferogram using filter) to N_2 cooled InSb detector at end. Hence, very high resolution (i.e. 0.2 cm^{-1}) setting with so slower scanning velocity (preferably, the step scan) can be the solution in that case to obtain spectra. However, step scan spectrometry solution from Bruker for IFS 55 is not available anymore and the lowest predefined scanning velocity of IFS 55 is 2.2 KHz. In this circumstances, modification of the provided OPUS/IR software by integrating a new script (may be developed by low level language i.e. C/C++, assembly language) that will control the speed of motor (used in moving the moving mirror in the interferometer block) with the concern of Bruker Inc. can also be another solution for achieving lower scanning velocity.

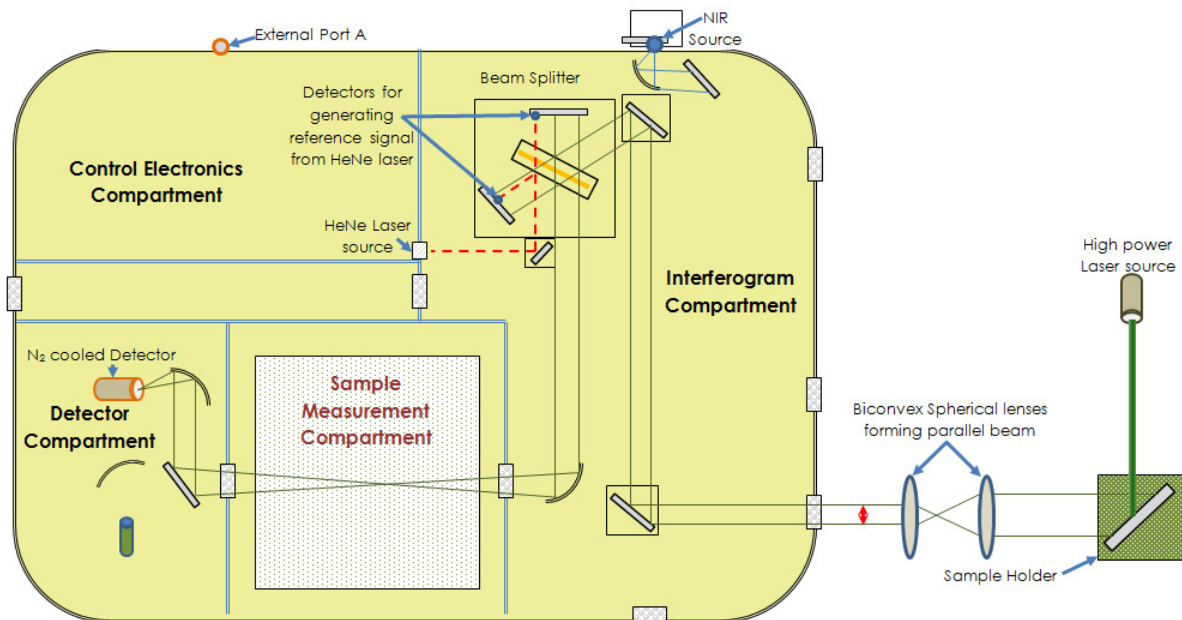

Figure 7.2: Proposed schematic setup for photoluminescence measurement using IFS 55 FTIR spectroscopy.

Mechanically induced strain effect on GaN/AlN based MQW heterostructures can also be studied through FTIR.

Appendix A

A1 Beer–Lambert law

The Beer–Lambert law is used to relate the amount of light transmitted by a sample to the thickness of the sample. The *absorbance* of a solution is directly proportional to the thickness and the concentration of the sample, as follows:

$$A = \varepsilon c l \tag{A1.1}$$

where A is the absorbance of the solution, c the concentration and l the pathlength of the sample. The constant of proportionality is usually given the Greek symbol epsilon, ε, and is referred to as the *molar absorptivity* The absorbance is equal to the difference between the logarithms of the intensity of the light entering the sample (I_0) and the intensity of the light transmitted (I) by the sample:

$$A = \log I_0 - \log I = \log (I_0/I) \tag{A1.2}$$

Absorbance is therefore dimensionless. *Transmittance* is defined as follows:

$$T = I/I_0 \tag{A1.3}$$

and percentage transmittance as:

$$\%T = 100 \times T \tag{A1.4}$$

Thus:

$$A = -\log (I/I_0) = -\log T \tag{A1.5}$$

When using percentage transmittance values, it is easy to relate and to understand the numbers. For example, 50% transmittance means that half of the light is transmitted and half is absorbed, while 75% transmittance means that three quarters of the light is transmitted and one quarter absorbed.

The Beer–Lambert law tells us that a plot of absorbance against concentration should be linear with a gradient of εl and will pass through the origin. In theory, to analyse a solution of unknown concentration, solutions of known concentration need to be prepared, a suitable band chosen, the absorbance at this wavenumber measured, and a calibration graph plotted. FTIR spectrometers have accompanying software that can carry out these calculations. Quantitative measurements need to be carried out on absorbance spectra. Thus, transmittance spectra need to be converted to absorbance spectra.

Appendix B

B1 External detectors

B1.1 External germanium detector

JUDSON J16 series' Ge has been used in the IS absorbance experimental setup. This detector can operate up to 60^0 C in smooth condition. It may accumulate photon response from the wavelength range 800 nm to 1800 nm whereas it's maxumium responsivity appears at 1300 nm.

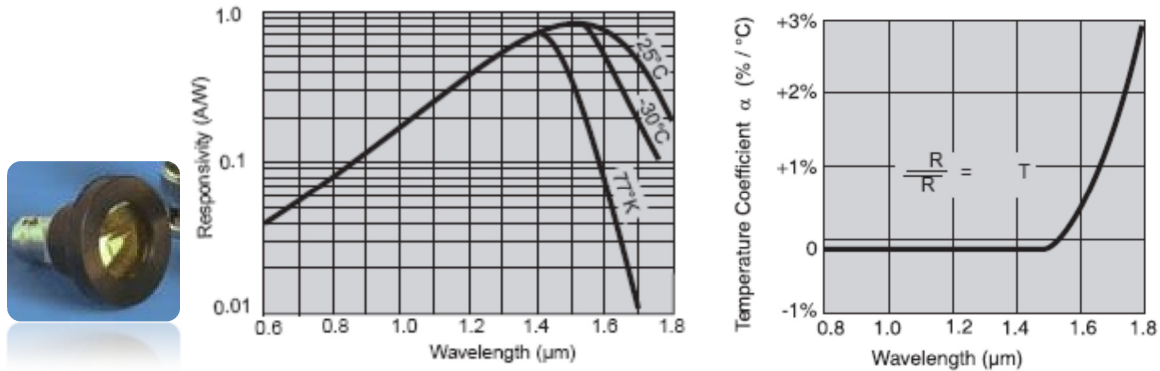

Figure B1.1: External Germenium Detector and its responsivity and thermal coefficient response curve.

Its diameter is about 10 mm wide and it is designed for low frequency application. It offers the highest shunt resistance and DC average power. It offers the highest shunt among all available JUDSON series Ge photodiodes that alternatively means to provide the lowest DC drifts. Its low reverse bias limit enables its operation above ~1 KHz. Temperature changes have little effect on this kind of detector responsivity (shown in Figure B1.1). Likewise, the temperature coefficient is less than 0.1% per ^{0}C at 1.2 μm whereas at 1.7 μm, this coefficient becomes approximately 1.5% per ^{0}C. Besides, it has already been mentioned that this detector can operate smoothly in the temperature range of -40^{0}C to 60^{0}C. Therefore, it is really a good candidate to measure the temperature dependent experimental study.

B1.2 PDT10DT external InGaAs amplified detector

In the temperature dependent experimental setup, this external InGaAs detector has been used. This Thorlab Inc. solution consists of nice temperature controlling, adjustable gain and adjustable bandwidth. It may accumulate the data of a wide optical wavelength (1200 nm to 2750 nm) range. Two eight-position rotary switches allow the user to vary the gain from 0 dB to 70 dB with the 10 dB step.

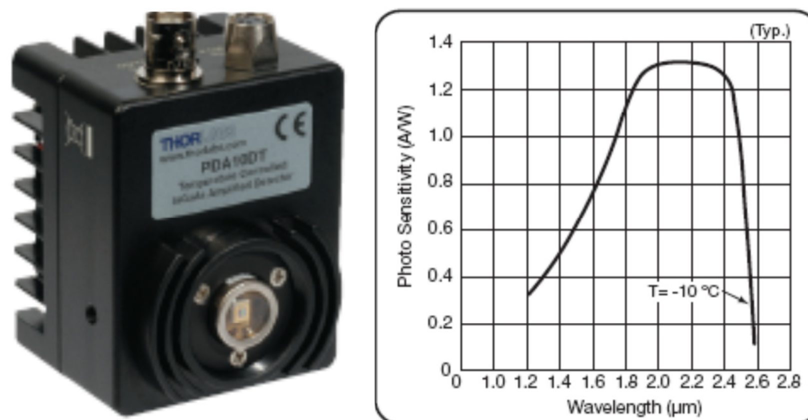

Figure B1.2: PDT10DT external InGaAs amplified detector.

It also allows user to select the bandwidth setting. This self-consisting amplified detector is ease to detect the low signal passed from experimental samples and it drives 50Ω load along with impedance

up to 5 volt. It performs its best at 0dB and 10 DB gain. It is equipped with a low pass filter that allows the frequency setting varied from 500 Hz to 1MHz (in 8 steps). But one noticeable factor is that the gain bandwidth decreases as the gain factor increases. Therefore, at 70dB gain, 1 MHz won't provide the perfect 1MHz according to the device specification. Besides, this detector is also mounted with a thermoelectric cooler so that the amplifier can be operated at -10^0 C (with the thermistor feedback to stabilize the temperature) incessantly. The temperature variance surrounding the sample compartment also plays a vital role since the thermoelectric current (at its limit ~820 meV) will be localized inducing offset and output noise if the sample compartment becomes too hot.

B1.3 PGA20 InGaAs detector

Likewise, PGA20 InGaAs photodetector has also been used in the IS absorbance experimental setup as JUDSON J16 series' Ge. Even though this PGA20 Thorlab Inc. photodetector is not equipped with a built in amplifier; it has a high responsivity range from 1200 nm to 2600nm.

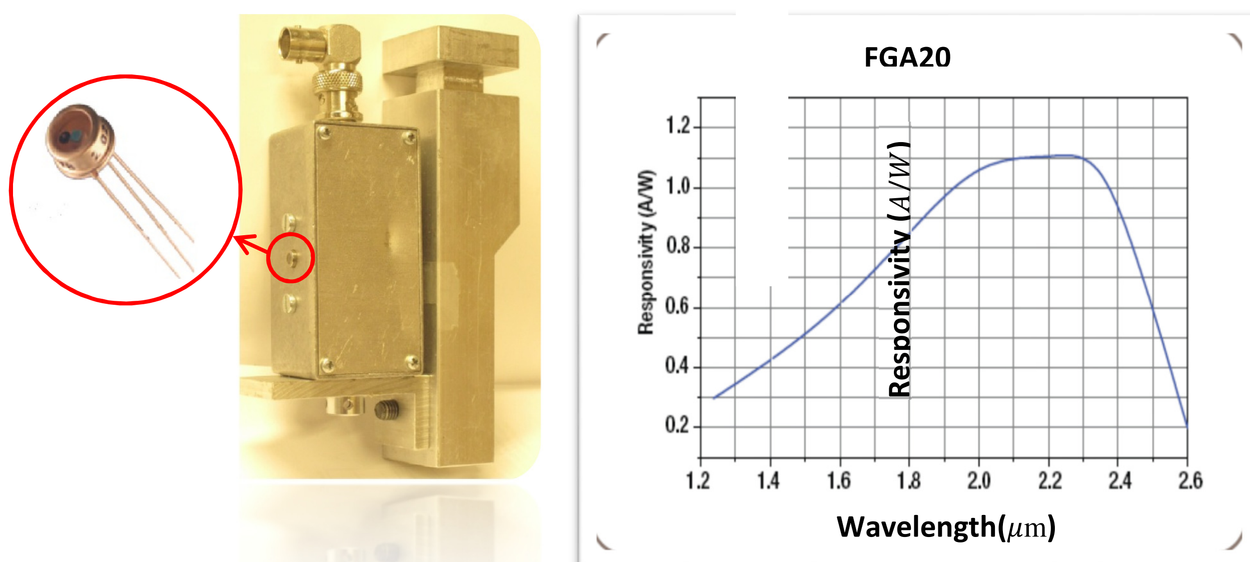

Figure B1.3: External dismounted InGaAs detector and its responsivity response curve.

It has added a figure of merit in our experimental study, since some studied samples have the peak absorption energy around 2000 nm wavelength and that is out of the detecting limit of JUDSON J16 Ge detector (as discussed above). The noticeable drawback of such detector is that it is of only 1 mm diameter that makes complexity for mounting it perfectly according to the experiment requirement and also leads to a loss of photons as all lights cannot be accommodated or perfectly coincide using convex mirrors/lenses.

B2 Automatic temperature regulator (ATR)

For assessing the temperature dependent absorption, a variable temperature regulator has been used. To accurately control the temperature without extensive operator's involvement, a temperature control system relies upon a controller, which accepts a temperature sensor such as a thermocouple or RTD as input. It compares the actual temperature to the desired control temperature, or set-point, and provides an output to a control element. The controller is one part of the entire control system, and the whole system should be analyzed in selecting the proper controller. In this case, PIXSYS ATR 243 has been used for the purpose that is capable of keeping temperature ±10 ^{0}C.

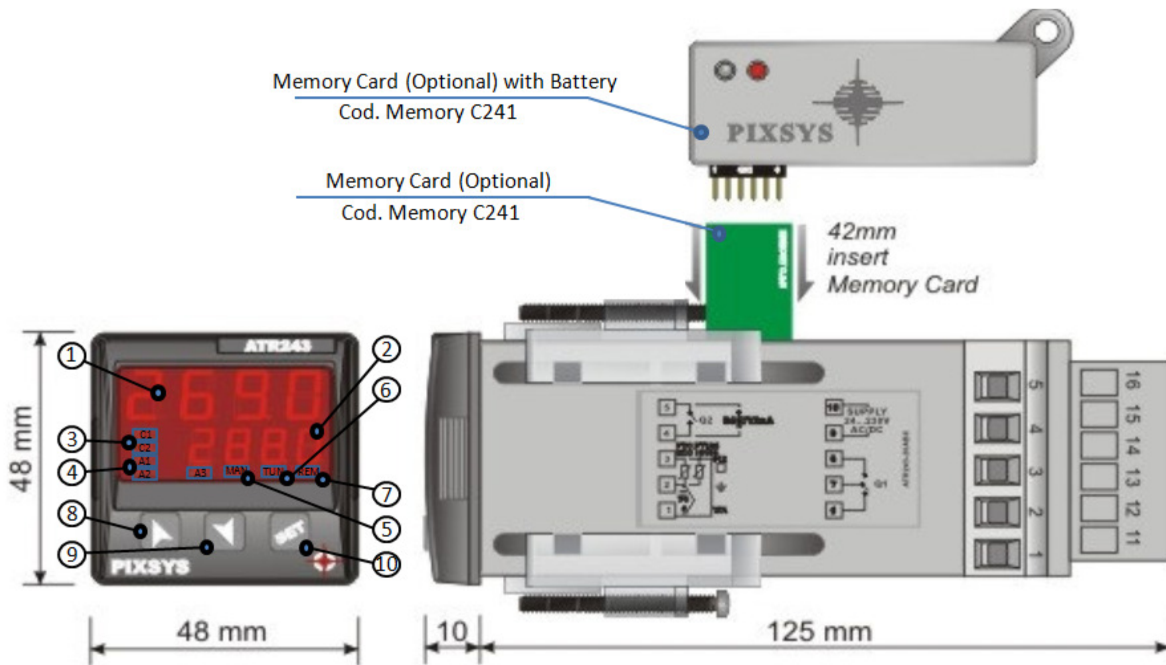

Figure B2: ATR 243 schematics.

ATR 243 provides the proportional with integral and derivative (PID) control that is consisted of a 150W resistive heater. This controller combines proportional control with two additional adjustments, which help the unit automatically compensate for changes in the system. These adjustments, integral and derivative, are expressed in time-based units. They are also referred to by their reciprocals, RESET and RATE, respectively. The proportional, integral and derivative terms must be individually adjusted or “tuned” to a particular system using trial and error. It provides the most accurate and stable control of the three controller types, and is best used in systems which have a relatively small mass, those which react quickly to changes in the energy added to the process. It is recommended in systems where the load changes often and the controller is expected to compensate automatically due to frequent changes in set-point, the amount of energy available, or the mass to be controlled.

The ATR 243 controller has a dimension of 48×48 mm and 2−4 set-point frontal extraction of electronics. It has an analog input that is configurable by parameter for up to 18 different sensors/signals. Besides, it consists of 2-4 outputs configurable as relays (also as Open/Close logic driven by motorized valves control, Solid Sate Relay (SSR), 4~20 mA, 0~10 V signal (both for command or re-scalable retransmission of process / set-point). The switching power supply has the capacity within the range of 24~230 Vac/Vdc that does not require any jumpers setting. As shown in Figure B2, 1~10 LED sections help user to signify the desired setting of temperature manually. LED section 1 shows the temperature of the process, LED section 2 shows the set-point signified by user.

This ATR also includes software features that include the launch tuning and the selection of 2-4 set-points by digital input. LED section 3 states the indication of the output command ON/OFF state. It becomes ON when the output command is on regarding relay /SSR /mA /Volt /motorized valve command. LED section 4 shows ‘ON’ if alarm keeps on during operation that is driven by manually inserted programme by user. LED section 5 remains ON when the manual function is ON. LED section 6 becomes on while running ‘Autotune’ cycle. LED section 7 becomes ON while communicating with the serial port. Optional Memory Card can also be used to this device to copy all parameters and those data can be further manipulated using software application LABSOFTVIEW on PC.

B3 Polarizer

In the experimental setup, Thorlab Inc. LPNIR100 linear polarizer has been used. This is a better alternative to a conventional polymer based polarizer due to the spherical ellipsoid nanoparticles embedded in sodium-silicate glass in the LPNIR100 which generate the polarizing effect. This polarizer is absorptive as it absorbs the light polarized perpendicular to the transmission axis.

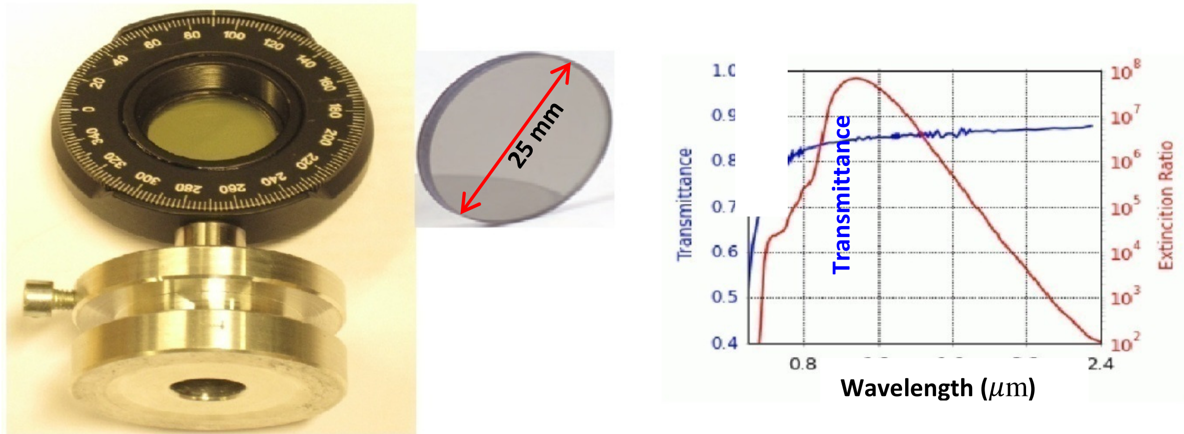

Extiction ratio

Figure B3: LPNIR100 linear polarizer.

The nanoparticles used in this component have a significantly higher damage threshold and a dramatically better extinction ratio. This is mounted with SM1 threading of diameter 25mm. Its linear polarizer selection is in the wavelength range from 650 nm to 2000nm. It maintains the extinction ratio of 1000:1 over the full operable bandwidth.

Appendix C

A Quick Guide to Intersubband (IS) Absorbance Study

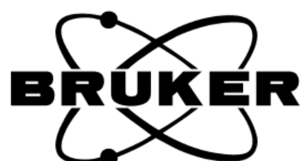

Contents

1. **Starting OPUS/IR .... iii**
2. **Measurement Settings ....vi**
3. **Printing Spectra .... xviii**
4. **Tips & Tricks ....xxi**

1. Staring OPUS/IR

The following steps have to be followed for measuring IS absorbance study:

1. Turn FTIR Spectroscopy ON.

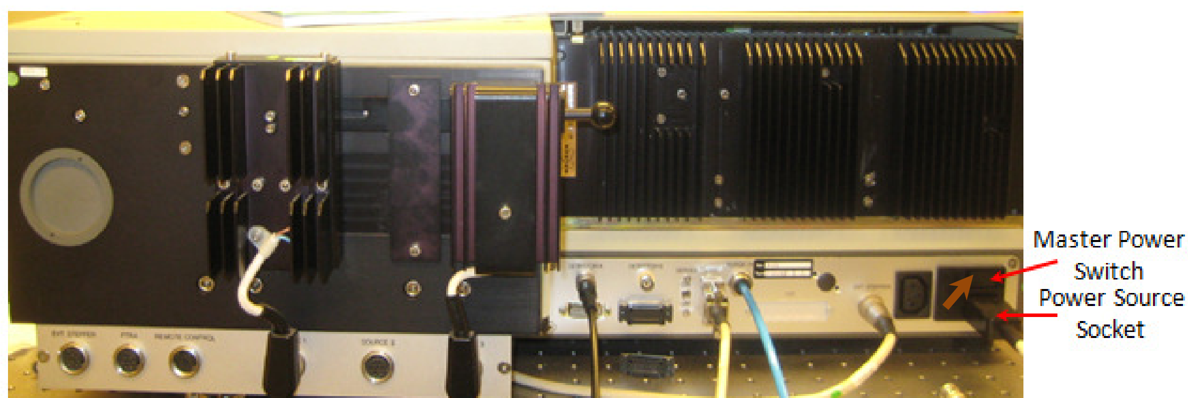

2. Put the Dummy sample at sample holder (located at experimental setup shown in section 4.6) in FTIR machine.
3. Turn the computer ON.
4. Click the *'OPUS 6.5'* icon on the desktop or from Windows XP *'START'* menu -> *'All Programs'*->*'OPUS 6.5'*.

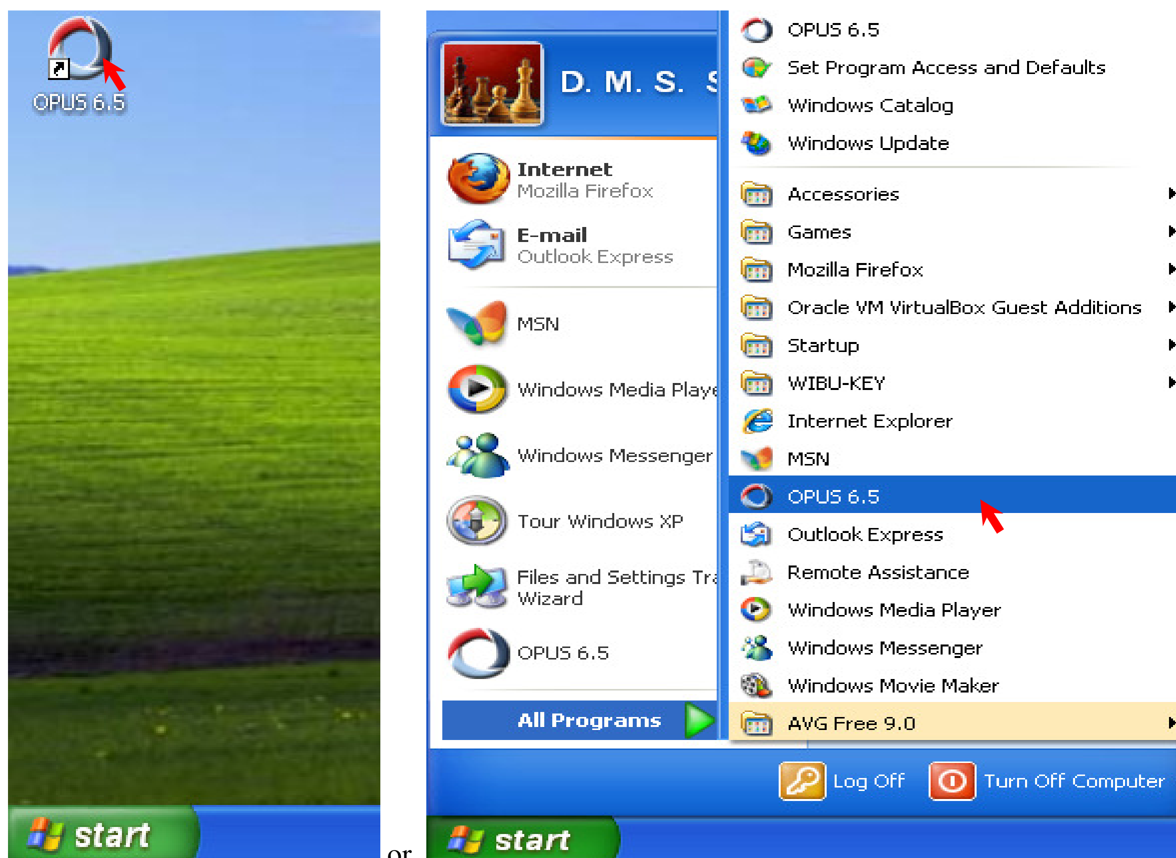

or,

5. Logging dialog will be open. Just press on the *'Login'* Button.

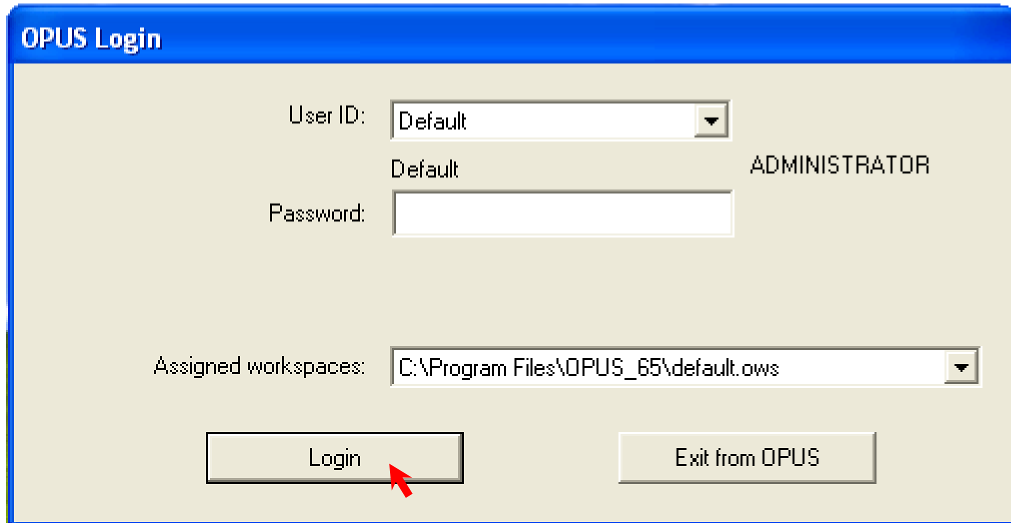

N.B.: *No password is needed to be entered. (However, in general case, User ID has to be selected (Default, Administrator, Labmanager, etc.) from the drop down list. Default logging password is* ***'OPUS'*** *[case sensitive] eventhough you may assign your own record later by choosing your own* ***'User ID'*** *and* ***'Password'***.

6. Now the front interface of *'OPUS'* along *'About OPUS'* will be open. Just click *'OK'*.

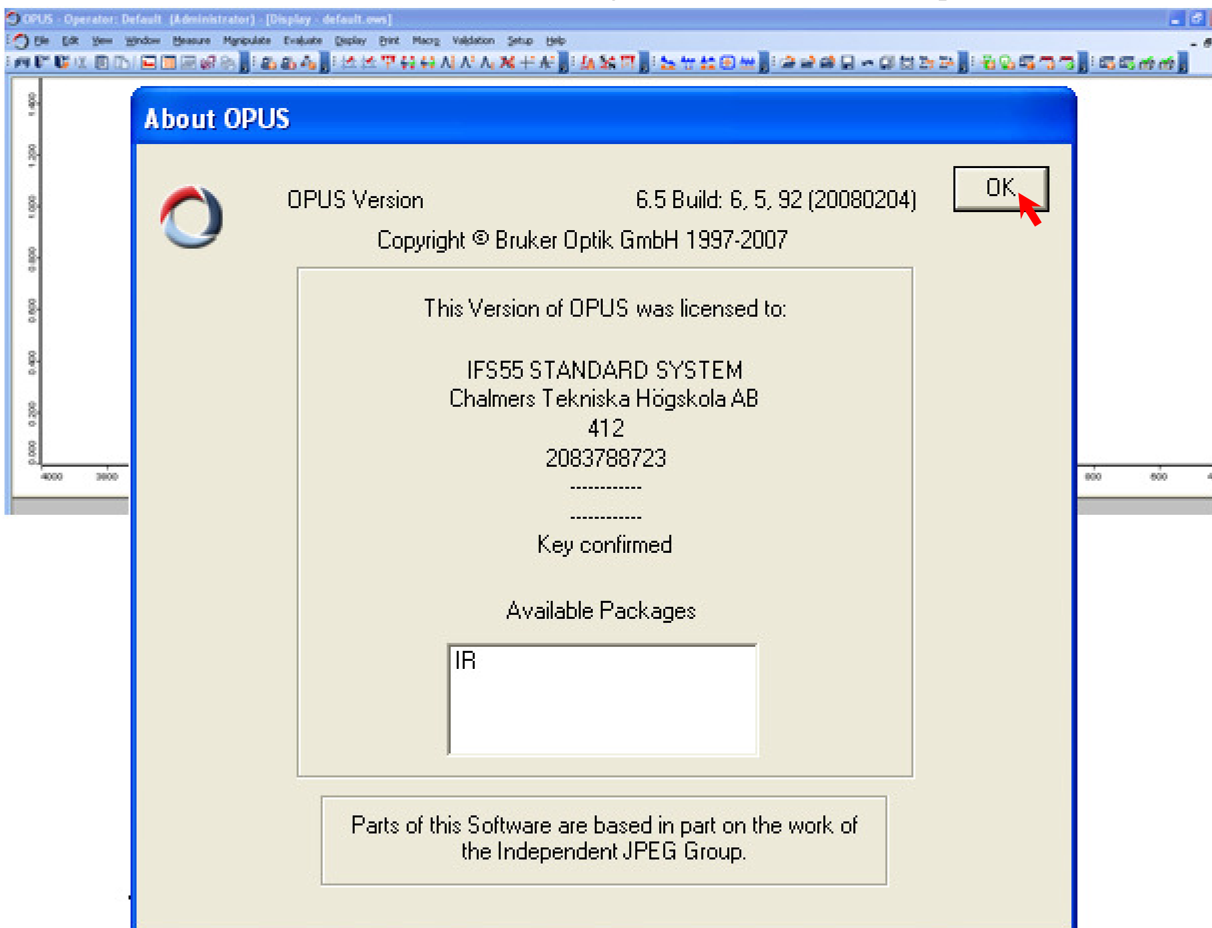

N.B.: ***'About OPUS'*** *window contains registration information of licensed User. The available packages [****'IR'*** *in installed version at PL lab] that are integrated along OPUS/IR software (registered form BRUKER Inc.) will be shown.*

7. Hereby, you will have the OPUS interface to play.

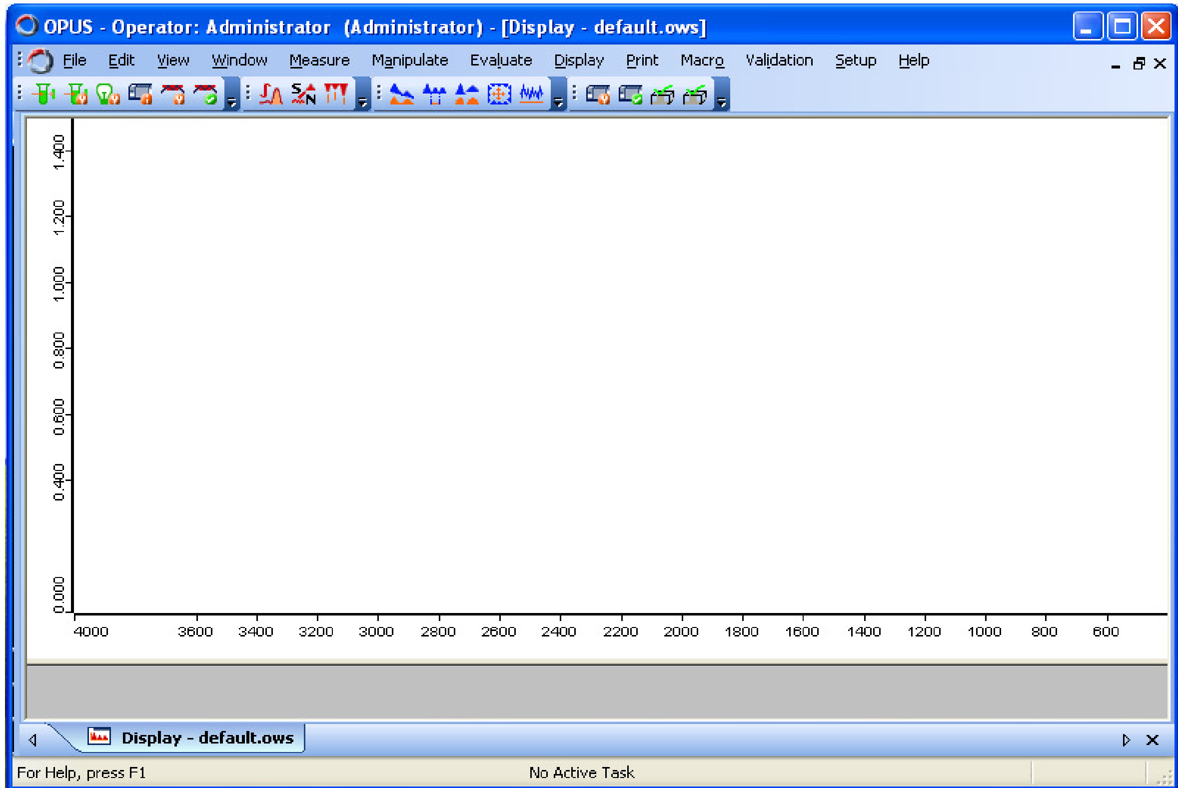

2. Measurement Settings

1. Click the *'Advance Measurement'* quick menu at top left corner at front interface.

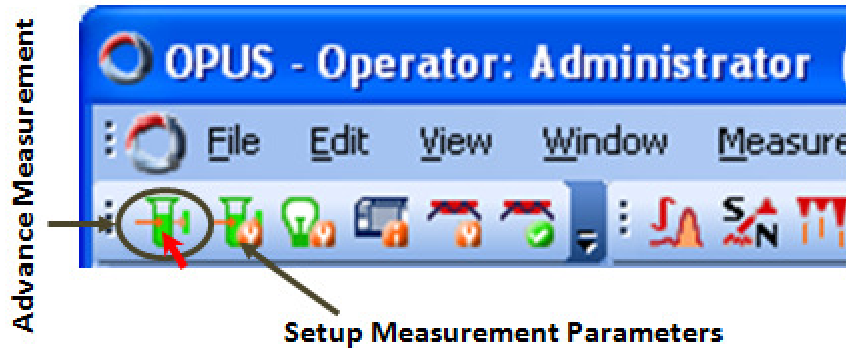

N.B.: *Don't be confused by clicking **'Setup Measurement Parameters'** quick menu since it looks pretty same as **'Advance Measurement'** quick menu but you won't find **'Background Signal Channel'** button or **'Sample Signal Channel'** Button in basic tab to measure reference signal or sample signal respectively. This **'Advance Measurement'** quick menu is not enlisted in **'Measurement'** menu as well. It has been added finding from **'View->Toggle Toolbars'**. See the section **Tips & Tricks** for further findings.*

2. Now, you will see the *'Measurement'* Window.

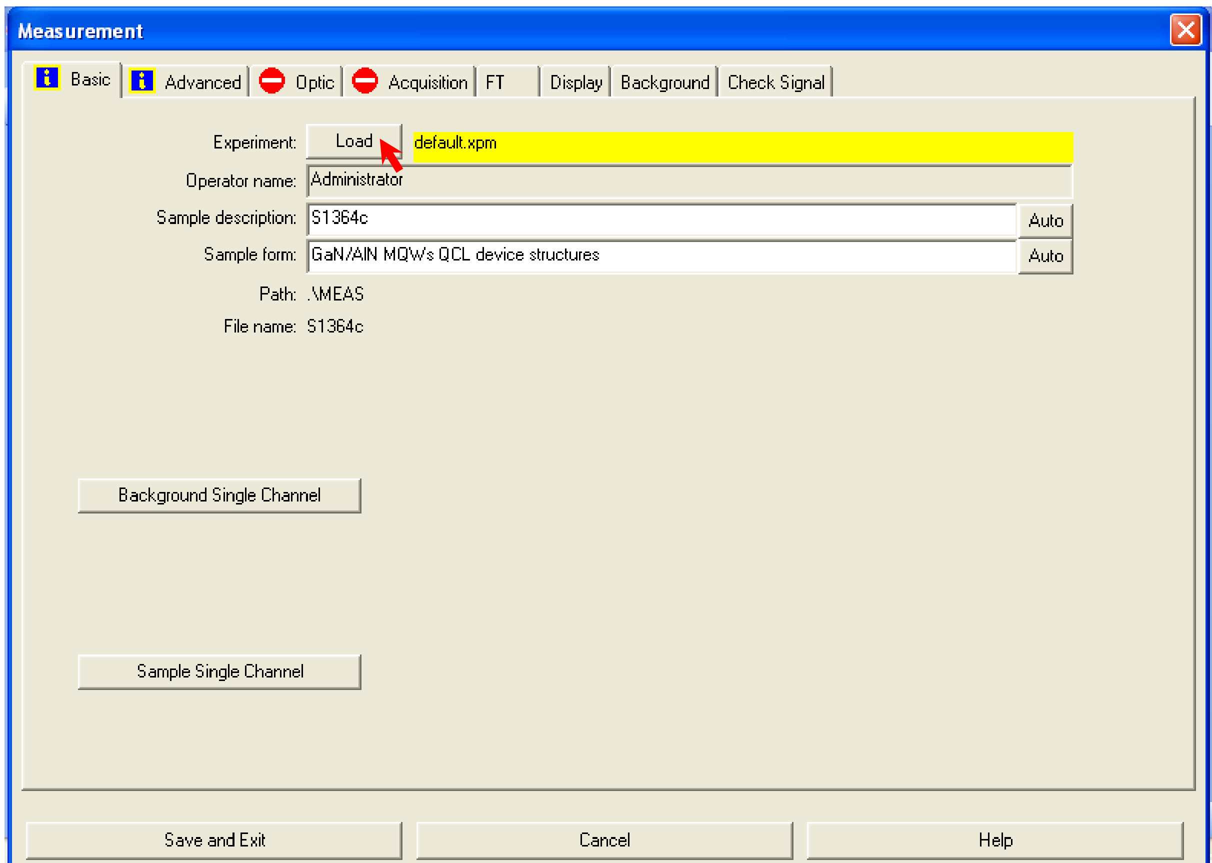

Here, first you may load the previously saved experiment settings clicking *'load'* button shown in *'Basic'* tab in *'Measurement'* window.

You may write your name in *'Operator name'* section. Otherwise, it will load operator name from previously saved settings as default.

You may define the sample description in '*'sample description'* section and may also add the sample property in *'Sample from'* section.

3. Now, go to '*Advance*' tab in '*Measurement*' window shown below.

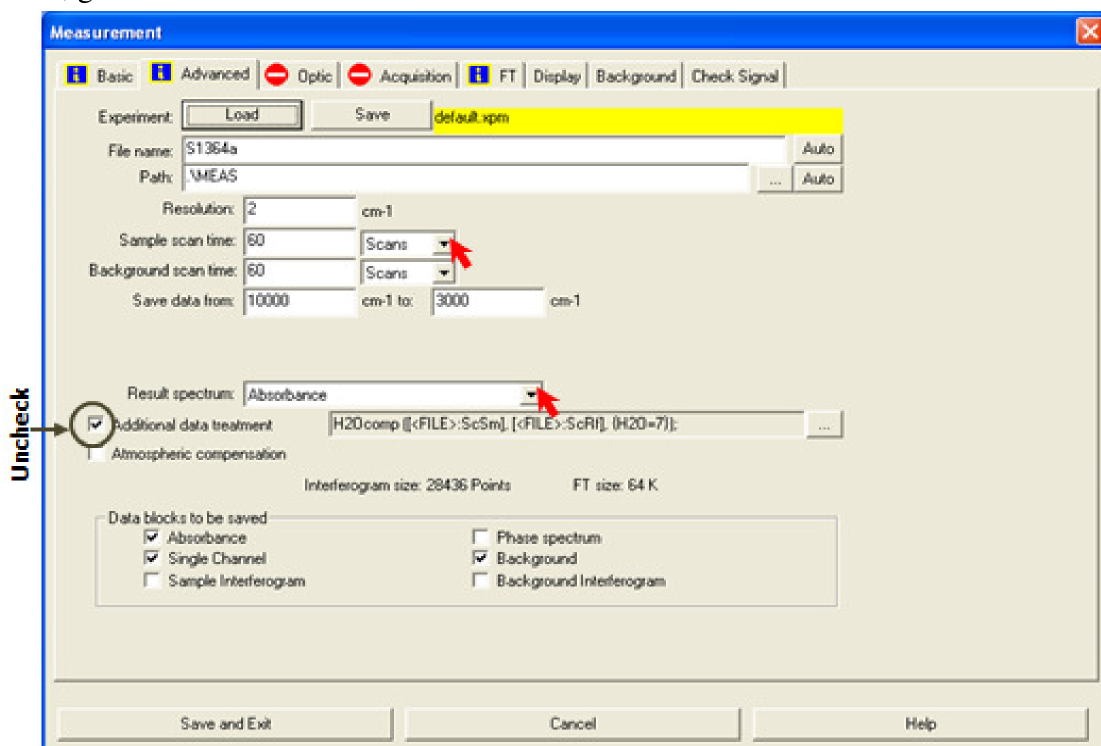

Again, you may load the previously saved experiment settings clicking *'load'* button shown in *'Advance'* tab in *'Measurement'* window if you have haven't load at *'Basic'* tab.

Add the settings name for remembrance at *'File name'* section.

You may define path for saving settings parameters in *'Path'* section in your PC.

Set the scanning resolution *'2'* at *'Resolution'* section.
N.B.: *Maximum resolution, 0.2 cm^{-1} can be possible to assign. If your signal strong enough, it is recommended to use low resolution like [2 / 4] for making the computation faster.*

Set the number of sample scan and reference scan in *'Sample scan time'* and *'Background scan time'* section. Choose unit *'Scans'*.
N.B.: *Two things have to be remembered here. Firstly, you have to choose either **'Scans'** or **'Minutes'** as unit for both reference and sample signal. Secondly, minimum value of **'Scans'***

*or **'Minutes'** for reference signal can be equal to sample signal's **'Scans'** or **'Minutes'** value though it can be larger. However, if you choose lower **'Scans'** or **'Minutes'** value, it will calculate the IS absorbance spectra with lower SNR.*

Assign the wavelength range in which wavelength range you want save the optically characterized signal (that passes through your sample and be detected at detector) at *'Save data from'* section.
N.B.: *To save valid data range, make sure the wavelength range is in between assigned range at **'Acquisition'*** tab.

Assign your type of optical characterization in section *'Result Spectrum Section'*. Here, *'Absorbance'* have to be selected as you are interested to measure IS absorbance.

Leave uncheck the *'Additional data treatment'*.
N.B.: *You may add script if you have already designed one to specifically refrain from the effect of environment absorbance [H_2O, CO_2 etc. reside in air].*

You may check or uncheck *'Atmospheric Compensation'* section since N_2 is being purged in FTIR spectroscopy machine to get rid of additional absorbance from H_2O, CO_2 etc. molecules reside in air.

You may save *'Absorbance', 'Phase spectrum', 'Background', 'Signal channel', 'Background interferogram'* and *'Signal interferogram'* while calculation is being performed by OPUS at by assigning tick mark at *'Data block to be saved'* section.

4. Now, go to *'Optic'* tab in *'Measurement'* window to select the FTIR instrument's component required for your observation.

   Select the '*NIR source'* from '*Source settings'* list section.
   N.B.: *There are other source choices like **'MIR source'** for mid infrared region spectroscopy and **'Emission'** for photoluminescence study (actually it let you know FTIR spectroscopy machine about an external source).*

   Select the '*CaF_2'* from '*Beam splitter'* list section as this is mounted in IFS55.

   Select the Aperture size of NIR source beam from '*Aperture settings'* list section.
   N.B.: *The maximum aperture size could be 10 mm and minimum could 0.3 mm. Higher aperture size is recommended for thermal (DLAGTS) detector while lower (i.e. 1.85 mm to 0.3 mm) is recommended for Quantum detector (i.e. Si/Ge detector). High intensity flux may saturate the detectivity of the detector and it is the option to play with this issue.*

   Choose *'front'* from '*Measurement channel'* list section.

   Choose *'front'* from '*Background meas. Channel'* list section.

Select *'External A'* from *'Detector settings'* list option as external detector is installed for IS absorbance measurement in External Port A in FTIR Spectroscopy rear side.

Select optical scanning velocity from *'Scanner velocity'* list option as an external detector is installed for IS absorbance measurement in External Port A (in FTIR Spectroscopy's rear side).
N.B.: *Lower value combination of both resolution (cm^{-1}) and scanner velocity (KHz) will help to create spectra with higher SNR but definitely with the cost of time.*

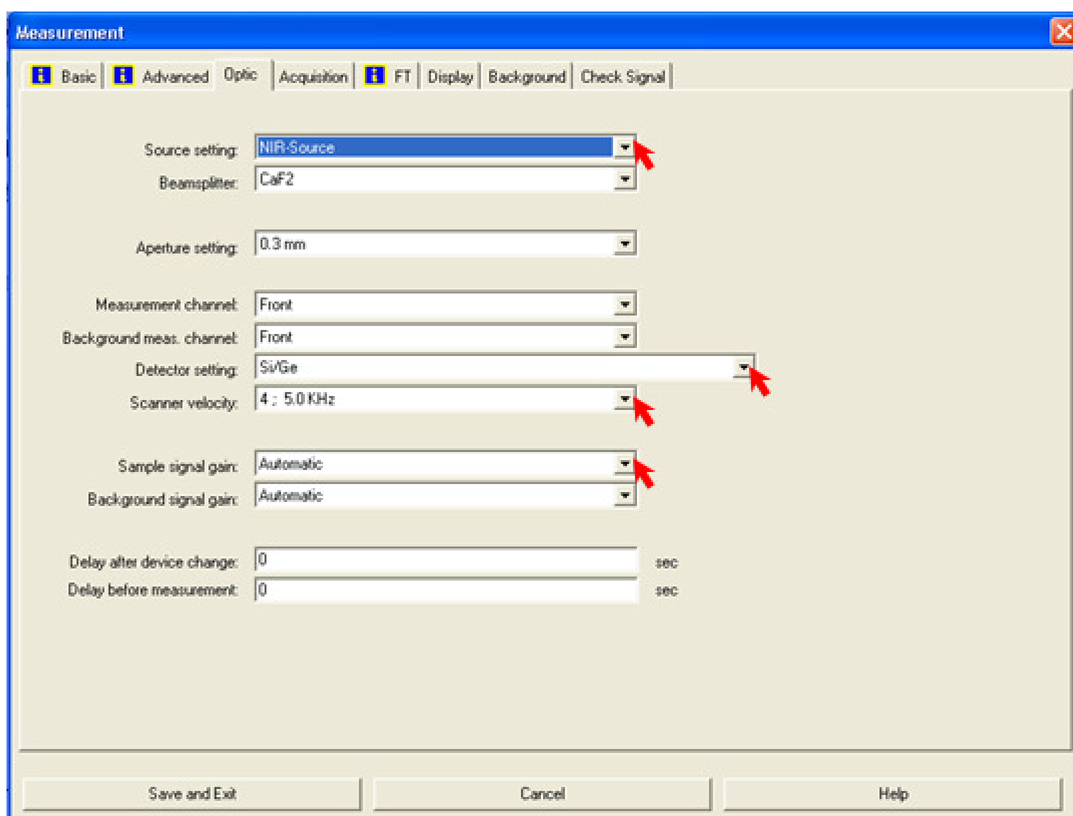

Change *'Automatic'* to *'1'* or *'2'* from *'Sample signal gain'* list option as external detector is installed.

Keep unchanged *'Automatic'* from *'Background signal gain'* list option.

'Delay after device measurement' and *'Delay before measurement'* sections should set '*0*' sec.

5. Now proceed to *'Acquisition'* tab of *'Measurement'* window. This is an important setting window where you actually assign the instructions for FTIR's operation as well as limit of operation.

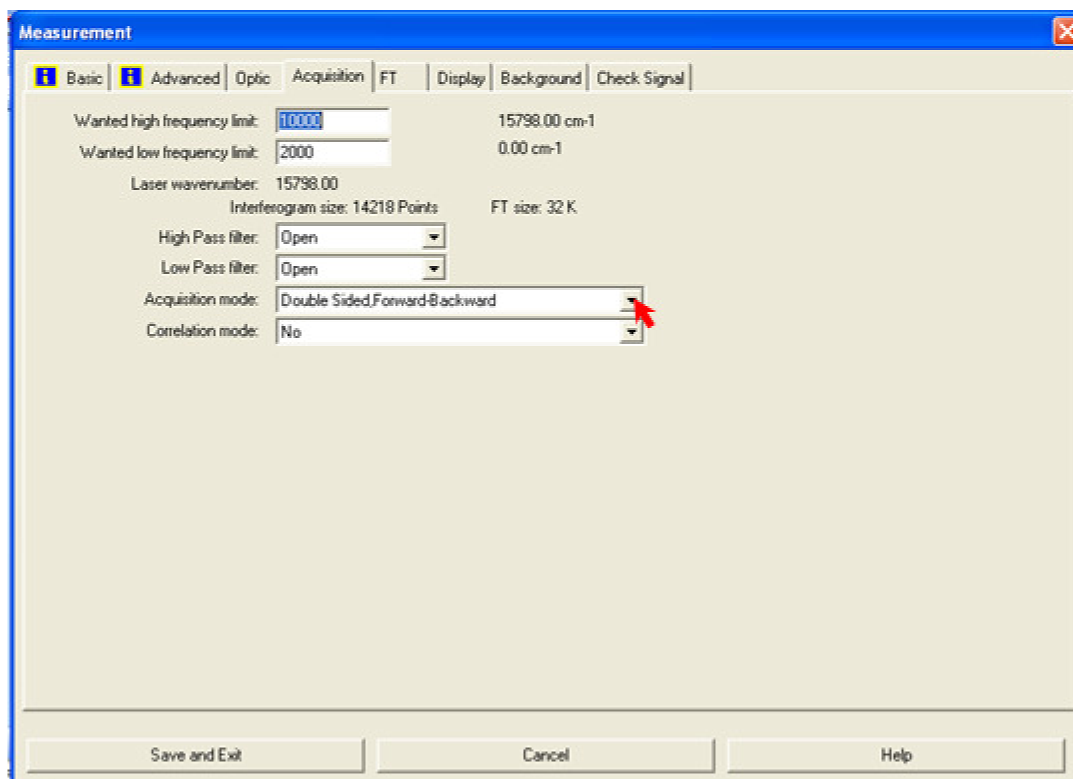

Set the high and low frequency limit at *'Wanted high frequency limit'* and *'Low frequency limit'* sections respectively that have shown above.

N.B.: *This is the actual frequency limit where data will be calculated. The bandwidth limit help to reduce the amount of data recorded from high resolution spectra. Due to this bandwidth assignment, FTIR itself (ADC block) uses filters (electrical / optical) to ensure the signal intensity '0' beyond the selected frequency limit (otherwise the unwanted signal beyond bandwidth limit may convoluted/folded to selected range and may taint the intensity).*

Make sure the *'laser wavenumber'* section displays 15798 cm^{-1} since HeNe laser emits at this frequency (633 nm). So, if it is been changed, FTIR will not be able to make interferogram or sampling the signal anymore. To fix this problem, see the *'tips & tricks'* section.

You may select *'Open'* for *'Low Pass filter'* and *'High Pass filter'* list section at *'Acquisition'* tab since there were no real external is electronic filter installed in FTIR spectroscopy.

Select *'Double Sided, Backward-Forward'* at *'Acquisition mode'* list option.
N.B.: *This option reduce dead time, improves signal-to-noise ratio. For more information, you look upon OPUS Reference Manual (pp.: 102)* [32].

You may select *'No'* at *'Correction mode'* list section to make sure data integrity.

N.B.: *It's quite useful to weak signal. For more details please look on the OPUS Reference Manual (pp. 102) for various correlation methods available in* ***'Correction mode'*** *list section* [32].

6. Go to *'FT'* tab at *'Measurement'* window. This tab is used basically to define treatments for Fourier transform calculation.

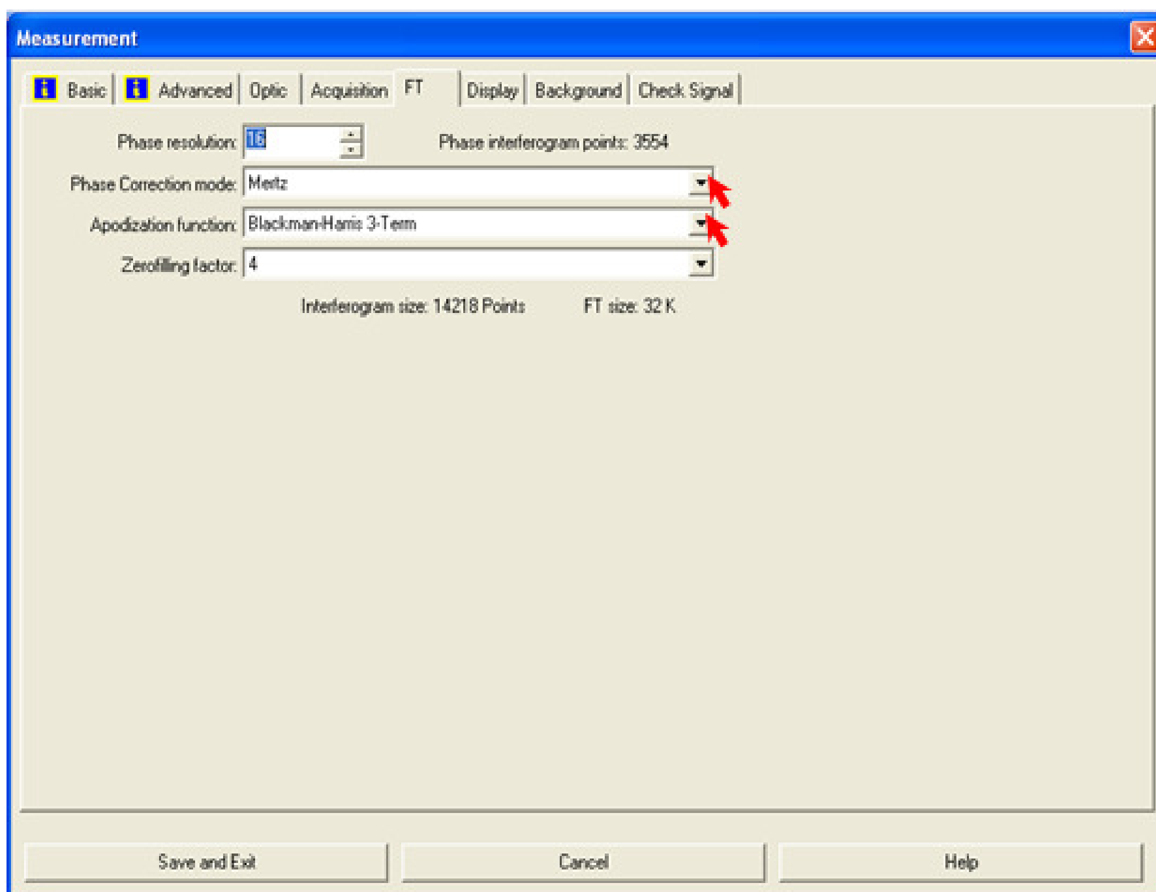

Set *'16'* to *'Phase resolution'* section (recommended for the bandwidth of our interest).

N.B.: *Define this phase resolution* (cm^{-1}) *in such way that the number of phase interferogram points amounts to at least 250 (in defined acquisition bandwidth).*

Set *'Mertz'* to *'Phase correction mode'* section.

N.B.: *For more information on other modes please look upon OPUS Reference Manual (pp. 163-168).*

Set *'Blackman-Harris 3-term'* to *'Apodization function'* section.

N.B.: *For more information on other methods of apodization, please look upon OPUS Reference Manual (pp. 163-168).*

Set *'4'* to *'Zerofilling factor'* section.

N.B.: *This helps to get sharper peak though you may assign larger value to get better spectrum. Unfortunately, here is a tradeoff since it increases the computation time.*

7. Go to *'Display'* tab at *'Measurement'* window. This tab is used basically to assign the axes settings for the spectrum display during measurement.

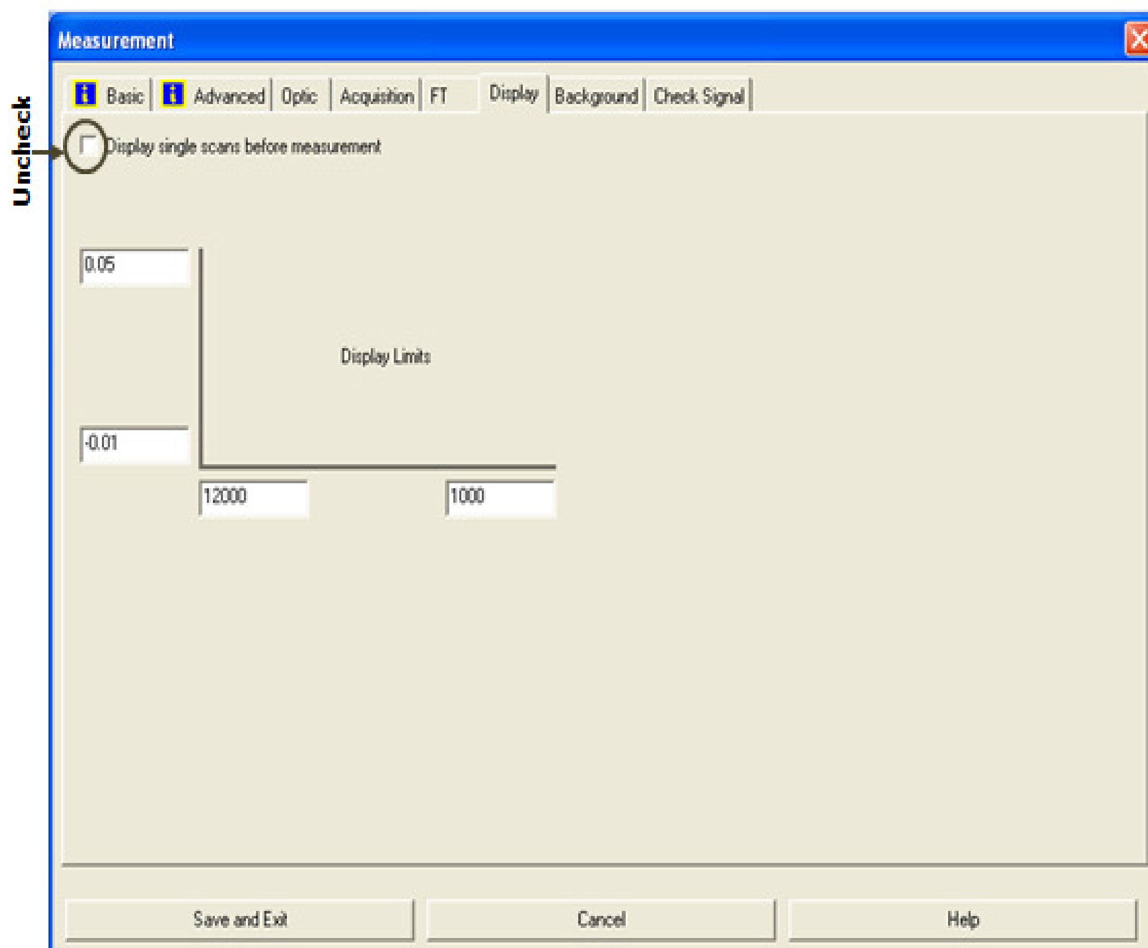

Uncheck *'Display single scans before measurement'*
N.B.: *As it will display the spectrum from the first scan before whole number of scans are completed and you may misguided to see the spectrum with SNR perhaps.*

Assign your bandwidth (on which range, you would like to see) along X-axes and arbitrary absorbance limit at Y-axes.

8. Go to *'Check signal'* tab at *'Measurement'* window. This window is very useful since it helps to see the instantaneous strength (from acquisition processor, AQP) of interferogram as well as signal spectrum. If amplitude strength is more than 29 (Shown below), then it means that the scale of signal strength is so low that detector cannot essence any signal there. (And, there will be no spectrum in the window). Recheck the experimental setup, check the interferogram again. Continuous this process unless you see the amplitude value is more than 29.

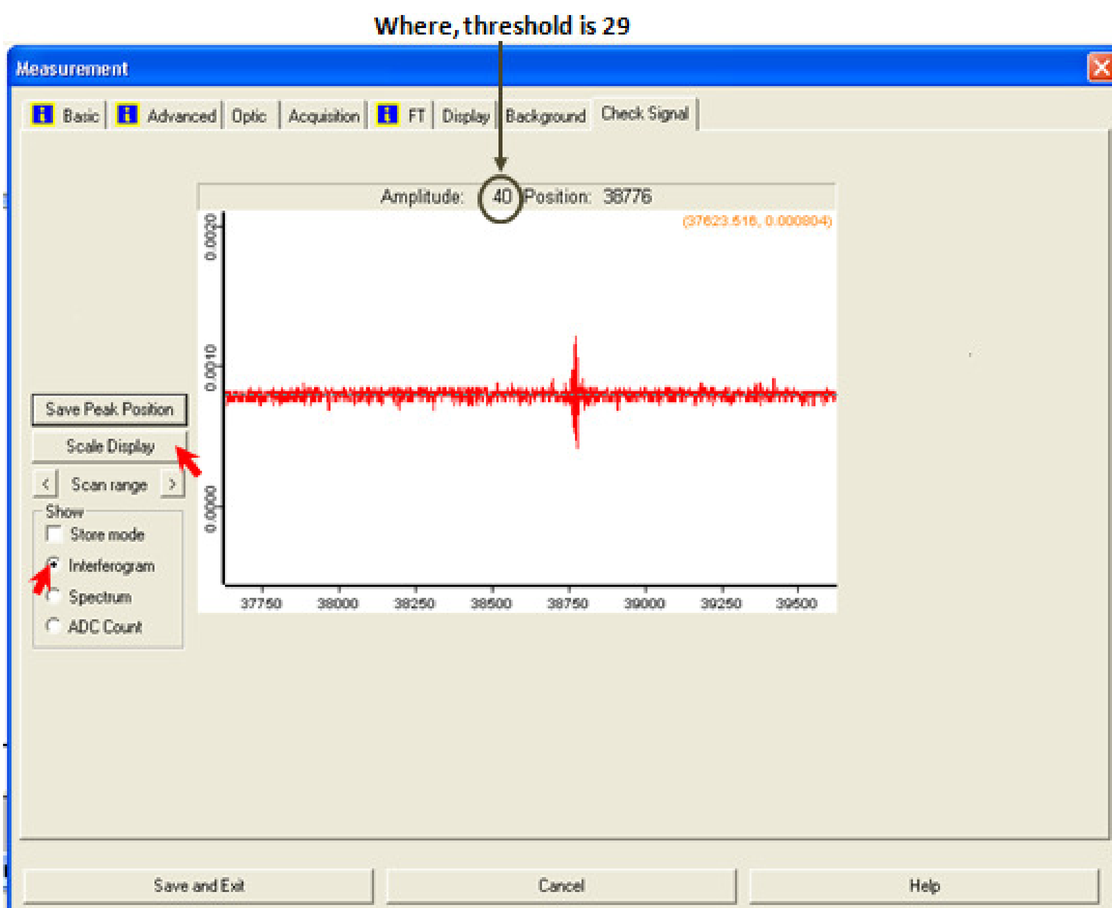

7

Select the '*interferogram*' to see check interferogram. It may see (Shown below) straight line even if amplitude value crosses the threshold value (~ 30-100).

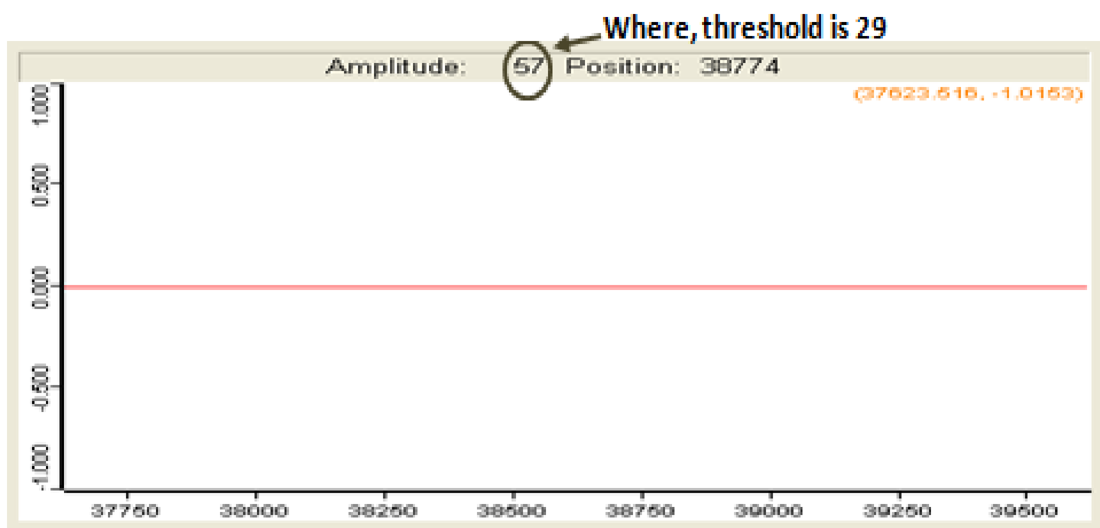

To solve the problem, click the '*Scale display'* button. It will fit the interferogram in accordance to the total area at spectrum window.

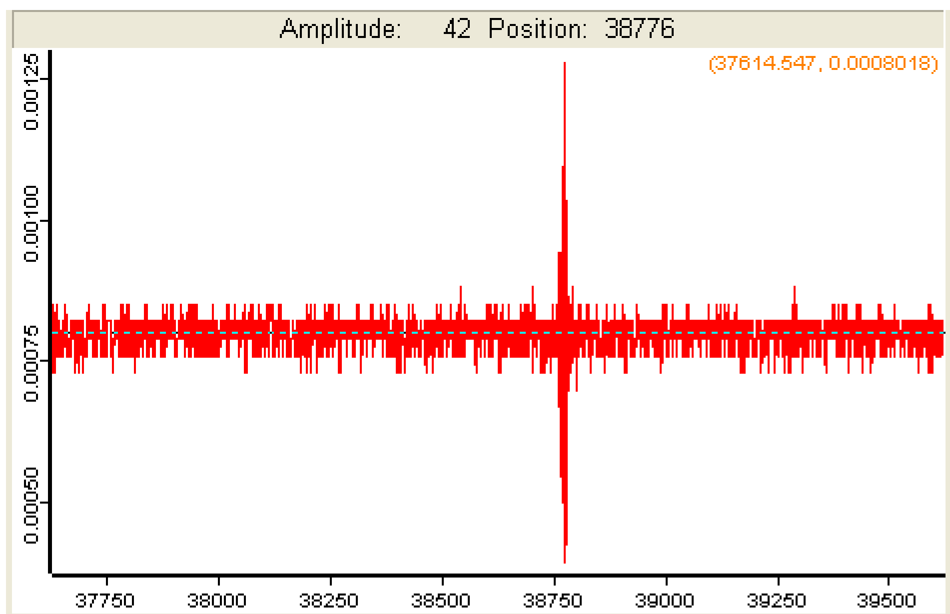

Click the *'Spectrum'* to see the signal spectrum.

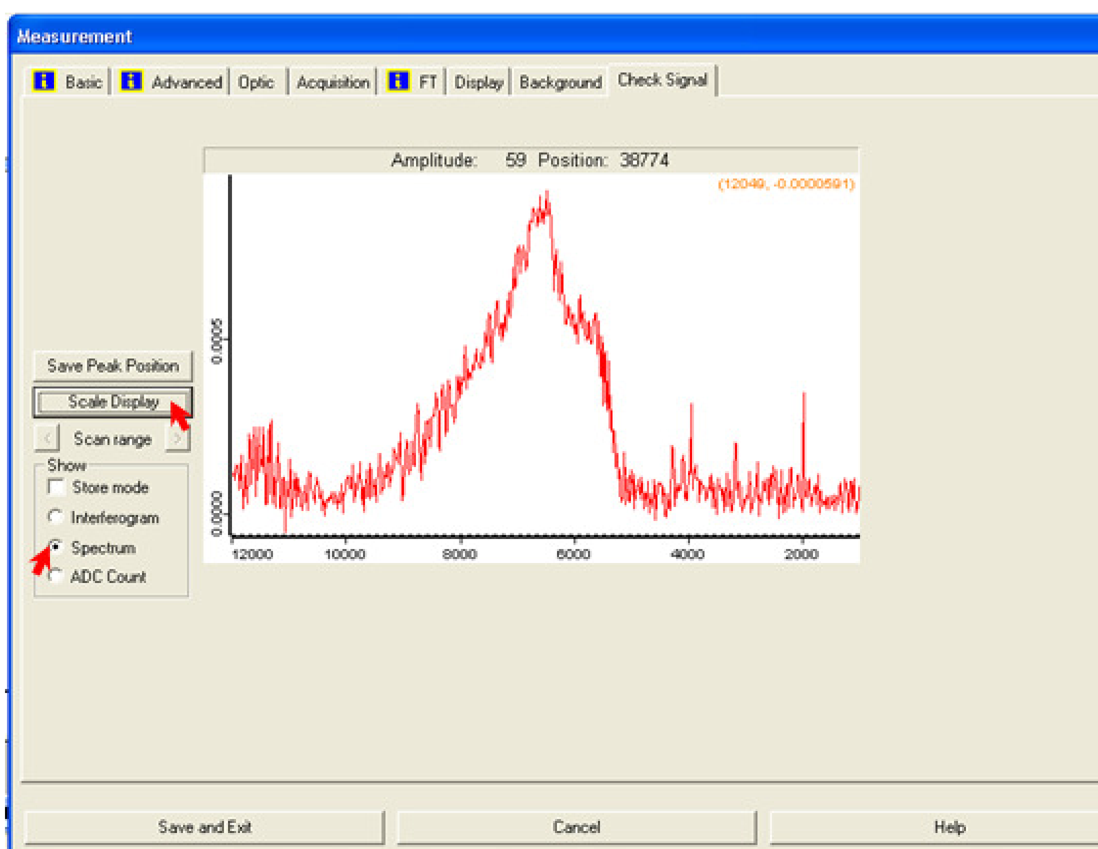

Here. It may also show nothing if the signal strength is so low (~ 30-100). To solve the problem, just click '*Scale display'* button.

9. If you have seen the interferogram as well as spectra, it means that you ready to measure spectra. Go to the *'Basic'* tab in *'Measurement'* window again and click *'Background signal channel'* at *'Basic'* tab.

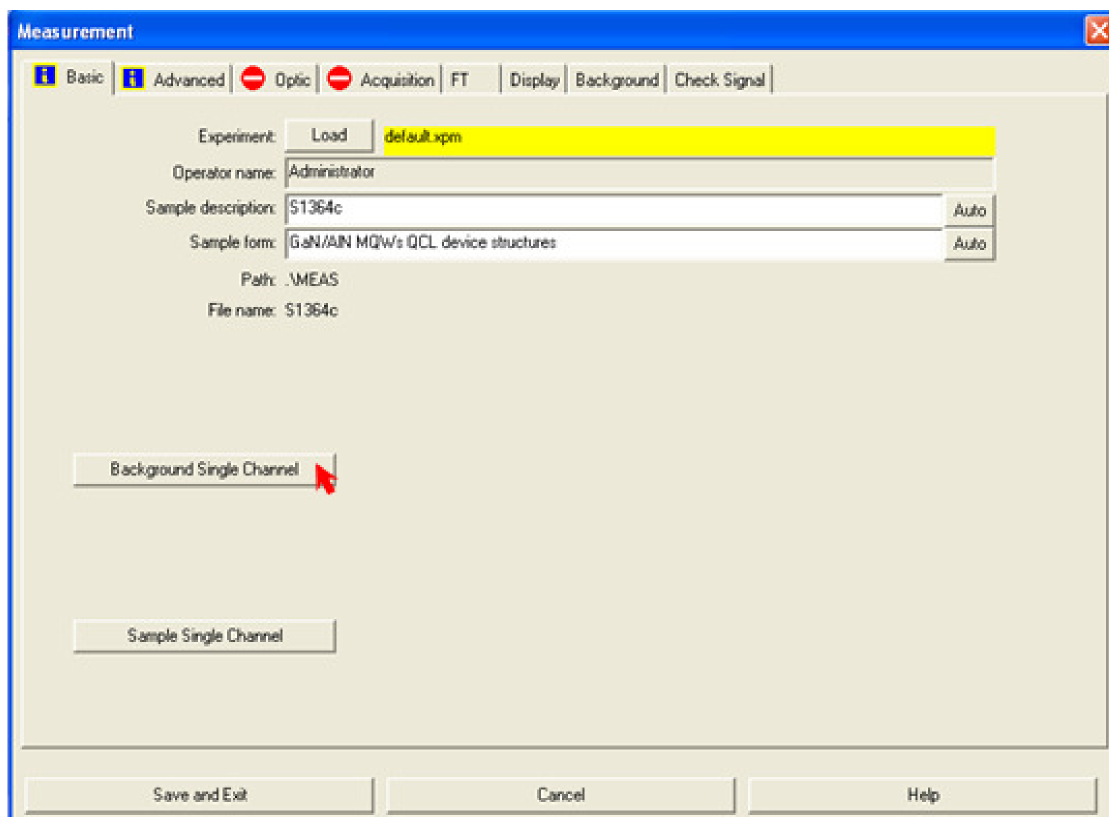

Once measurement is done you save the background signal by going to *'Background'* tab in *'Measurement'* window. Click *'Save Background'* Button.

N.B.: *Background generally stays at Acquisition processor (AQP) of FTIR. In save process, it transfers from AQP to PC.*

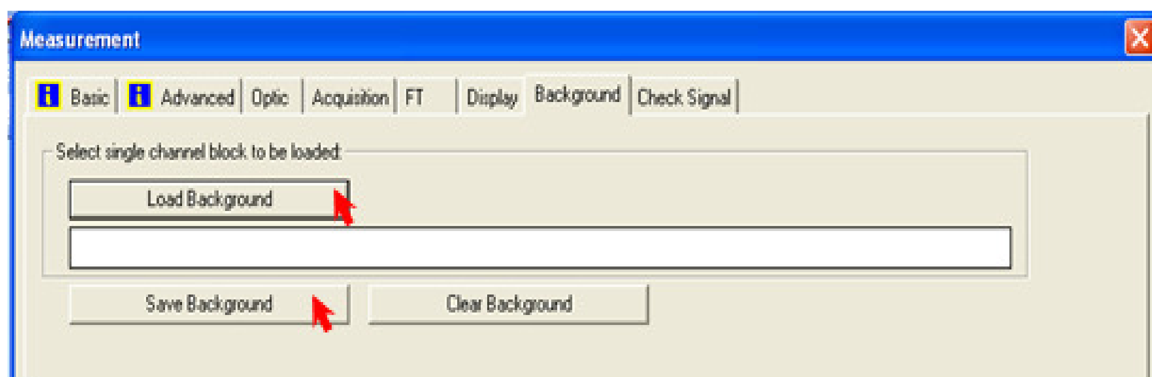

You may also load background signal for specific location on PC by clicking *'Load Background'* Button. *'Clear Background'* Button is used to clear loaded background signal on PC.

10. Now mount the real sample instead of dummy one at sample holder in FTIR experimental setup (See: section 4.6).

11. Go to *'Check signal'* tab at *'Measurement'* window again to check if the interferogram and signal can be seen.

12. If manage to see interferogram and signal there, go to *'Basic'* tab in *'Measurement'* window. Click *'Sample signal channel'* at *'Basic'* tab.

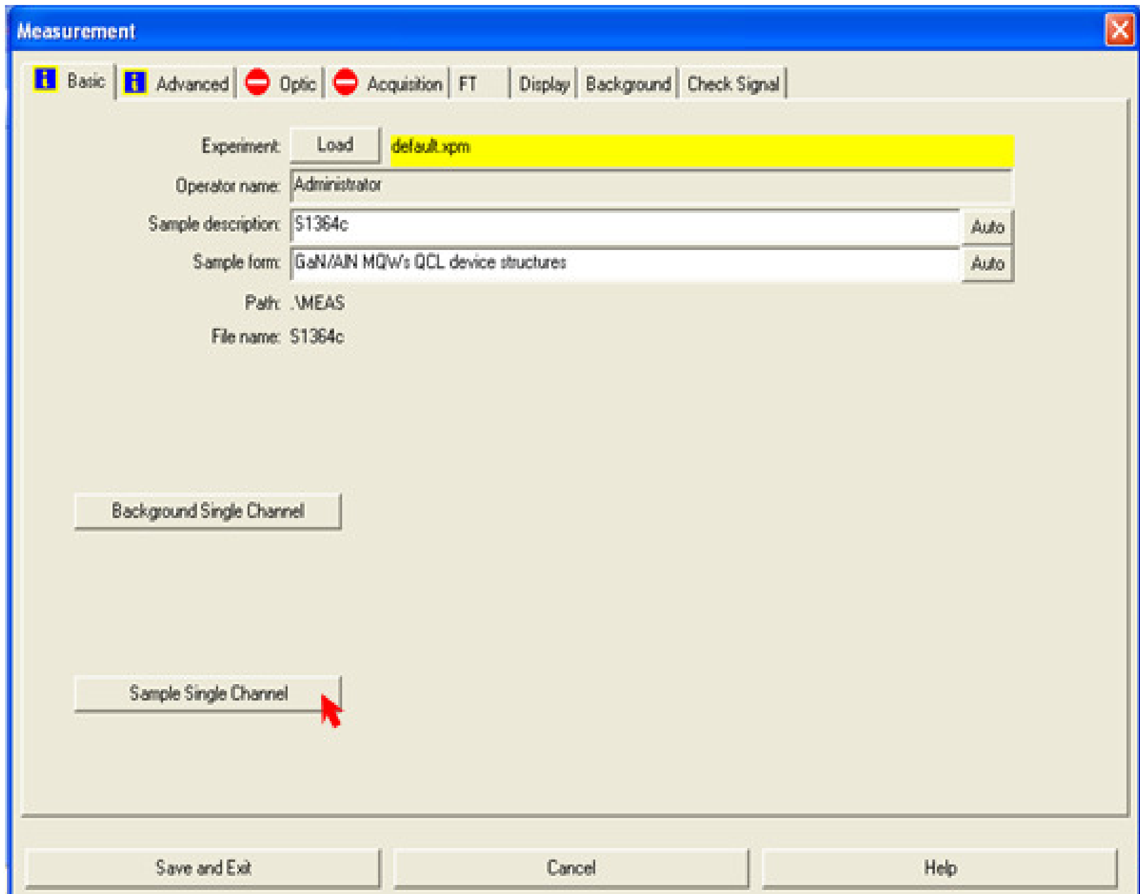

Now, you are done with measurement step. After completing the scan and calculation, you will see IS absorbance spectra in spectrum window (at front interface of OPUS/IR).

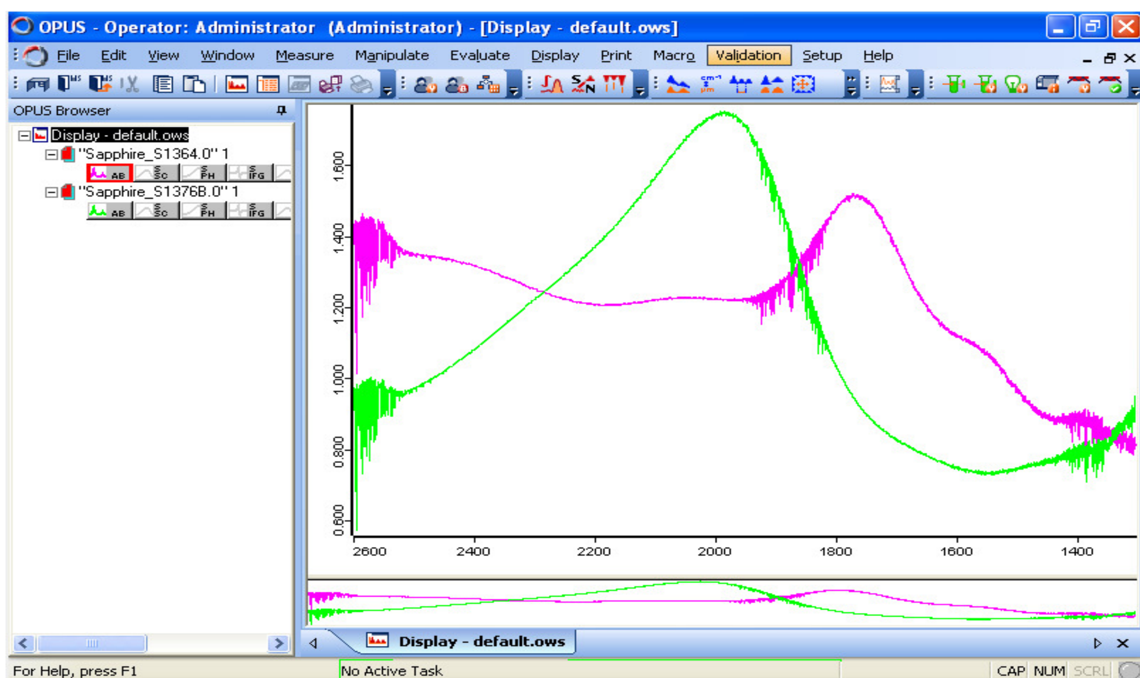

3. Printing Spectra

1. To print the spectra, select the spectra that you would like to print and open the print spectra window by clicking *'Print->Print Spectra'*.

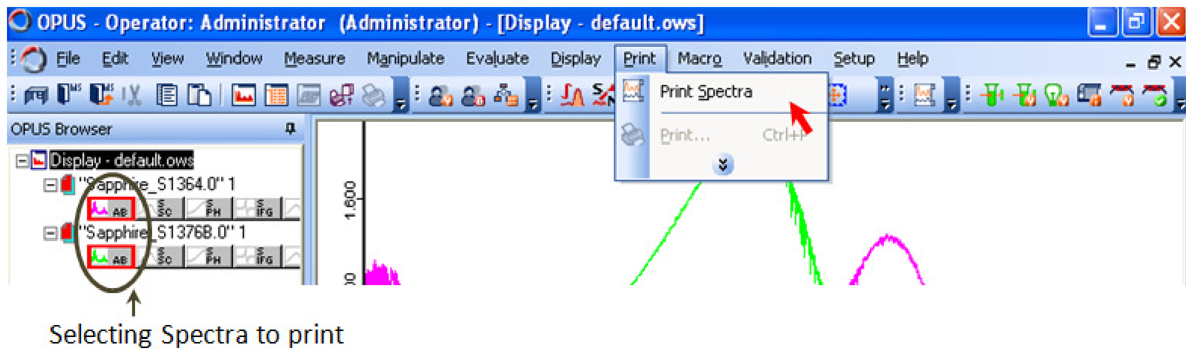

Selecting Spectra to print

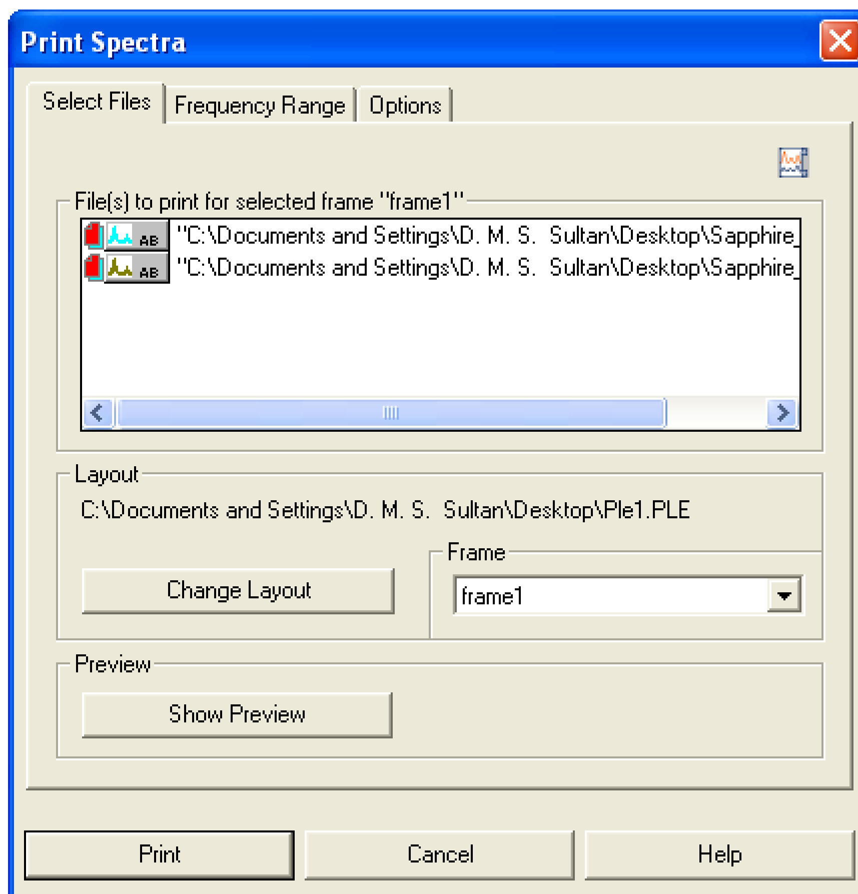

You may check the printing range by clicking *'Show Preview'* button shown above.

2. You may also define the intended frequency range from *'Frequency Range'* tab from *'Print Spectra'* window.

   Select *'Set limit separately for each spectrum frame'* at *'Frequency Range'* tab. Define X axes (at *'X-Startpoint',' X-endpoint'* sections) and Y axes (at *'Y-Minimum', 'Y-maximum'* sections) as printing dimension limit.

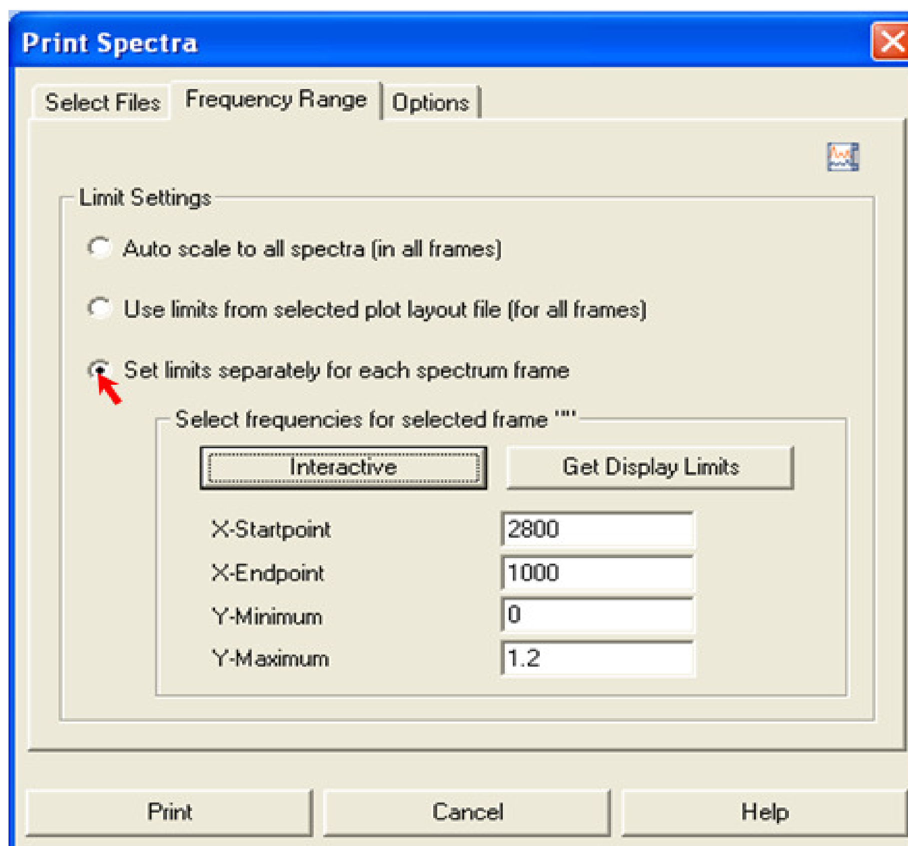

3. Go to *'Option'* tab at *'Print Spectra'* window.

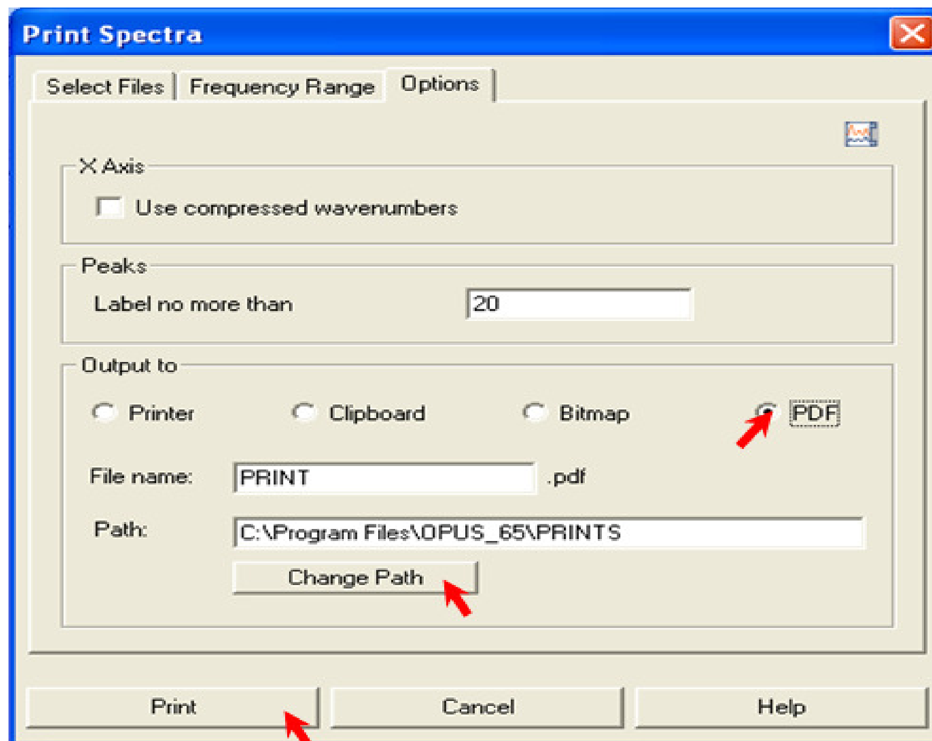

Select the output type (*'PDF', 'Bitmap', 'Clipboard'* or *'Printer'*) from *'Output to'* Section.

Set the location printed file clicking *'Change path'* button.

Click *'Print'* button now. The figure should be printed by now (i.e. below).

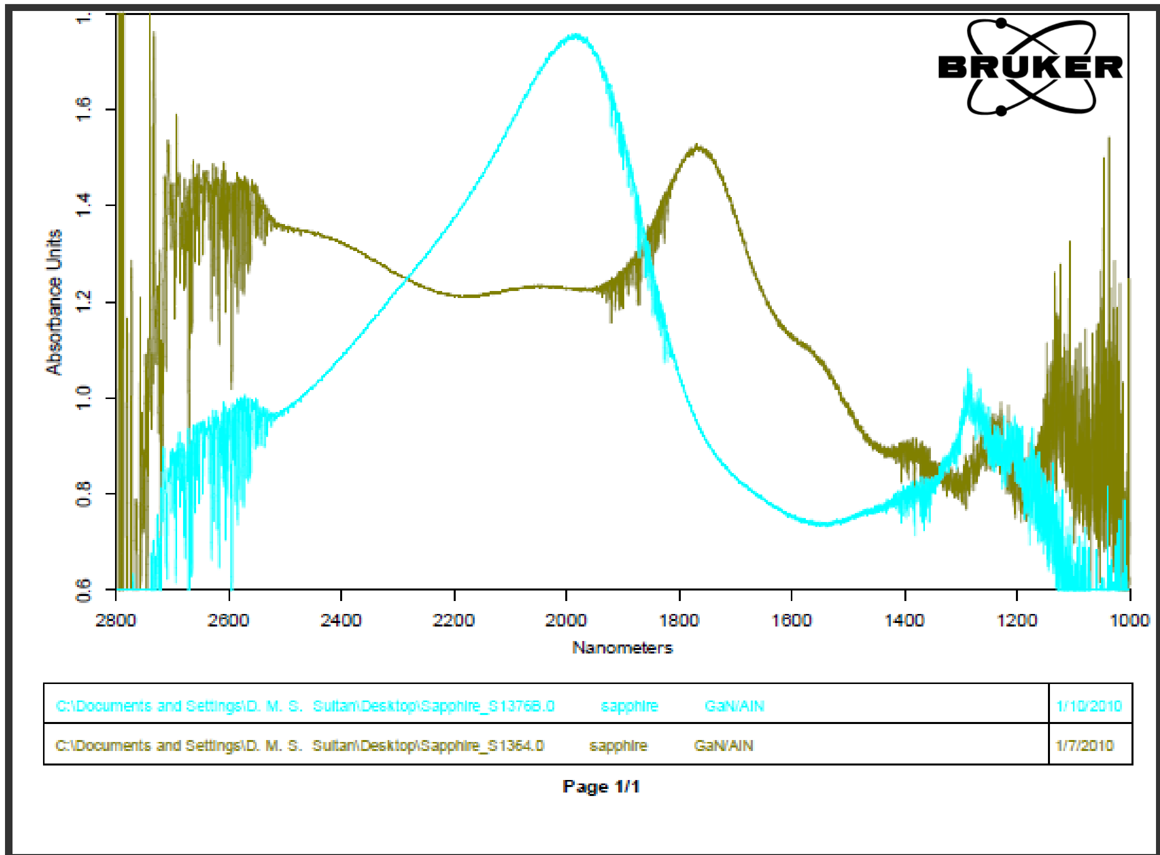

4. Tips & Tricks

1. **Adding *'Advance measurement'* Button:**
   To add the *'Advance measurement'* button to front interface, click *'View->Toggle Toolbar'* from menu-bar. A *'Customize'* window will be open then.

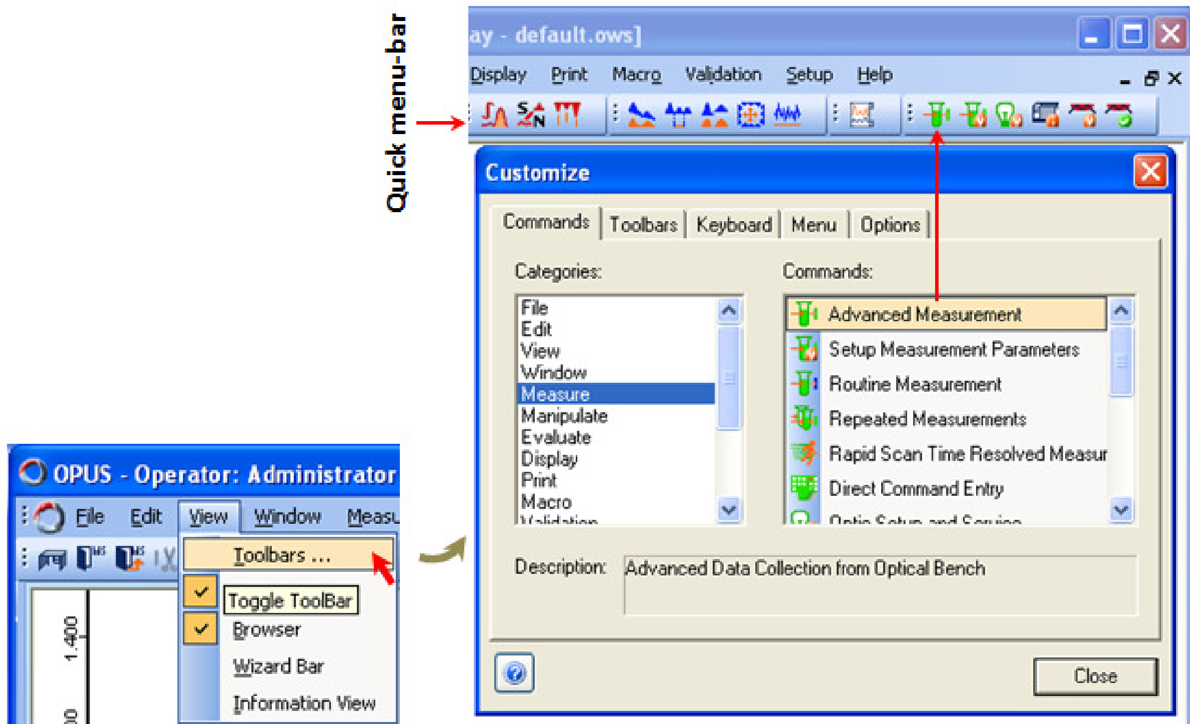

   Go to *'Commands'* tab at *'Customize'* window. Select *'Measure'* at *'Categories'* section. You will see all commands relevant to measure technique will be available to *'Commands'* section at *'Commands'* tab.

   Select *'Advance measurement'* from *'Commands'* section at *'Commands'* tab and drag & drop to *'Quick'* menu-bar of front interface at OPUS/IR.

2. **Fixing HeNe laser wavenumber:**
   Click *'Measure->Optic Setup and Service'* from menu-bar of front interface of OPUS/IR.

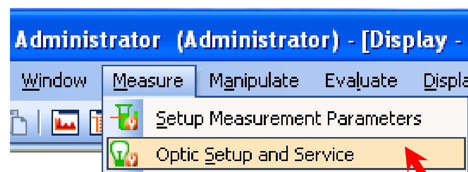

   Now, *'Optic Setup and Service'* window will be open.

   Select *'Interferometer/AQP'* tab from *'Optic Setup and Service'* window.

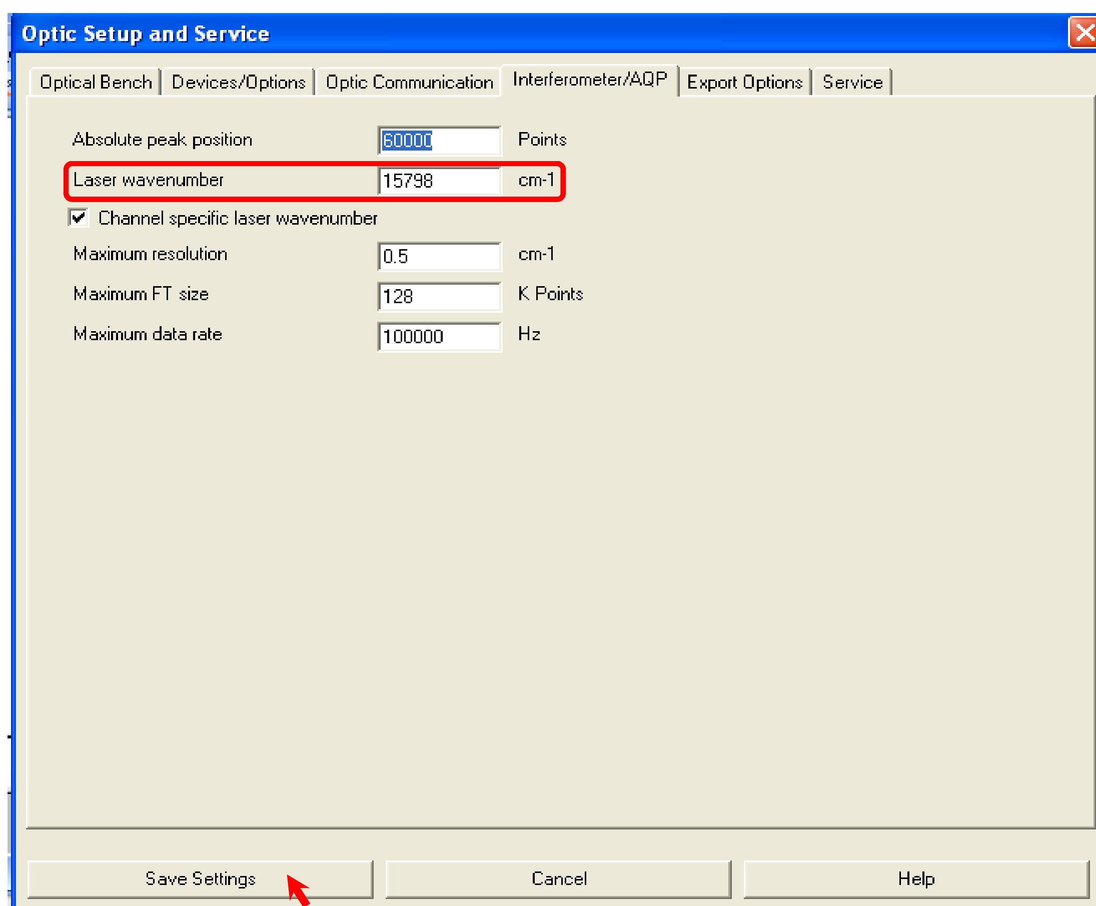

Assign the 15798 cm^{-1} (HeNe laser wavenumber) at '*Laser wavenumber*' section at '*Interferometer/AQP'* tab.

Click *'Save Settings'* button. Restart FTIR Spectroscopy and PC.

3. **Export measured data:**
   To manipulate the measured data with software (i.e. MATLAB), you may export data. Select the data file you want to export. Then, click *'File->Save File As'*. *'Save File As'* window will be open.

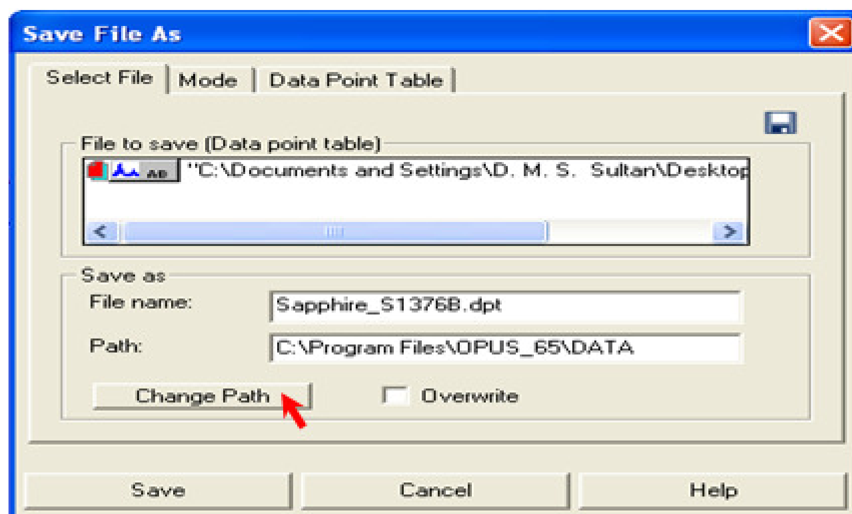

Assign the file name at *'File Name'* section at *'Select File'* Tab.

Change the path where you want to save file clicking *'Change Path'* button at *'Select File'* tab.

Go to *'Mode'* tab at *'Save File As'* window.

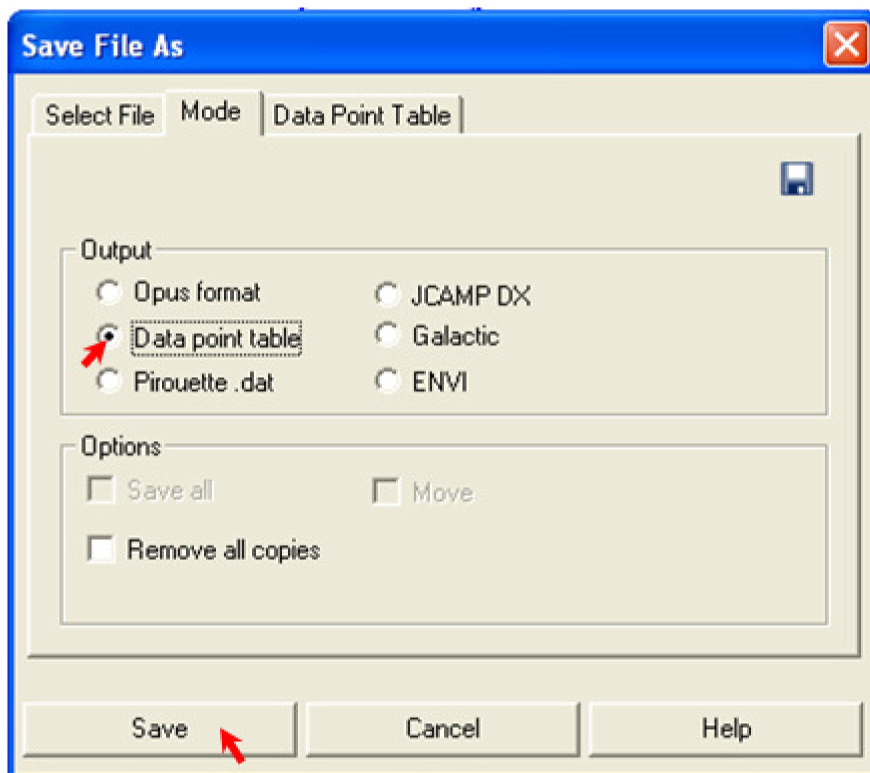

Select *'Data point table'* at *'Output'* section in *'Mode'* tab.

Click *'Save'* button. Now, all data should be saved as *'.dpt'* format in your predefined location at PC.

References

[1] Asano, T; Tamura, M; Yoshizawa, S; Noda, S, "Pump-probe measurement of ultrafast all-optical modulation based on intersubband transition in n-doped quantum wells", APPLIED PHYSICS LETTERS, 77(1): 19-21, 2000-07-03.

[2] Claire Gmachl, Hock M. Ng, S.-N. George Chu, and Alfred Y. Cho, "Intersubband absorption at $\lambda \sim 1.55 \mu$m in well- and modulation-doped GaN/AlGaN multiple quantum wells with superlattice barrier", Appl. Phys. Lett. 77, 3722 (2000).

[3] K. krishno, A. Kikuchi, H. kanazawa, and T. Tachibana, Phys. Stat. Sol. (a) 192 124 (2002)

[4] A. Helman, M. Tchernyceva, A. Lusson, E. Wrade, F. H. Julien, K, Moumanis, G. Frishman, E. monroy, B. daubin, D. Dang, E. Bellet-amalric, and D. Jalabert, Applied Physics Letter, 83 5196 (2003)

[5] W. G. Perry, M. B. bremser, T. Zheleva, R. F. Davis, W. Shan and J. J. Song, Journal of Electronic Material 26 224 (1997).

[6] Joachim peprirk, " Nitride Semiconductor Devices: Principle and Simulation", Page:4, ISBN: 978-3-527-40667-8

[7] Scipy:Open source Scientific Tools for Python: The Scipy.linalg routine eigbanded, 2001.

[8] A. Castaddini, A. Cavallini and L. prolenta, Applied Physics letter 84, 4851(2004)

[9] H. Teisseyre, P. perlin, T. Suski, J. Applied Physics, 76, 2429(1994)

[10] D. C. Raynolds, J. Hoelscher, C. W. Litton, and T. C. Collins, J. Applied Physics, 92, 5596(2002)

[11] K. B. Nam, J. li, J. Y. Lin, and H, X, Jiang, Applied Physics Letter. 85, 3489 (2004)

[12] N. E Christensen and I gorczyca, Physics rev. B 50, 4397 (1994)

[13] F. bschstedt, U. Grossner, and J. Furthmuller, Phys. Rev. B 62 8003 (2003)

[14] A. M. Sanchez, F. J. Pacheco, S. I. Molina, J. Stemmer, J. Aderhold and J. Graul, "Critical thickness of high-temperature AlN interlayers in GaN on sapphire (0001)", Journal of Electronic Materials, Volume 30, Number 5, pages: L17-L20, May, 2001.

[15] P. Hacke, A. Maekawa, N. Koido, K. Hiramatsu and N. Sawaki, Jap. J. Applied Phys. 33 6443 (1994)

[16] A. E. Wickenden, L. B. Rowland, K. Doverspike, D. K. Gaskill, J. A. Freitas, D. S. Simons and P. H. Chi, J. Electron. Mater. 24 1547 (1995)

[17] A. Cremades, L. Gorgens, O. Ambacher, M. Stutzmann, and F. Scholz, Phys. Rev. B 61 2812 (2000)

[18] L. T. Romano, C. G. Van de walle, Ager, J. W. W. Gotz and R. S. Kern, J. Appl. Phys. 87 7745 (2000)

[19] J. Faist, F. Capasso, D. L. Sivco, C. Sirtori, A. L. Hutchinson, and A. Y. Cho, Science 264 553 (1994)

[20] Xinyu Liu, "GaN/AlN multiple quantum well structures: MBE Growth and characterization", Doctoral Thesis, ISBN: 978-91-7291-3, page: 9, 2007.

[21] F. Berbardini and V. Fiorentini, Appl. Phys. Lett. 80, 4145 (2002).

[22] A. Zoroddu, P. Ruggerone, F. Berbardini and V. Fiorentini, Phys. Rev. B 64, 45208 (2001).

[23] A. Ishida, Y. Inoue, M. Kuwabara, H. Kan and H. Fujiyasu, Japan J. Appl. Phys.., vol. 41, pp. 1303-1305 (2002).

[24] S. Chuang, Physics of Optoelectronics Device, New York: Wiley InterScience, 1995.

[25] M. O. Manasreh, Semiconductor quantum wells and superlattices for long wavelength infrared detector. Boston: Artech House, 1993.

[26] T. Aggerstam, T. G. Andersson, P. Holmstrom, P. Jänes, X. Y. Liu, S. Lourdudoss and L. Thylen, " GaN/AlN multiple quantum well structures for 1.55 μm intersubband absorption", Proc. Of SPIES, vol. 6479 64791E-8.

[27] X. Y. Liu, P. Holmstöm, P. Janes, L, Thylen, and T. G. Andersson,, Phys. Stat. sol. (b) 244, No. 8, 2902-2903, 2007

[28] X. Y. Liu, P. Holmstöm, P. Janes, L, Thylen, and T. G. Andersson,, Phys. Stat. sol. (b) 244, No. 8, 2895, 2007

[29] Kristian Berland, Martin Stattin, Rashid Farivar, D. M. S. Sultan, Per Hyldgaard, Anders Larsson, Shu Min Wang, and Thorvald Andersson, Phys. Appl. Lett. (accepted).

[30] D. C. Larrabee et al., App. Phys. Lett. 83, 3936 (2003).

[31] T. Y. Lin, Y. M. Sheu, Y. F. chen, J. Y. Lin, H. X. Jiang, "Optical properties of GaN/AlN multiple quantum wells", Solid State Communication 131, pp. 391, 2004

[32] BRUKER Optics, "Application and Measurement Software Reference Manual", OPUS Spectroscopy Software ver. 6, 2006.

[33] Kent B. Hill, Scott A. Basinger, Ronald A. Stack, and David J. Brady, "Noise and information in interferometric cross correlators", APPLIED OPTICS, Vol. 36, No. 17, 10th June, 1997.

PAPER

Temperature stability of intersubband transitions in AlN/GaN quantum wells

Kristian Berland, Martin Stattin, Rashid Farivar, D. M. S. Sultan,

Per Hyldgaard, Anders Larsson, Shu Min Wang, and Thorvald Andersson

[1] *Department of Microtechnology and Nanoscience, MC2,*

Chalmers University of Technology, SE-41296 Göteborg, Sweden

Abstract

Temperature dependence of intersubband transitions in MBE-grown AlN/GaN multiple quantum wells is investigated both by absorption studies at different temperatures and modeling of conduction-band electrons. For the absorption study, the sample is heated in increments up to 400^0C. The self-consistent Schrödinger-Poisson modeling includes temperature effects of the bandgap and the influence of thermal expansion on the piezoelectric field. We find that the intersubband absorption energy decreases only by ~ 6 meV at 400^0C relative to its room temperature value.

Intersubband transitions in nitride-based semiconductor heterostructures hold great promise for optoelectronic devices. The high band-offset between gallium nitride (GaN) and aluminum nitride (AlN) enables intersubband transitions in the near-infrared regime (λ = 1-4 μm). Thus, intersubband devices such as modulators, detectors, and quantum cascade lasers (QCLs) have the potential to operate at wavelengths useful for fiberoptic communication. QCLs also have the potential to be used when measuring characteristic absorption of small molecules. There are several studies of intersubband absorption in AlN/GaN heterostructures.[1-6] These typically show a peak at 500 to 900 meV with full width half maximum (FWHM) in the range of 60 to 200 meV. An intersubband device should operate at and above 300 K, often with the condition of a negligible change in transition energy. Temperature dependence of the transition energy, up to room temperature, has been reported for *intersubband* absorption in InAs/AlSb multiple quantum well (MQW) structures[7] and for *interband* photoluminescence in nitride-based AlN/GaN MQW structures.[8] The huge piezoelectric fields introduce an additional temperature-dependent effect in the nitride MQW structures, because the different thermal expansions of AlN and GaN induce a temperature dependent strain in the structures.

In this letter, we demonstrate that the peak position of intersubband transitions red shifts only ~ 6 meV as the temperature of the sample is increased from 25^0C to 400^0C. This aspect of thermal robustness could be vital for the operation of nitride-based QCLs since their ultrafast LO-scattering rates and high intersubband energy would cause them to heat significantly. The temperature effects are studied for MQW structures both experimentally by measuring the absorption at different temperatures, and theoretically by a self-consistent solution to the Schrödinger-Poisson equations for the conduction-band electrons. The nitride-semiconductor heterostructures are characterized by huge internal electric fields, which arise from the exceptionally large spontaneous and piezoelectric fields. A proper account of these fields is crucial for an accurate description and characterization of the quantum well states, and they require that the complete structure is considered in the design of heterostructures.

The set of MQW structures (A, B, C) are grown in a Varian Gen II modular molecular beam epitaxy (MBE) system. Elemental gallium and aluminum are evaporated from thermal effusion cells, and nitrogen from a plasma source. For substrates, we use metalorganic vapour phase epitaxy (MOVPE) grown silicon-doped GaN templates on 2" sapphire substrates. The GaN epitaxial layer is 2.5 μm thick. All substrate holders are temperature-calibrated to control the substrate surface temperature within approximately $\pm 5^0$C. The GaN buffer layer is silicon doped. We grow crack-free MQW structures on top of this buffer layer at a substrate temperature of 760^0C and thereafter cap the structure with a 500 nm silicon doped GaN layer grown under the same conditions as the buffer layer.[9,10]

For the absorption study, the MQW structures are cut into 5×7 mm large chips and polished into a standard multi-pass geometry with 45^0 beveled input and exit edges. The temperature is set within $\pm 5^0$C using a resistive heater and measured with a PT100 probe. The transmitted light is focused onto a TE-cooled InGaAs detector (1.2-2.75 μm, ThorLabs PDA10DT). The absorption in the MQW structures is measured using a Bruker IFS 55 FTIR Spectrometer. A (ThorLabs LPNIR100) linear (0.65-2 μm, 30 dB ER) polarizer is used to select transverse-magnetic (TM) polarized light. We measure the transmission at room temperature and in 50^0C increments between 50^0 and 400^0C. Two measurement runs are made: one where the temperature is increased between each increment and one where it is decreased. For background reference at each temperature, a sapphire dummy sample is used.

The intersubband absorption energies and conduction band profile are calculated using the Schrödinger-Poisson equation for envelope-functions within the effective-mass approximation:[11]

$$\left[-\frac{\hbar^2}{2}\frac{\partial}{\partial z}\frac{1}{m(z,E)}\frac{\partial}{\partial z}+V[n](z)\right]\psi_i(z)=E_i\psi_i(z) \quad (1)$$

The conduction band profile, $V\,[n](z)$, takes into account the electrostatic potential arising from the interface charges, the electrostatic interactions between electrons (Hartree-term), and exchange-correlation in the local-density approximation.[5,12,13] For the intersubband absorption energies, we include depolarization shift and excitonic effects.[5,11] For physical parameters of the nitrides, we use those recently recommended by Vurgaftman *et al.*[14] Temperature effects enter the calculations through their influence on AlN and GaN band gaps, the thermal expansion influencing the piezoelectric fields, and the two-dimensional Fermi distribution of the electrons.

The Varshni relation accounts for the change in band gap $E_{gap}(T) = E_0 - \alpha T^2/(T+\beta)$ with temperature T. The parameters of the two nitrides differ significantly: for GaN $\alpha_{GaN} = 0.914$ meVK^{-1}, $\beta_{GaN} = 825$ K; while for AlN $\alpha_{AlN} = 2{:}63$ meVK^{-1}, $\beta_{AlN} = 2082$ K. We keep the relative conduction/valence band offset fixed at all temperatures in the calculation. We further assume that the MQW structure is strained to the lattice parameter of the GaN substrate. The effective conduction band offset is therefore set to $\Delta E_c \approx 2$ eV at room temperature.[5,15]

The polarization field within a layer is given by the sum of the spontaneous and piezoelectric polarization:

$$P_z(T) = P_z^{\mathrm{SP}} + 2\frac{a(T)-a_0(T)}{a_0(T)}\left(e_{31} - e_{33}\frac{c_{31}}{c_{33}}\right). \quad (2)$$

Here c_{13} and c_{33} are elastic coefficients, e_{31} e_{33} are piezoelectric coefficients, and $a(T)$ is the layer lattice constant, while $a_0(T)$ is the lattice constant of the corresponding bulk material. Since the lattice constants of the active part of the MQW is set to that of the GaN substrate, the wells are unstrained, and the piezoelectric field contributes to the polarization fields only within the barriers. For the thermal expansion, we use the relation specified in Ref. 16.

The Schrödinger equation is solved using the finite-difference method.[17] This scheme benefits from an expansion of the non-parabolicity correction. We use an open-source routine to solve the resulting eigenvalue problem.[18] The finite-difference approach secures a numerically robust solution to the Schrödinger equation, and in addition, provides a big speedup over the standard shooting method. We use potential mixing to dampen charge oscillations in the self-consistent cycle in the solution of the Schrödinger-Poisson equations.[5,15]

Table I: Characteristics of the samples A, B, and C at room temperature: barrier and well thickness, experimental and calculated absorption peak positions.

Sample	Barrier/well thickness (nm)	measured peak position (meV)	calculated peak position(meV)
A	4.2/3.3	704	690
B	2.8/3.6	626	612
C	3.1/2.4	739	712

Table I specifies the thickness of the AlN barriers and GaN wells for the three samples. It also gives the experimental and calculated (for a single period) room-temperature peak position of the

absorption curve. The barriers are delta-doped with a sheet-donor concentration of $n_d = 7 \cdot 10^{12}$ cm^{-2}, while the GaN cladding layers are doped to $n_d = 2 \cdot 10^{18}$ cm^{-3}.

When examining or designing heterostructures in materials with huge internal fields, it is essential to consider the full structure, as the long-range electric fields could distort, or even deplete the active part of the structure.11 To investigate these matters for the MQW structure of this study, we solve the Schrödinger-Poisson equation for the full structure in equilibrium (with a common Fermi level) and make sure to use a unit cell size large enough to get bulk-like behavior far from the central cell.

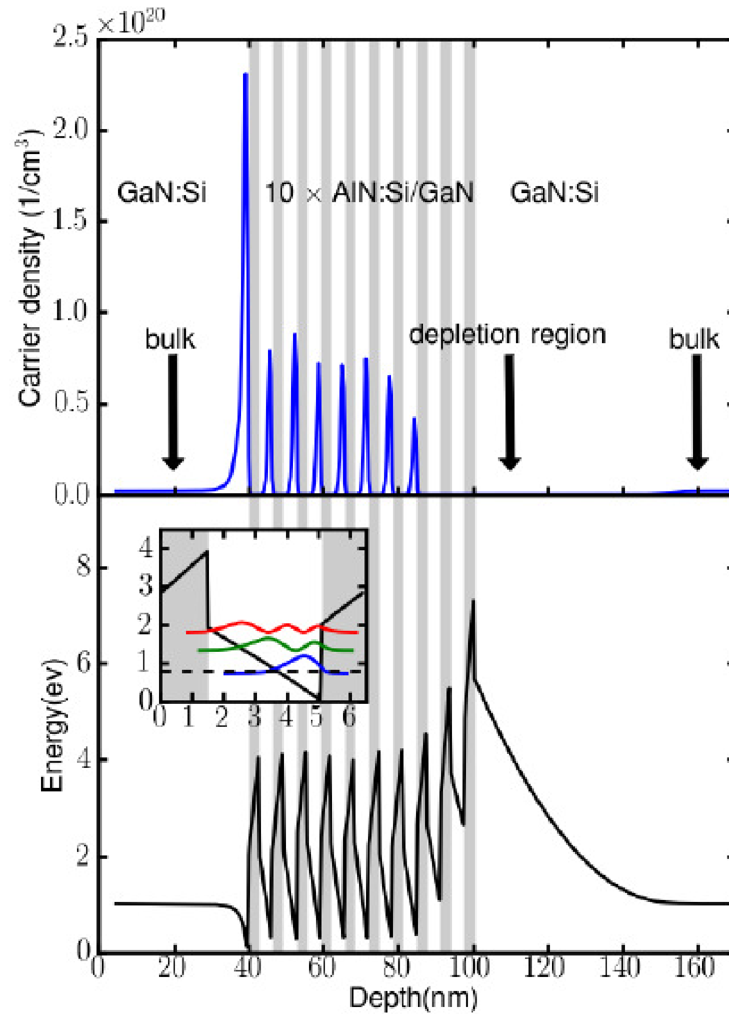

Figure 1: The carrier density (upper panel) and conduction band profile (lower profile) of a ten period AlN/GaN multiple quantum well structure (sample B) with doped AlN barriers (gray background) and doped GaN cladding layers generated by the Schrödinger-Poisson solver. The two rightmost wells are completely depleted and do not contribute to the absorption. The inset illustrates the three lowest bound state of a period of the MQW structure. The dashed line gives the room-temperature Fermi level.

Figure 1 shows the calculated carrier density and conduction band profile for the multiple quantum well (MQW) structure of sample B. The light gray background indicates the position of the doped AlN barriers. At the first GaN/AlN interface (from the left), a two-dimensional electron gas is formed. Following the right AlN/GaN interface, there is a long electrostatic tail, depleted of conduction electrons. Moreover, the two rightmost wells are also completely depleted, while the third

from the right is partially depleted. Between these two regions, the potential profile of the MQW structure approximately repeats itself and this region should therefore dominate the absorption spectra. Thus, we can focus our calculations on a single period of the structure. The inset of Fig. 1 displays the potential profile and the three energetically lowest states for a single period of the MQW structure. The calculated and experimental intersubband absorption energies are given in Table I.

Figure 2 shows the shift of the absorption energy for the three samples at different temperatures. To emphasize the temperature trend, the data-series are shifted to zero at room temperature. The results for sample A to C are ordered from top to bottom in the panels of the figure. The filled dots

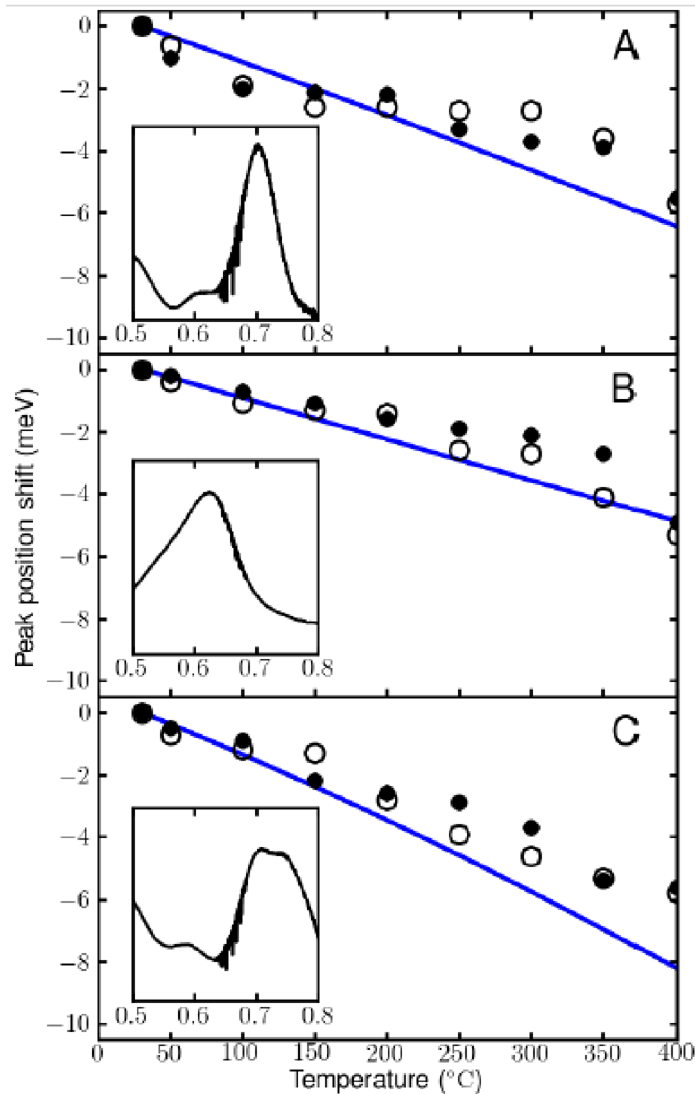

Figure 2: Temperature-dependent shift in absorption peak-position for samples A to C. The peak positions are given relative to the room temperature result. The experimental data obtained by increasing the sample temperature are given by the filled dots, while the open circles give the data when decreasing the sample temperature. The full line gives the calculated shift in peak position. The inset shows the absorption spectrum at room temperature, where the *x*-axis gives the photon energy in eV.

(circles) indicate the measured values obtained with increasing (decreasing) temperature. The good coincidence between them indicates the low experimental uncertainties. The experimental peak positions shift by ~ 6 meV as temperature is increased from room temperature to 400^{0}C. The insets

show the measured room-temperature absorption spectra for the samples. The full line gives the calculated shift.

The calculated and experimental results are in good agreement. There is a somewhat poorer correspondence for sample C. This discrepancy could be related to presence of a double peak. Based on our calculations, we attribute multiple peaks to mono-layer fluctuations. A well that is one mono-layer thinner (wider) shifts the calculated peak position by 40 (30) meV. This shift explains the shape of the spectrum in the inset of Fig. 2.

The temperature-dependent shift in transition energy is most affected by the shift in band offset, but the strain-induced piezoelectric effect is also essential. By only including the temperature dependent band offset, we get 60, 67, and 80 % respectively of the full energetic shift for sample A to C. The higher percentage for sample C stems from a larger penetration into the left AlN barrier, and therefore an increased sensitivity to the band offset. The remaining part of the shift comes from the piezoelectric effect. The energetic shift caused by the redistribution of the electrons is negligible, because of the large intersubband transition energies.

The documented temperature insensitivity for intersubband transition energies in AlN/GaN MQWs is very promising for intersubband devices made with these materials.

The authors are grateful to F. Capasso, Q. J. Wang and C. Plügl for helpful discussions. X. Liu is acknowledged for assistance in growth and S. Lourdudoss for supplying substrates. Financial support was received from Vinnova through the grant distribution “Banbrytande IKT 2007”.

---

[1] C. Gmachl, H. M. Ng, S. N. G. Chu, and A. Y. Cho, App. Phys. Lett. **77**, 3722 (2000).
[2] K. Kishino, A. Kikuchi, H. Kanazawa, and T. Tachibana, App. Phys. Lett. **81**, 1234 (2002).
[3] A. Helman et al., App. Phys. Lett. **83**, 5196 (2003).
[4] T. Aggerstam et al., Quantum Sensing and Nanophotonic Devices IV, Proc SPIE **6479**, 64791E (2007).
[5] X. Y. Liu, P. Holmstr¨om, P. J¨anes, L. Thyl´en, and T. G. Andersson, Phys. Stat. Sol. (B) **244**, 2892 (2007).
[6] P. K. Kandaswamy et al., J. App. Phys. **104**, 093501 (2008).
[7] D. C. Larrabee et al., App. Phys. Lett. **83**, 3936 (2003).
[8] T. Y. Lin, Y. M. Sheu, Y. F. Chen, J. Y. Lin, and H. X. Jiang, Sol. State Com. **131**, 389 (2004).
[9] O. Brandt, R. Muralidharan, A. Thamm, P. Waltereit, and K. H. Ploog, App. Surf. Sci. **175 - 176**, 419 (2001).
[10] T. Ive, O. Brandt, and K. H. Ploog, J. Crys. Growth **278**, 355 (2005).
[11] S. Gunna, F. Bertazzi, R. Paiella, and E. Bellotti, Nitride Semiconductor Devices: Principles and Simulation, chapter Intersubband Absorption in AlGaN/GaN Quantum Wells, 2007.
[12] W. L. Bloss, J. App. Phys. **66**, 3639 (1989).
[13] L. Hedin and B. I. Lundqvist, J. Phys. C: Sol. State Phys. **4**, 2064 (1971).
[14] I. Vurgaftman and J. R. Meyer, Nitride Semiconductor Devices: Principles and Simulation, chapter Electron Bandstructure Parameters, 2007.
[15] F. Bernardini and V. Fiorentini, Phys. Rev. B **57**, R9427 (1998).
[16] H. Iwanaga, A. Kunishige, and S. Takeuchi, J. Mat. Sci. **35**, 2451 (2000), 10.1023/A:1004709500331.
[17] F. Alharbi, Opt. Quant. Elec. **40**, 551 (2008).
[18] SciPy linalg routine eigbanded. SciPy: Open source scientific tools for Python:, 2001–. http://www.scipy.org/